Università
Ca'Foscari
Venezia

Corso di Dottorato di ricerca

in Science and Technology of Bio and Nanomaterials

in convenzione con il Centro di Riferimento Oncologico di Aviano

ciclo XXXIV

Tesi di Ricerca

Development of Multifunctional Nanomaterials for Biomedical Applications

SSD: BIO/11

Coordinatore del Dottorato
ch. prof. Alberto Vomiero

Supervisore
ch. prof. Flavio Rizzolio

Supervisore
ch. prof. Vincenzo Canzonieri

Dottorando
Muhammad Adeel
Matricola 956465

Acknowledgements

First, I would like to express my sincere gratitude to my supervisor **Professor Flavio Rizzolio** for his continuous guidance, support, and encouragement throughout my Ph.D. study and research. I am thankful for giving me the freedom to pursue independent research work, which allowed me to learn both biosensors and nanomedicine research fields. I would like to thank **Professor Salvatore Daniele** for his unlimited help in my research and guidance for better future. I am impressed his way of teaching and I am one of the lucky students to get first handed training from him. Thanks for providing me the opportunity to work in his lab under his continuous supervision. I am thanks to **Dr Mahbub** to help me, not only in my Ph.D. but also in my carrier overall. Though he was on distance, but I always find him available for me to get help and guidance on daily bases. His friendly way and sincerity will always be precious in my entire life. Also, I am thankful to **Professor Vincenzo Canzonieri** providing me CRO facilities and help in completing my degree. From the core of my heart, I would like to thank my parents who raised me with their love and supported me in all my pursuits. My brothers and sisters, was a source of my inspiration and their encouragement allowed me to become more dedicated to research and light up lonely moments during my Ph.D. I would like to give them a special ‘’thanks’’.

I would like to express my sincere thanks to all my friends and colleagues, who supported me a lot in various aspects. Special thanks to all my Italian friends and lab members (including research fellows, postdocs, Ph.Ds., and technical staff) for their technical support and service in my research. Special thanks to my friend and lab fellow Kanwal Asif and a friend Andera, for being with me in my every up and down moments and dedicated me to focus more on my research.

Special thanks to the Ca’ Foscari University, PhD’s coordinator (**Prof. Alberto Vomiero)**, CRO Aviano and technical staff, especially **Francesca Guidi** who always help me a lot in this journey. Above all, I owe it all to almighty for granting me the wisdom, health, and strength to undertake this research task and enabling me to complete it successfully. This thesis is dedicated to my parents, my brothers and sister, the recently departed souls, Mamu jan and Bubo (who wanted to see me a good doctor and a fruitful scientist always, RIP) and non-other than my grandmother (Dadi jan, RIP).

Mohammad Adeel
Ca' Foscari University
September 2021

Table of Content

Abstract:

The research conducted in this thesis was focused on two main topics. The first was to develop electrochemical sensors and biosensors, based on nanostructured materials, for the detection of molecules of biological interest. The second was devoted at establishing novel strategies and synthetize compounds for the treatment and cure of cancer.

As for the first topic, electrochemical sensors, based on 2D materials, including metal organic frameworks, were developed for the enzyme-less detection of glucose. The synthesised nanomaterials, defined nanozymes, are capable of efficiently catalyze directly (i.e., act as artificial enzymes) the oxidation of glucose. The sensors were employed to detect glucose in phosphate buffer and diluted plasma samples at both physiological pH and alkaline conditions. Flexible carbon foil was employed as substrates to construct biosensors for the earlier stage detection of COVID-19. This goal was achieved by immobilizing a suitable antibody on the carbon cloth surfaces for the selective detection of the SARS-CoV-2 spike protein. The developed sensor, being wearable, can be integrated in facemasks, for self-monitoring of the onset of Covid-19 disease.

The second topic was concerned with the development of different systems to treat high grade serious ovarian cancer (HGSOC). A drug delivery system, encompassing a novel compatible hydroxylated-boron nitride-nanosheets, was synthesised and employed as carrier of doxorubicin. To avoid some drawbacks related to this approach, carrier-free delivery systems, made of a hydrophobic drug (MAGL) was also prepared. The super hydrophobic molecules of the drugs were solubilized, while simultaneously reducing their sizes, with different surfactants and then covered with albumin nanocrystals to obtain stable and safe *in vivo* carrier systems. A self-therapeutic nanomaterial (e.g., cobalt hydroxide nanosheets) that can act like a “magic nano bullet” free from extra therapeutic compounds or external stimuli dependency was also investigated and proposed for practical or clinical purposes.

Key Words: *Multi-functional Nanomaterials, Electrochemical Biosensors, Nanomedicine, Enzyme-less Glucose Detection, COVID-19, Self-Therapeutic, Drug Delivery Systems.*

Chapter 01: Introduction

Health is one of the major issues around the globe[1]. Every year several billions of dollars are spent to launch and explore new projects to have better lifestyle or save lives. According to the United Nations report of "world-historical death rate data" the death rate of 2021 is around 7.645 while the growth rate is 0.43% around the globe[2]. According to WHO statistics of 2017, major causes of deaths are due to cardiovascular and cancer diseases[3] as is displayed in **Figure1.1**. Besides, there are several diseases that contribute to a general medical disorder, and among others diabetes (it is listed in the top position of mortality rate, **see Figure 1.1**) plays a role[4].

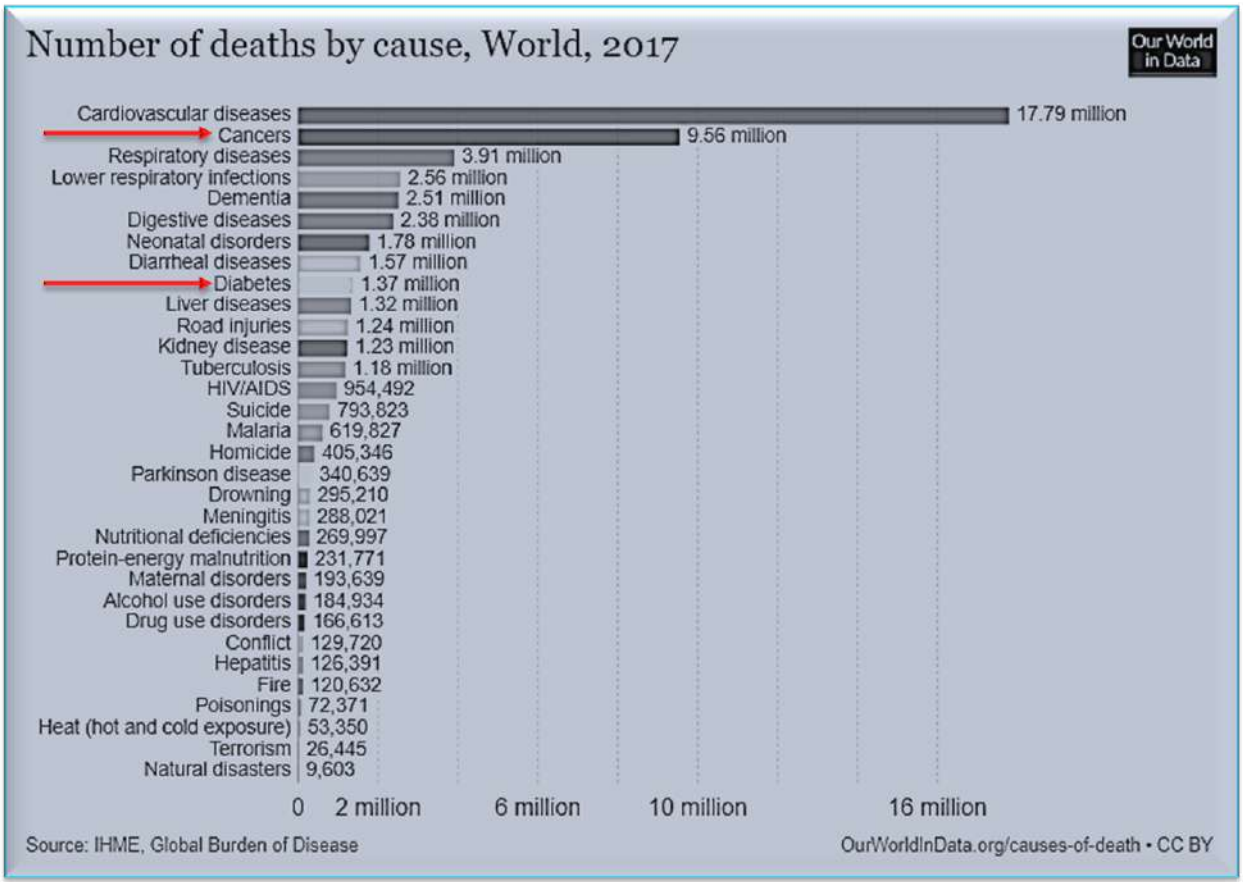

Figure: 1.1 World deaths statics data of 2017 caused by different diseases by IHME, global burden of disease (copy right, google).

Cancer is the deadly disease that kills a huge number of people every year around the globe[5]. Although several therapeutic systems were employed to root out this life hunting disease, as yet

no system is available that can eradicate it completely[5,6]. Among all other different types of cancers, ovarian cancer is considered one of the most aggressive at late stages (overall survival rate of <30% as shown in **Figure 1.2**)[7]. High grade serous ovarian cancer (HGSOC) is almost 70% of all ovarian cancers and is characterized by a high mortality[8]. Therefore, there is the necessity to explore new therapeutic systems for (HGSOC) cancer therapy.

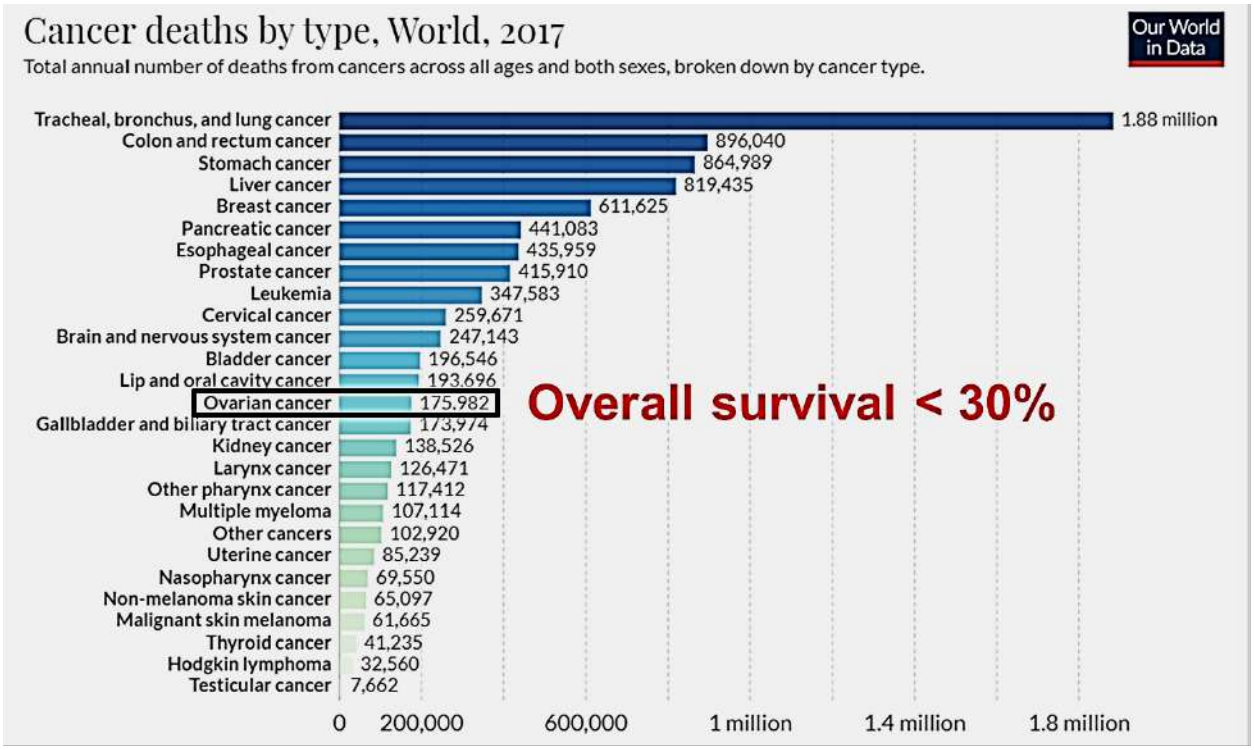

Figure 1.2: Cancer death by type, 2017 WHO (copy right, google).

On the other hand, diabetes caused the death of 1.37 million people worldwide in 2017. By world health organization (WHO), diabetes is predicted to be the world's 7th leading cause of death by 2030[2]. It is caused by the insulin deficiency, due to the demolition of the β-cells of the pancreas (type I or juvenile-onset diabetes) or because target cells oppose to insulin/insulin deficiency (type-2 or adult-onset diabetes)[9]. Around the globe, about 5-10% and 90-95% of diabetes are accounted for type-1 and type-2, respectively[10]. Multifactorial causes of diabetes include both genetic and

environmental influences, for example, by virus and life-style[10]. The early diagnostic of diabetes can save many lives every year. This can be done by using simple, easy, portable devices that can be handled personally without any need of hospitalization or technician help[9]. Alongside the aforementioned major diseases, which lead to death, unforeseen causes, such as a pandemic, can increase mortality or make life-style difficult for people around the world. Severe acute syndrome coronavirus (SARS-CoV-2 or 2019-nCoV) has been the most lethal disease from 2020 that challenged the health system of all around the globe[11,12]. It started in December 2019 with a serious and unknown cause of pneumonia[12]. The World Health Organization (WHO) classified COVid-19 outbreak as pandemic on March 12, 2020, due to the rapid human to human transmission, and in Europe, the mortality due to covid-19 was number one (**Figure 1.3**)[13].

Various types of vaccines are nowadays available to combat the virus. However, worldwide vaccination program will take a long time, also because of the urgent need of million doses production and supplying by pharmaceutical manufacturing companies, while its success will depend on the public's acceptance. Recent studies published in October 2020 have indicated that whereas most would accept a future vaccine against Covid-19, a not negligible percentage would not or fear vaccination[14]. Therefore, one of the best possible way to control and manage Covid-19 lethal disease is still social distancing and the use of physical protections such as masks. One of the main cause to spread of this disease is due to healthy carriers, who are asymptomatic[15]. It is evident that early detection of the infection is a key issue for a successful control and manage the COVid-19 disease.

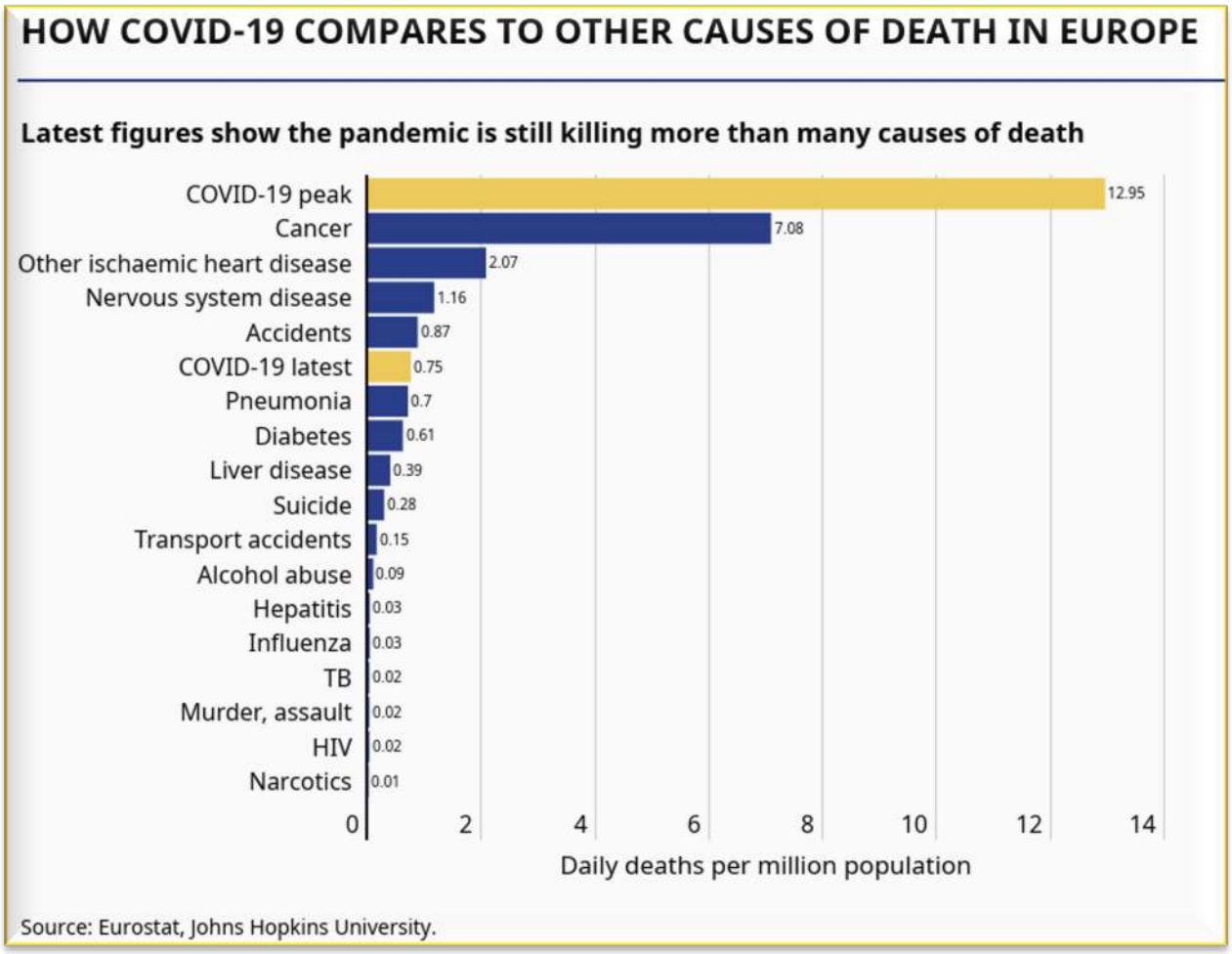

Figure 1.3: A comparison between other causes and Covid-19 deaths recently in Europe by Eurostat, Johns Hopkins University estimation (Copy rights, google).

To deal with the above aspects and to provide practical solutions, several strategies can be adopted, and those based on advanced chemical sensors, from one side, and new approaches to treat cancer therapy, from the other side, either exploiting nanotechnology and nanomaterials, represent nowadays widespread pursued roads. Brief and general information relating to these topics is provided in the following sections.

1.1 Electrochemical sensors and biosensors

A chemical sensor can be defined according to the IUPAC recommendations*: "A chemical sensor is a device that transforms chemical information, ranging from the concentration of a specific sample component to total composition analysis, into an analytically useful signal. The chemical information, mentioned above, may originate from a chemical reaction of the analyte or from a physical property of the system investigated* "[16]. The sensor includes two basic functional units: a receptor and a transducer part. The latter has the function to transfer the signal from the output domain of the recognition system into an output signal (usually electric), which in turn is converted into useful data. The receptor part of the chemical sensors can be based upon various principles; in case it is based on a biological process, the chemical sensor is defined biosensor. A biosensor can be therefore defined as "a device that uses specific biochemical reactions mediated by isolated enzymes, immunosystems, tissues, organelles or whole cells to detect chemical (or biochemical) compounds"[16].

Several different chemical sensors and biosensors have been developed based on their different transduction principles, such as electrochemical, optical (i.e., absorbance, fluorescence, Raman, etc.), mechanical, thermal, etc.[9] Among them electrochemical sensors are advantageous because of their high sensitivity, selectivity, low cost and ease in fabrication[9,17]. In recent electrochemical sensors and biosensors, electrodes modified with a variety of nanomaterials (nanoparticles, graphene, carbon nanotubes, 2D inorganic composites, etc.)[9,18] have been employed. These materials possess specific properties able to enhance the signal (through, for instance, catalytic reactions) or selectivity (through, tailoring the receptor) towards the target analyte and convert it into measurable current, voltage or resistance. An overall schematic illustration of the electrochemical sensors and biosensors is shown in **Figure 1.1.1**.

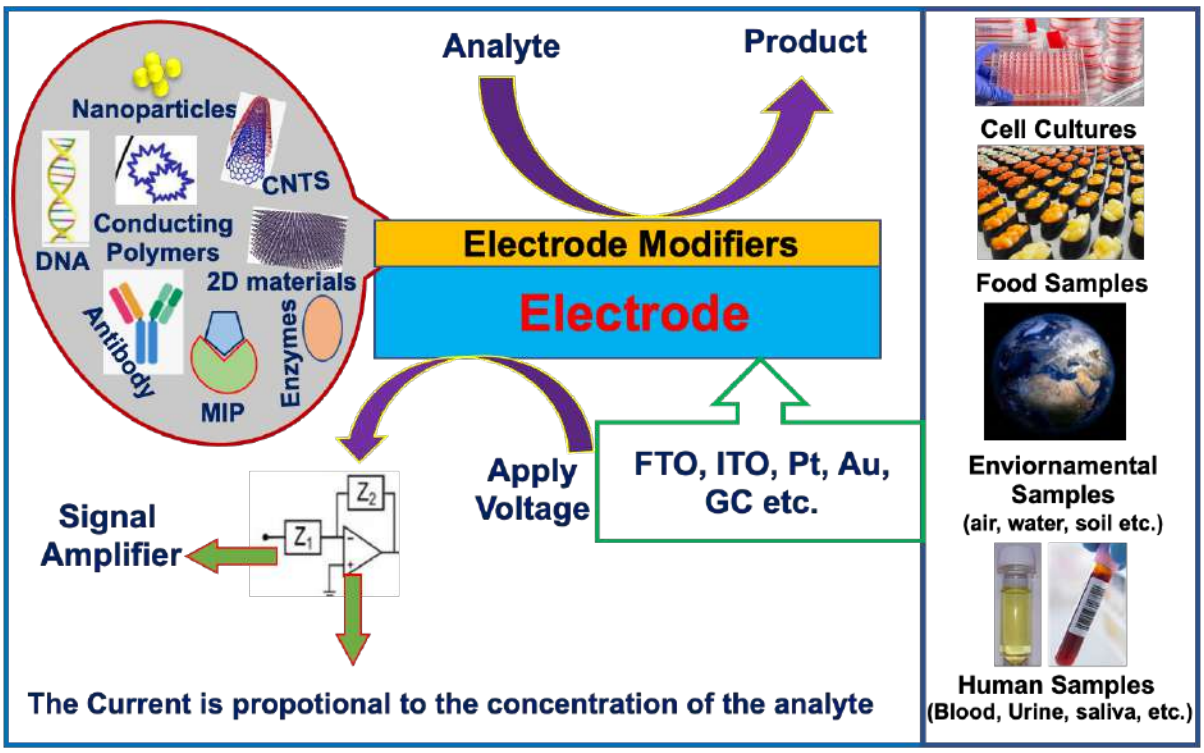

Figure 1.1.1: Schematic illustration of different components of electrochemical sensors and biosensors.

1.2 Electrochemical Techniques

Amperometry, voltammetry, potentiometry, and impedance are the main techniques used to determine the concentration of the target analyte[19,20]. The waveforms and corresponding display signals of few of the techniques are shown in **Figure 1.2.1**

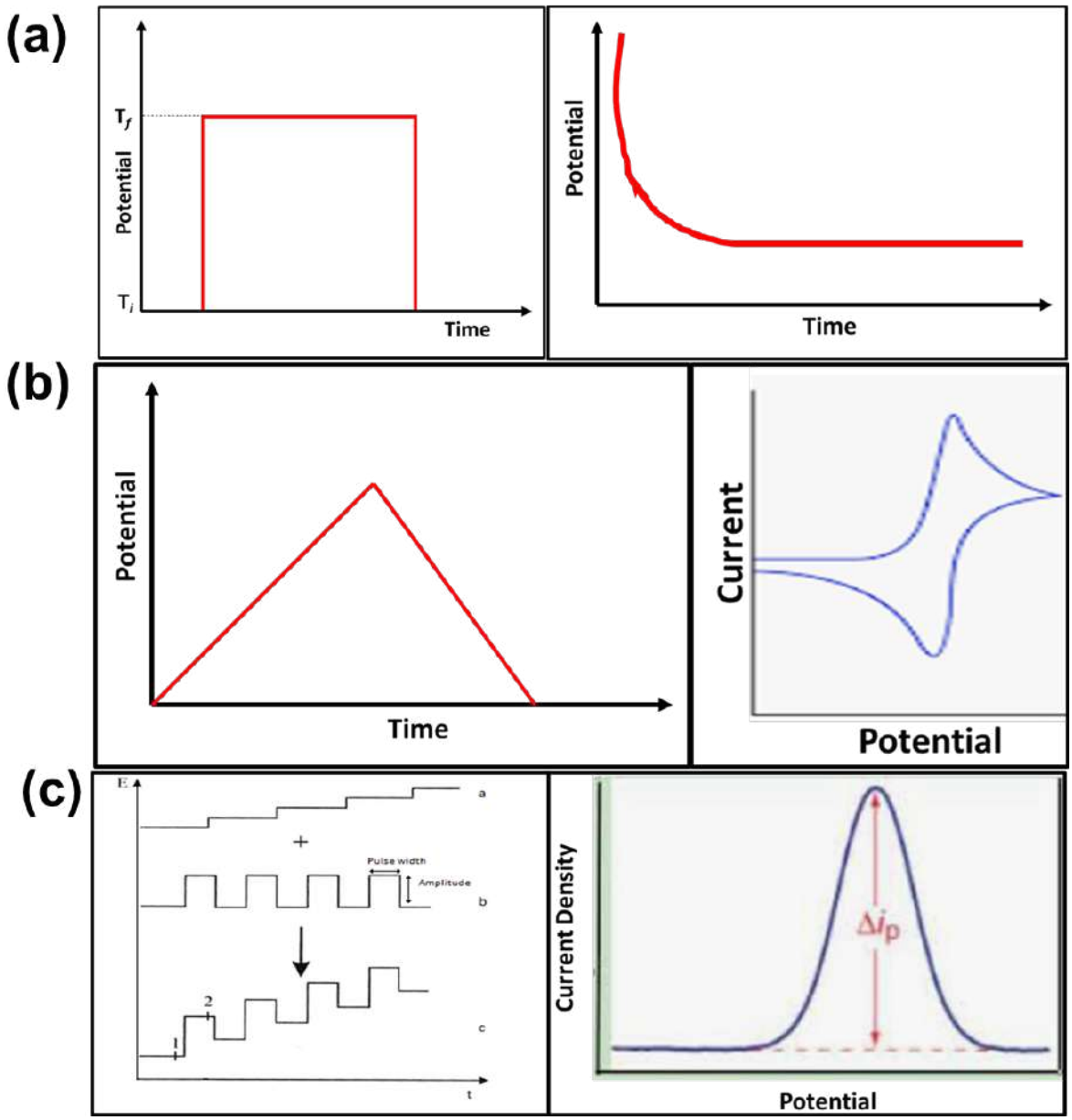

Figure 1.2.1 (a), (b) and (c) represents the waveforms and relevant responses of chronamperometry, cyclic voltammetry and differential pulse voltammetry, respectively.

Amperometry (**Figure 1.2.1a**) and voltammetry (**Figure 1.2.1 b,c**) are the dominant techniques employed, and the output signals are current as a function of time or of the applied potential and the current responses are proportional to analyte concentrations. Cyclic voltammetry is used to "fingerprint" an electrode process and mostly to obtain qualitative information on the

electrochemical mechanisms involving the analyte. For more selective and quantitative applications, pulsed techniques, such as differential pulse voltammetry (DPV) is in general employed[9]. On the other hand, potentiometry produces electrical potential responses, under electrochemical equilibrium conditions, and it is typically employed for the detection of ionic species (i.e., in conjunction with ion selective electrodes). In some cases, impedance techniques are also employed. Impedance measures the interfacial properties of an electrode-solution interface by imposing a small amplitude (5-10 mV), sinusoidal alternating current (AC) potential[21].

Amperometric and voltammetric measurements are often taken by the use of millimetre sized electrodes (generally known as conventional electrodes) at which planar diffusion occurs [22,23].

Due to some limitations of these electrodes, especially for the *in vivo* applications (i.e., implanted inside human, animals, small volume samples, etc., with minimal invasiveness), micro- nano-electrodes, can be better employed [22]. These electrodes have dimensions from about 50 μm down to a few nanometres, possess various geometries, and the current responses are dictated mainly by radial diffusion[22]. A more recent technique that exploits the properties of nano- micro-electrodes and is very useful for the characterization of chemical and biochemical events, is scanning electrochemical microscopy (SECM). SECM is an electrochemical techniques that perform measurements at interfaces with high spatial resolution[24–26]. A scheme of a typical SECM apparatus is shown in **Figure 1.2.2**.

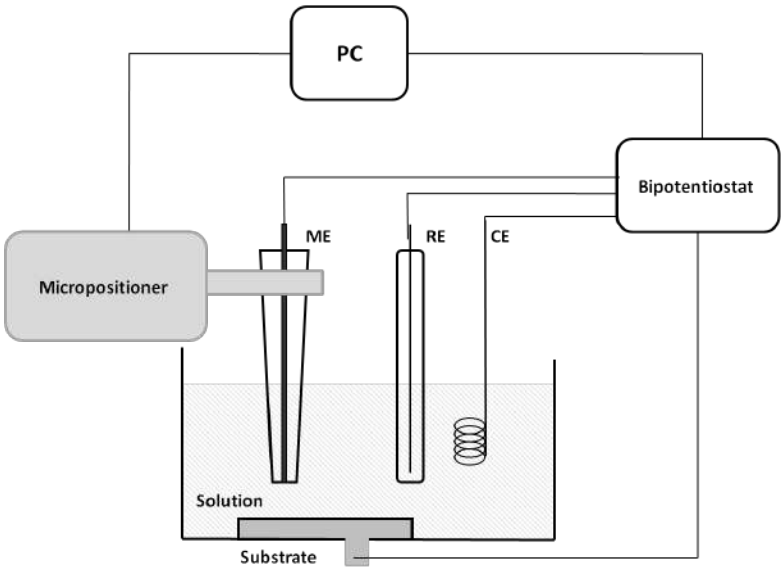

Figure 1.2.2: Scheme of a typical SECM apparatus. ME: microelectrode. RE: reference electrode. CE: counter electrode.

In typical SECM experiments, a microelectrode is scanned in the space above the surface of interest in close proximity by the use of three stages micro- or nano-positioning device. Current signals are recorded as a function of the microelectrode position in the space, thus allowing to obtain images of chemical reactivity of the substrate in non-invasive way. The technique has been used to image the performance of a variety of biosensors[25–27].

1.3 Principles and historical development of the electrochemical glucose sensors

The accurate and precise, low-cost, fast, and point-of-care monitoring of the glucose level directly in the blood is one of the top priorities for the diagnosis and prognosis of diabetic patients as well as to control glucose levels in healthy humans[9,18,28]. The progressing of glucose sensors from first to fourth generation and replacement of the biological enzyme with a non-enzymatic catalyst. In particular, direct glucose oxidation on nanomaterials is one of the major challenges for researchers recently[9] (**Figure 1.3.1**).

The electrochemical glucose sensor consists of the biological recognition element (biological enzymes, or other catalytic compounds), the electrochemical transducer (substrates FTO, ITO, Au, carbon or Pt electrodes), and the signal processing and display unit as is shown in **Figure 1.3.1a**. Generally, the main part of electrochemical sensor is molecular recognition component, which catalyzes the electro-oxidation of glucose with high selectivity[29]. By the 1950s, selective electrodes had been developed to detect oxygen in samples [30a]. Building on these, in the 1960s, Clark developed the first enzyme-modified electrodes by entrapping glucose oxidase in a dialysis membrane over an oxygen probe [30a,b]. The other commonly used enzyme that catalyzes the oxidation of glucose is the glucose-1-dehydrogenase (GDH) along with the oxidized form of pyrroquinolinequinone (PPQ) (i.e., the PQQ-GDH system). GOx is more specific for glucose oxidation (about $5x10^3$ per second in half of the electrochemical relevant reaction)[9], while PQQ-GDH is less selective for glucose sensing, due to the fact that it can catalyze the oxidation also of other sugars[9].

The fundamental principle of operation of the enzymatic glucose sensor sensor is schematized in **Figure 1.3.1 b** and depend on the following reaction mechanism:

$$\text{Glucose} + O_2 \xrightarrow{GO_x} \text{Gluconic acid} + H_2O_2$$

$$H_2O_2 \xrightarrow{Pt} 2H^+ + O_2 + 2e^-$$

It involves the GOx catalyzed oxidation of glucose by molecular O_2 with the production of gluconic acid and H_2O_2. The latter is oxidized at the Pt electrode, and the current thus generated is proportional to the amount of glucose in the sample. This is considered as 1st generation glucose sensor and has been widely used for the self-monitoring of blood glucose level at physiological pH. Although Clark's glucose sensor is highly selective towards glucose oxidation, its detection

process is significantly dependent on the concentration of O_2 in the sample. When applied in biological fluids, the restricted solubility of O2 in these media (known as the "oxygen deficit") greatly influenced the responses of the 1st generation glucose sensor[9,31]. To overcome this problem, the 2nd generation glucose sensor **(Figure 1.3.1b)** was introduced by changing O_2 with a non-physiological redox mediator to transfer electrons from the glucose to the surface of the sensing electrode[31]. After that, a 3rd generation glucose sensor **(Figure 1.3.1b)** was developed based on the direct electron transportation between the GOx and the sensing surface, therefore overcoming the necessity of both mediator and O_2. Although both these 2nd and 3rd generation-GOx based glucose sensors could effectively overcome the O_2 problem, stability issues of GOx still applied[9,31]. Furthermore, other drawbacks occurred due to the complex immobilization processes of GOx, chemical degradation of the material of the sensor system during its fabrication process, storage, and use[9].

In recent years, the introduction of non-biological catalysts has drawn considerable attention for the detection of glucose, as, in principle, they effectively solved the constraints of 1st to 3rd-generation glucose sensors. The new class of glucose sensors is designated as enzyme-free or fourth-generation glucose sensors. For the latter types of glucose sensing devices, the electrode modifiers have a paramount importance. In this regard, fueled by the significant progress in nanotechnology various nanostructured materials, composed of metals, metal oxides and their hybrids with organic compounds have been exploited for non ezymatic sensing. These systems were named ‘‘nanozymes’, that is, nanomaterials with enzyme-like activities[9,32,33].

To date, several different types of nanomaterials have been developed for the direct electrochemical oxidation of glucose. They include metals (Au, Ag, Ni, Cu, Co, etc.)[9,34] metal-oxides (NiO, CuO, Co2O3, etc.)[34–36] metal sulfides, metal-organic framework (MOF), and metal

azolate framework (MAF)[37,38]. Although these nanomaterials and composites can successfully oxidize the glucose, most of them suffer from several problems that prevent their practical applications towards the monitoring of diabetic patients and thus have not reached the commercial glucose sensor market. Main drawbacks of these systems are: lack of selective recognition elements in their structures and their working conditions, as they commonly rely on alkaline solutions, i.e., far from physiological pH conditions. Nevertheless, with future advances in the synthesis of nanomaterials, along with deeper understanding of the mechanism of their catalytic pathways, nanomaterials could approach the 3D architecture mimicry of the enzymes towards practical applications, involving also the glucose sensor industry.

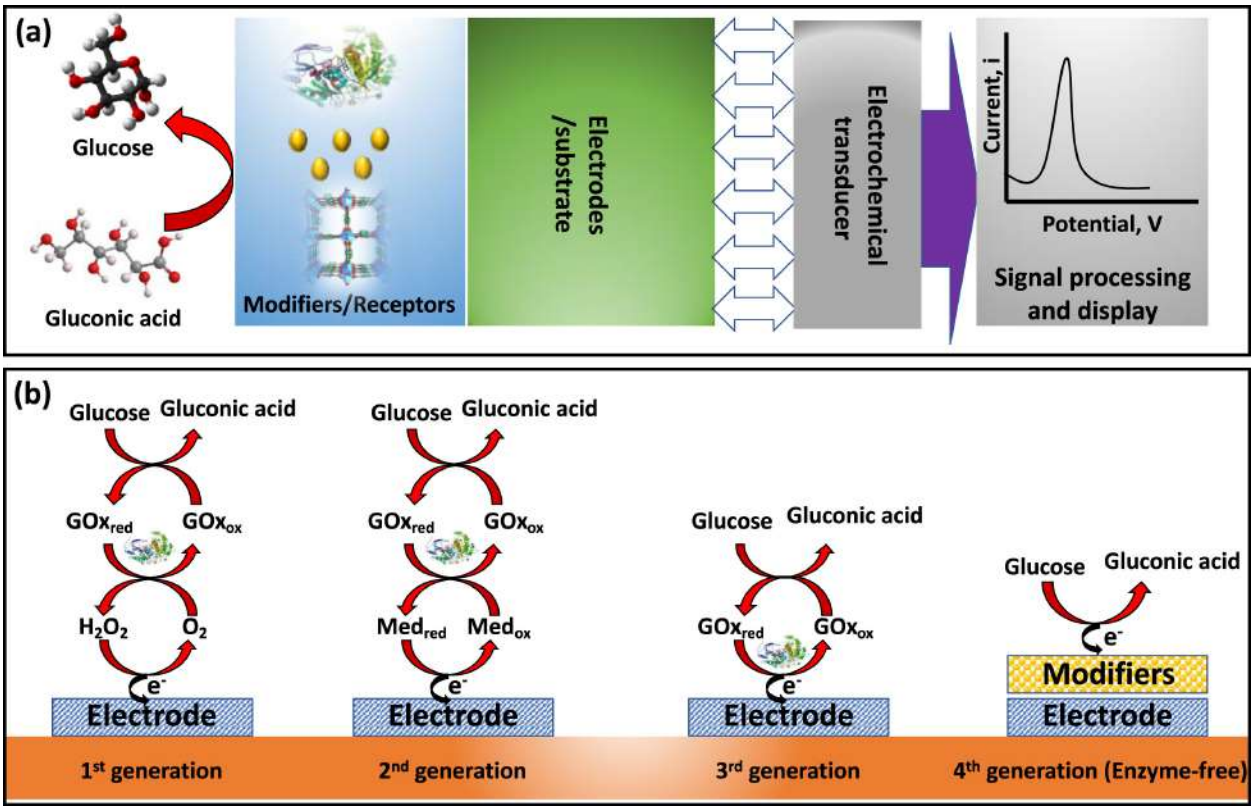

Fig. 1.3.1 (a) General schematic illustration and (b) working principle of different generations of an electrochemical glucose sensor (copy right Adeel et al.2020).

1.4 Nanomaterials and Covid-19 sensing devices

Currently, the available detection systems for Covid-19 are based on real-time reverse transcription− polymerase chain reaction (RT-PCR). In addition to PCR for SARS-CoV-2 RNA detection, ELISA for antibody analysis have also been developed[39,40]. Despite of the high sensitivity of these methods, they are not the most suitable approaches for large scale screening because of their high cost and long analysis time. A further drawback of the current detecting systems is that they need a hospital, specialized technical staffs to take samples and processing[40]. In addition to the above considerations, because SARS-CoV-2 is highly contagious, healthcare workers may be themselves infected. Therefore, there is an utmost and urgency to have smart self-detecting systems without the need for hospital and technical staff. To overcome these drawbacks, electrochemical sensors have become an appealing choice due to their high sensitivity, low-cost, ease of use and possibility of miniaturization[41,42]. By now, some electrochemical biosensing systems have also been proposed for the detection of COVID-19[42]. Magnetic nanobeads, graphene, working electrodes, or 3D nanoprinting three-dimensional electrodes, coated with nanoflakes of reduced-graphene-oxide (rGO), were employed as platforms to immobilize suitable antibodies to detect the SARS-CoV-2 spike protein (SP)[43]. Functionalized graphene and Au nanoparticles based immunosensors were reported as the proof-of-concept, label-free detection of SARS-CoV-2 SP[44]. Cu_2O nanocubes modified screen-printed carbon electrode were also suggested as immunosensor platform for the impedimetric detection of SARS-CoV-2 SP[45]. More in general, carbon-based materials (e.g., SWNT, graphene, graphitic carbon nitride) and Nobel metals (Au, Ag, Pt etc.) are considerably more attractive to develop biosensors and other electrochemical based device manufacturing[46]. This is due to non-toxicity, therefore biologically

compatible, and ease of introducing functional groups. Graphene and functionalized graphene have attracted considerable interest for the modification of conventional electrode surfaces (e.g., glassy carbon electrode, Au, etc.) for the detection different biological molecules, due to their electronic properties and high surface area with excellent chemical stability[47–49].

It must be considered that all the above systems actually represent proof-of-concept on the possibility to monitor COVID-19, but they work under almost standard experimental conditions, that is, in standard solutions or in small amounts of body fluids (i.e., saliva, tears), and modifying commercially available electrode systems. Hence, they are far of being useful to construct smart and continuous self-detecting systems. Therefore, it is still utmost to detect Covid-19 at earlier stages using, for instance, sensors for the personalized detection of Covid-19.

1.5 Nanomaterials and Cancer therapy

Recently, nanomaterials, due to their many attractive physical and chemical properties, have attracted a lot of attention from scientists fascinated by the possibility of exploiting their characteristics to prepare suitable materials to be employed in cancer therapy[50]. This can revolutionize the paradigm of how cancer can be treated. Strategies already reported in the literature, include the use of nanomaterials as carriers of therapeutic compounds[50–52]. These therapeutic systems have been extended by introducing external stimuli (e.g., light, magnetic waves and heat) to improve drug release at the tumor sites. These approaches can be further subdivided into photodynamic, photothermal, magnetic, and neutron-capturing systems. Unfortunately, the use of nanomaterials as carriers of therapeutic compounds has some flaws, which preclude these therapeutic systems from clinical applications. The major challenges are a low drug loading efficiency, low solubility in an aqueous media, poor ability to cross in vivo

barriers and penetrate inside the tumor (less than 1% reach the tumor), problematic physical and chemical interactions of hydrophobic therapeutic compounds with nanomaterials, in vivo stability, a suboptimal biodistribution, low tumor targeting ability, and a suboptimal drug release profile[50,53]. To overcome all of these issues and bring nanomaterials from the bench to clinics, scientists are trying to develop optimized self-therapeutic nanomaterials that can work like a "magic nano bullet" without the loading of additional therapeutic compounds or using external stimuli dependencies, thus making these systems more practical for clinical applications. Most of the organic nanoparticles (liposomes, micelles, exosomes, lipids, PLA, PLGA)[52], inorganic nanoparticles (gold, silver, silica, iron, graphene, carbon quantum dots)[50], and composites (metal−organic frameworks (MOF), transition metals dichalcogenide (TMD)) were designed as carriers in drug-delivery systems or for use in external stimuli-based systems such as photodynamic therapy (PDT), photothermal therapy (PTT), magnetic therapy, and boron neutroncapturing therapy (BNCP)[50]. All of these external dependencies and low loading efficiency of therapeutic compounds are shortcomings, which have led to the failure of these systems at the clinical level. Additionally, these therapeutic systems need special equipment that are difficult to use and requires confining the patient in the hospital.

The application of nanotechnology to cancer therapy could extend beyond drug delivery into the creation of new therapeutics able to destroy the tumors with minimal damage to healthy tissues and organs [5]. Furthermore, they can be applied the detection and elimination of cancer cells during the initial stage of tumorigenesis [5]. These relatively small particles can also be functionalized with ligands, nucleic acids, peptides, or antibodies that bind to specific target molecules. Because of certain intrinsic properties of nanomaterials (reaction with oxygen species, heat and hazardous gas producers) and biocompatibilities, they are quite interesting to use directly for therapeutic

purposes[50]. A further issue, related to the direct use of drugs, is that they suffer from low solubility and fail in clinical trials [54].

In fact, drug design and combinatorial chemistry have been utilized to develop new and useful drugs. They usually have high molecular weight and lipophilicity that support drug to transfer across membranes. By contrast, they are characterized but the low solubility in water[55]. This negotiates the bioavailability of the drug[56]. Therefore, in order to be available commercially (in general almost 10-17 years are required after its first synthesis)[57] a poorly soluble drug needs to be formulated through different technologies to enhance their solubility.

To conquer all the related traditional chemotherapy issues, currently much focus is given to the discovery of drugs that target specific receptors or proteins typically upregulated in tumor cells. This approach takes part of a broad concept called personalized therapy in which each patient is treated with specific targeted therapeutic compounds, based on the genotype and phenotype. Many research groups are exploring many genes, receptors, and enzymes that are mainly involved in different cancer types and could be a therapeutic target for all of them[58]. Among the enzymes, monoacylglycerol lipase (MAGL) is a member of the serine hydrolase superfamily, which primarily degrades the endocannabinoid 2-arachidonoylglycerol (2-AG) to arachidonic acid and glycerol in the brain, thus interrupting it signaling on cannabinoid receptors. MAGL is also involved in the hydrolysis of monoacylglycerols in peripheral tissues[59]. For this reason, in cancer cells, MAGL was reported to activate oncogenic signaling related to the intracellular pool of free fatty acids and it proved to be involved in sustaining the growth of different cancer cells[60]. Recently, Park et al. reported a novel nanocrystallization method for the solubilization of poorly soluble drugs. They used Pluronic F-127 and cetyltrimethylammonium bromide (CTAB) as surfactants to acquire a controlled nanocrystals formation in water and wrapped them with human

serum albumin[61]. The bare nanocrystals without albumin can lead to the adsorption of non-specific proteins resulting in the uptake by mononuclear phagocyte system (MPS). On the other hand, albumin is a natural carrier of native ligands and other hydrophobic molecules, it is very stable, digestible and decomposable by cells, provides amino acids for cell metabolism and helps to internalize the nanocrystals in tumoral sites through interacting with specific receptors[62].

Most of the above-mentioned issues related to therapeutic application using nanomaterials and nanotechnology including drug delivery systems, carrier free delivery system and self-therapeutic nanomaterials-based systems will be considered in the studies undertaken in the present thesis.

References

[1] C. Herrick, D. Reubi, Springer, Cham, **2021**; pp. 275–280.

[2] World Death rate 1950-2021, World Death Rate 1950-2021 | MacroTrends. *https://www.macrotrends.net/countries/WLD/world/death-rate* **2021**.

[3] H. Nagai, Y. H. Kim, Cancer prevention from the perspective of global cancer burden patterns. *J. Thorac. Dis.* **2017**, *9*, 448–451.

[4] WHO Diabetes report **2021**, Diabetes. *WHO* 2021.

[5] M. Adeel, F. Duzagac, V. Canzonieri, F. Rizzolio, *ACS Appl. Nano Mater.* **2020**, *3*, 4962.

[6] S. Palazzolo, M. Hadla, C. R. Spena, S. Bayda, V. Kumar, F. Lo Re, M. Adeel, I. Caligiuri, F. Romano, G. Corona, V. Canzonieri, G. Toffoli, F. Rizzolio, *ACS Med. Chem. Lett.* **2019**, *10*, 517.

[7] M. Hermens, A. M. van Altena, J. Bulten, H. A. A. M. van Vliet, A. G. Siebers, R. L. M. Bekkers, *Gynecol. Oncol.* **2021**, *162*, 735.

[8] M. A. Lisio, L. Fu, A. Goyeneche, Z. H. Gao, C. Telleria,. *Int. J. Mol. Sci.* **2019**, *20*.

[9] M. Adeel, M. M. Rahman, I. Caligiuri, V. Canzonieri, F. Rizzolio, S. Daniele,. *Biosens. Bioelectron.* **2020**, *165*, 112331.

[10] G. Xu, B. Liu, Y. Sun, Y. Du, L. G. Snetselaar, F. B. Hu, W. Bao, *BMJ* **2018**, *362*.

[11] A. A. Al-Qahtani, *Saudi J. Biol. Sci.* **2020**, *27*, 2531–2538.

[12] C. C. Lai, T. P. Shih, W. C. Ko, H. J. Tang, P. R. Hsueh, *Int. J. Antimicrob. Agents* **2020**, *55*, 105924.

[13] C. Wang, Z. Wang, G. Wang, J. Y. N. Lau, K. Zhang, W. Li, *Signal Transduct. Target. Ther.* **2021**, *6*, 1–14.

[14] M. Detoc, S. Bruel, P. Frappe, B. Tardy, E. Botelho-Nevers, A. Gagneux-Brunon, *Vaccine* **2020**, *38*, 7002.

[15] H. J. Zhao, X. X. Lu, Y. Bin Deng, Y. J. Tang, J. C. Lu, *Epidemiol. Infect.* **2020**, *148*.

[16] A. Hulanicki, S. Glab, F. Ingman, *Pure Appl. Chem.* **1991**, *63*, 1247.

[17] X. Huang, Y. Zhu, E. Kianfar,. *J. Mater. Res. Technol.* **2021**, *12*, 1649–1672.

[18] M. Adeel, V. Canzonieri, S. Daniele, A. Vomiero, F. Rizzolio, M. M. Rahman, *Microchim. Acta* **2021**, *188*, 1.

[19] A. Bonanni, M. Del Valle,. *Anal. Chim. Acta* **2010**, *678*, 7–17.

[20] Z. Meng, R. M. Stolz, L. Mendecki, K. A. Mirica, *Chem. Rev.* **2019**, *119*, 478–598.

[21] H. Herrera Hernández, A. M. Ruiz Reynoso, J. C. Trinidad González, C. O. González Morán, J. G. Miranda Hernández, A. Mandujano Ruiz, J. Morales Hernández, R. Orozco Cruz, In *Electrochemical Impedance Spectroscopy*; IntechOpen, 2020.

[22] S. Daniele, C. Bragato, Springer, New York, NY, **2014**;. 373–401.

[23] R. Toniolo, R. Bortolomeazzi, R. Svigelj, N. Dossi, I. G. Casella, C. Bragato, S. Daniele, *Sensors Actuators, B Chem.* **2017**, *240*, 239.

[24] L. I. Stephens, J. Mauzeroll, *Anal. Chem.* **2018**, *90*, 6796.

[25] F.-R. F. Fan, B. Liu, J. Mauzeroll, In *Handbook of Electrochemistry*; Elsevier, **2007**;. 471–540.

[26] H. S. Park, J. H. Jang,. *J. Electrochem. Sci. Technol.* **2016**, *7*, 316–326.

[27] R. A. Lazenby, R. J. White,. *Chemosensors* **2018**, *6*, 24.

[28] M. Adeel, V. Canzonieri, S. Daniele, F. Rizzolio, M. M. Rahman, *J. Ind. Eng. Chem.* **2021,** *103,* 165-174.

[29] N. Muthuchamy, A. Gopalan, K. P. Lee, *RSC Adv.* **2018**, *8*, 2138.

[30] a) L. C. Clark, C. Lyons, *Ann. N. Y. Acad. Sci.* **1962**, *102*, 29; b) L. C. Clark, G. Sachs, *Ann. N. Y. Acad. Sci.* **1968**,

[31] D. Grieshaber, R. MacKenzie, J. Vörös, E. Reimhult, *Sensors* **2008**, *8*, 1400.

[32] J. Kim, A. S. Campbell, J. Wang, *Talanta* **2018**, *177*, 163.

[33] W. V. Gonzales, A. T. Mobashsher, A. Abbosh, *Sensors* **2019**, *19*, 800.

[34] M. M. Rahman, A. J. S. Ahammad, J. H. Jin, S. J. Ahn, J. J. Lee, *Sensors* **2010**, *10*, 4855.

[35] N. S. Lopa, M. M. Rahman, F. Ahmed, S. Chandra Sutradhar, T. Ryu, W. Kim, *Electrochim. Acta* **2018**, *274*, 49.

[36] M. Nacef, M. L. Chelaghmia, A. M. Affoune, M. Pontié, *Electroanalysis* **2019**, *31*, 113.

[37] X. Zhou, X. Gu, Z. Chen, Y. Wu, W. Xu, J. Bao, *Sensors Actuators, B Chem.* **2021**, *329*, 129117.

[38] M. Adeel, V. Canzonieri, S. Daniele, A. Vomiero, F. Rizzolio, M. M. Rahman, *Microchim. Acta* **2021**, *188*.

[39] B. Singh, B. Datta, A. Ashish, G. Dutta, *Sensors Int.* **2021**, *2*, 100119.

[40] T. Ji, Z. Liu, G. Q. Wang, X. Guo, S. Akbar khan, C. Lai, H. Chen, S. Huang, S. Xia, B. Chen, H. Jia, Y. Chen, Q. Zhou, *Biosens. Bioelectron.* **2020**, *166*, 112455.

[41] S. D. Bukkitgar, N. P. Shetti, T. M. Aminabhavi, *Chem. Eng. J.* **2021**, *420*, 127575.

[42] T. Chaibun, J. Puenpa, T. Ngamdee, N. Boonapatcharoen, P. Athamanolap, A. P. O'Mullane, S. Vongpunsawad, Y. Poovorawan, S. Y. Lee, B. Lertanantawong, *Nat. Commun.* **2021**, *12*, 1.

[43] L. Fabiani, M. Saroglia, G. Galatà, R. De Santis, S. Fillo, V. Luca, G. Faggioni, N. D'Amore, E. Regalbuto, P. Salvatori, G. Terova, D. Moscone, F. Lista, F. Arduini, *Biosens. Bioelectron.* **2021**, *171*, 112686.

[44] B. Mojsoska, S. Larsen, D. A. Olsen, J. S. Madsen, I. Brandslund, F. A. Alatraktchi, *Sensors* **2021**, *21*, 1.

[45] Z. Rahmati, M. Roushani, H. Hosseini, H. Choobin, *Microchim. Acta* **2021**, *188*.

[46] R. Kour, S. Arya, S.-J. Young, V. Gupta, P. Bandhoria, A. Khosla, *J. Electrochem. Soc.* **2020**, *167*, 037555.

[47] A. Navaee, A. Salimi, H. Teymourian, *Biosens. Bioelectron.* **2012**, *31*, 205.

[48] J. H. Shin, M. J. Lee, J. H. Choi, J. ae Song, T. H. Kim, B. K. Oh, *Nano Converg.* **2020**, *7*.

[49] M. M. Rahman, N. S. Lopa, M. J. Ju, J. J. Lee, *J. Electroanal. Chem.* **2017**, *792*, 54.

[50] M. Adeel, F. Duzagac, V. Canzonieri, F. Rizzolio, *ACS Appl. Nano Mater.* **2020**, *3*, 4962.

[51] X. Mei, T. Hu, Y. Wang, X. Weng, R. Liang, M. Wei,. *Interdiscip. Rev. Nanomedicine Nanobiotechnology* **2020**, *12*, e1596.

[52] J. Jacob, J. T. Haponiuk, S. Thomas, S. Gopi,. *Mater. Today Chem.* **2018**, *9*, 43–55.

[53] J. Li, C. Fan, H. Pei, J. Shi, Q. Huang, *Adv. Mater.* **2013**, *25*, 4386.

[54] S. Kalepu, V. Nekkanti,. *Acta Pharm. Sin. B* **2015**, *5*, 442–453.

[55] S. Verma, S. Kumar, R. Gokhale, D. J. Burgess, *Int. J. Pharm.* **2011**, *406*, 145.

[56] A. Mercuri, P. S. Belton, P. G. Royall, S. A. Barker, *Mol. Pharm.* **2012**, *9*, 2658.

[57] E. J. Barbosa, R. Löbenberg, G. L. B. de Araujo, N. A. Bou-Chacra,. *Eur. J. Pharm. Biopharm.* **2019**, *141*, 58–69.

[58] R. Fleck, D. Bach, *J. Pers. Med.* **2012**, *2*, 15.

[59] J. Z. Long, D. K. Nomura, B. F. Cravatt, *Chem. Biol.* **2009**, *16*, 744.

[60] C. Granchi, I. Caligiuri, E. Bertelli, G. Poli, F. Rizzolio, M. Macchia, A. Martinelli, F. Minutolo, T. Tuccinardi, *J. Enzyme Inhib. Med. Chem.* **2017**, *32*, 1240.

[61] J. Park, B. Sun, Y. Yeo, *J. Control. Release* **2017**, *263*, 90.

[62] E. N. Hoogenboezem, C. L. Duvall,. *Adv. Drug Deliv. Rev.* **2018**, *130*, 73–89.

Chapter 02: Aims and Thesis layout

Thanks to material science and technology that enable to connect different field of research at one platform, its tremendous breakthrough in every field of science makes life easier in the current era. Nanoscience and nanotechnology expanded almost every field of research tremendously in basic (i.e., quantum mechanics, photonics, space technology) and in applied (through different devices) sciences. This is due to the possibility to arrange different atomic species into materials of 1-100 nm scale, allowing to create compounds having different physical and chemical properties according to the need of interest. In fact, nanoscience and nanotechnology brought a completely new era in electronics and computer engineering (from the first room size computer to a smart notebook). However, its role in health sciences, compared to other fields, is still in a development stage and far to the threshold. This may be due to inadequate experimental techniques available, lack in experimental specimens and unexpected results, especially in vivo. With the hope of achieving faster and similar transformations in health sciences as in other fields, researchers have recently turned their attention to the use of nanomaterials and nanotechnology in health sciences on aspects concerning imaging, sensing, diagnostic and therapeutic applications. In line with these considerations, the aim of this thesis was to explore strategies for preparing/using novel nanomaterials for diagnostic/sensing and therapeutic applications in cancer treatments. In particular, as is shown in schematic chart in **Figure 2.1,** the work done focused on the development of electrochemical sensors, using different nanomaterials characterized by different size, shape, as well as physical and chemical properties, for glucose and Covid-19 sensing, possibly, at physiological conditions. A second major topic considered was the use of nanomaterials or exploitation of nanotechnologies to developed smart therapeutic systems for cancer therapy. The schematic chart of the specific topics addressed is shown in **Figure 2.1**.

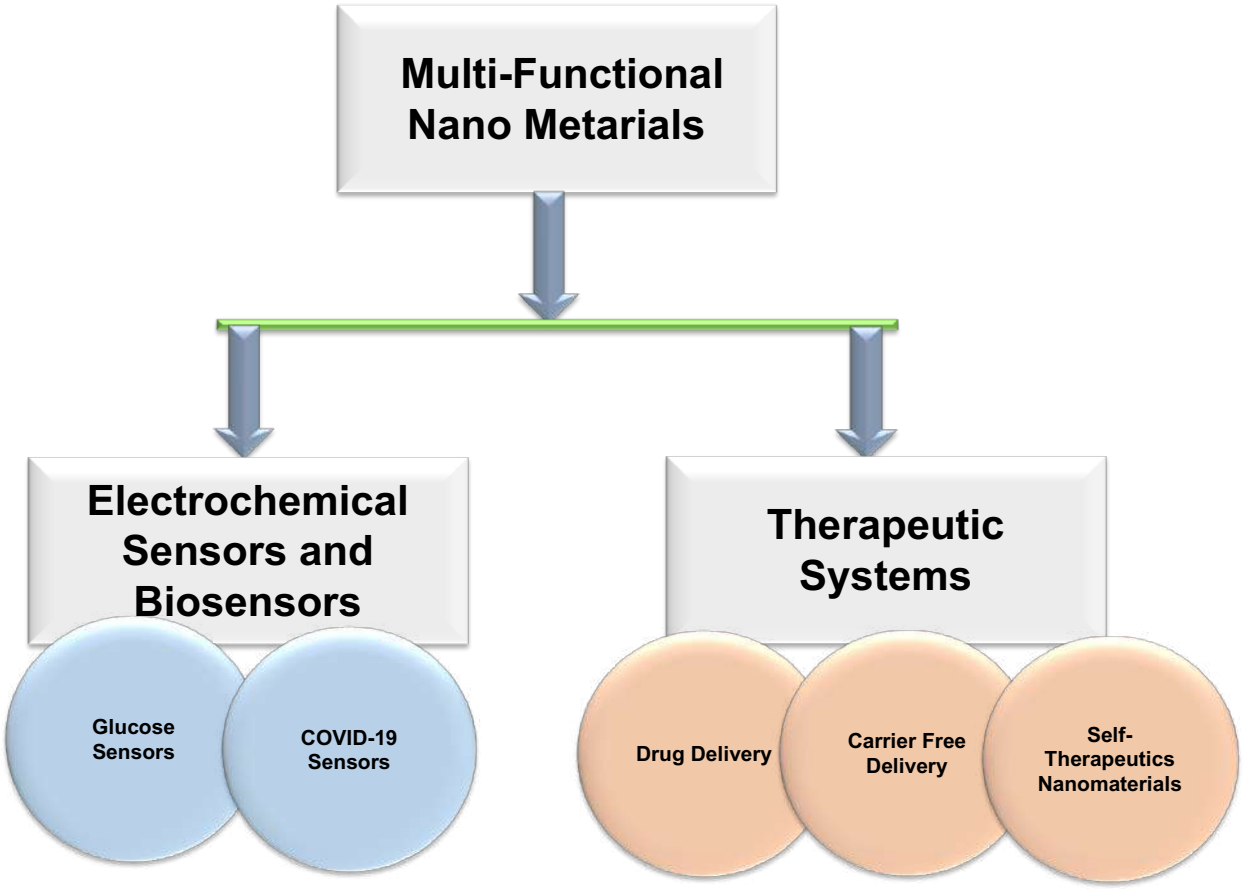

Figure 2.1: The schematic illustration of the summary of this thesis

A more detailed overview of the thesis is presented below.

Chapter: 1 This chapter includes an introduction on the role of material science and engineering in health sciences. It highlights the importance of nanotechnology and the improvements achieved in their applications in current health care devices, mainly focusing on the detection of glucose and Covid-19, as well as their use in cancer therapeutic applications.

Chapter: 2 It includes the general layout of the work carried out in the thesis.

Chapter: 3 This chapter includes all the experimental sections of the work carried out in the thesis including both sensing devices and nanomaterials based therapeutic systems.

Chapter: 4 It contains the results and relevant discussion sections. It is divided into sub-sections to deal with the glucose and Covid-19 sensing devices and the different therapeutic systems or developed strategies (drug delivery, carrier free and self-therapeutic nanomaterials).

Chapter: 5 This chapter reports the overall conclusions, shortcomings, and future perspectives of the worked carried out in the purposed thesis.

Chapter 03: Experimental Section

Section 3.1 Electrochemical Biosensors for glucose and Covid-19 detection

In this part of the thesis, electrodes modified with different materials having different shape, size, physical and chemical properties are described and employed for the construction of glucose and Covid-19 sensors. In particular, 2D materials (metal azolate frameworks (MAF), cobalt hydroxide nanosheets) and flexible carbon sheets are considered and further functionalised to prepare the covid-19 spike protein based immunosensors.

3.1.1 Reagents for the Glucose Sensors

Cobalt (II) acetate (Co(CH3CO2)2, 99.995%), Potassium hexacyanoferrate(II) trihydrate (≥ 99%), Potassium hexacyanoferrate(III) (≥ 99%), 2-Ethylimidazole (98%), triethylamine (99%), benzene, D-(+)- Glucose (99.5%), fructose, lactose, galactose, NaOH, Nafion® 117 (~ 5% in a mixture of alcohols and water), and absolute ethanol were purchased from Sigma -Aldrich (St. Louis, MO, USA). Dulbecco's PBS (pH 7.4) was bought from TermoFisher Scientific. All the chemicals and reagents were used as received. The SPE-110 was procured from Ω Metrohm DropSens. Ultrapure water was prepared using a Milli Q Biocell water purifying system and used throughout the experiment.

3.1.2 Synthesis of MAF-5-Co^{II} NS

MAF-5-CoII NS was synthesized by a modified method of a reported protocol[1]. Briefly, 0.1 g of $Co(OAc)_2$ was dissolved in water (25 mL) as a first solution. A second solution was prepared by dissolving 0.3g of EIM in a mixture of water and benzene (65:10 v/v). These solutions were rapidly mixed and stirred at room temperature for 30 minutes. Then, the resultant blue coloured suspension was centrifuged at 6000 RPM for 10 minutes. The precipitate was washed with water and ethanol

several times by the centrifuge method. Finally, the blue-colored powder was dried in a vacuum drying oven at 100 ^{o}C for 2 hours and stored for further characterizations and applications.

3.1.3 Synthesis of $Co(OH)_2$ NS

A simple solution process at room temperature (RT) has been employed to prepared high-quality $Co(OH)_2$ NS. Briefly, 0.2 g of $Co(CH_3CO_2)_2$ was dissolved in 50 mL of ultrapure water in a beaker. Another solution of ethyl imidazole (EIM (0.30 g)) and triethyl amine (TEA (0.30 g)) were dissolved in the mixture of ultrapure water and benzene (90:10, v/v). Both these solutions were mixed rapidly and stirred vigorously at RT for 1 hour. Then, the precipitate was collected by a centrifuge method at 6000 RPM, washed with water and ethanol, and dried in a vacuum drying oven at 100 oC for two hours. The as-prepared $Co(OH)_2$ NS was stored for further characterization and applications.

3.1.4 Preparation of the glucose sensor

2 mg of the as-synthesized NS was suspended in 1 mL of ethanol and Nafion (1:1) solution by sonication for 1 hour. Then, 20 µL of the suspension was drop cast onto the working area of SPE and dried at 60 oC for 1 hour. The as-prepared NS/SPE was used directly for glucose sensing.

3.1.5 Apparatus for the glucose sensor

The MAF and Co(OH)2 NS morphological analysis was analyzed by a field-emission scanning electron microscope (FE-SEM, Carl Zeiss Sigma VP) and a high-resolution transmission electron (HR-TEM, JEM-2100 (HRP)). Elemental analyses were performed by energy-dispersive X-ray

spectroscopy (EDS) (Quantax 200) equipped with the FE-SEM. The crystallographic phase information was obtained by an X-ray diffractometer (Philips Xpert, Cu Kα radiation). The elemental composition and the oxidation state were studied with an X-ray photoelectron spectroscopy system (XPS, Thermo Scientific K-Alpha, Thermo Fisher Scientific). The functional groups in the MAF and Co(OH)2 NS were analyzed by Fourier transform infrared (FTIR) spectroscopy (MIDAC, M4000). Thermogravimetric analysis (TGA) was performed in the temperature range 30–700 °C in atmospheric conditions to check the thermal stability of the compounds. The N2 adsorption isotherm was acquired at −190 °C, after evacuation at 110 °C for 12 h, using a surface area analyzer (Micromeritics, Tristar II 3020, USA).

All electrochemical measurements were performed using a CHI760B potentiostat (CH Instrument, Texas, USA). Disposable screen-printed electrodes (SPEs) (from DropSens Metrohm), in the three-electrode configuration, consisted of a carbon disk as working electrode (active area 0.96 cm^2), a carbon ring as an auxiliary electrode, and an Ag/AgCl as the reference electrode. The working electrode was covered with MAF-5-CoII NS (MAF-5-CoII NS/SPE) and Co(OH)2 NS (Co(OH)2 NS/SPE) as specified below.

3.1.6 Reagents for the Covid-19 sensor

Sulfuric acid (95-98%), Nitric acid (63%), N-Hydroxysuccinimide, Bovine Serum Albumins (≥ 98%), Potassium hexacyanoferrate (II) trihydrate (≥ 99%), Potassium hexacyanoferrate (III) (≥ 99%), and Ethylenediamine (≥ 99%) were purchased from Sigma Aldrich. Dulbecco's PBS (pH 7.4) without calcium and magnesium chloride and 1-Ethyl-3[3-dimethlaminopropyl] carbodiimide HCL were purchased from Thermo Fisher Scientific. Flexible carbon foil (99.8% of thickness 0.35 mm) was purchased from Goodfellow Cambridge. SARS-Covid Antibody (Rabbit IgG), SARS

spike protein (Source: SARS > 90 % as determined by SDS-PAGE), and MARS spike protein was purchased from Sino Biological.

3.1.7 Apparatus for the Covid-19 sensor

Most of the equipment reported in Section 3.1.5 was also used for the characterization and to perform measurements for/with the Covid-19 sensor. In addition, the following apparatuses were also employed.

Raman spectra were measured using a Raman Spectrophotometer (Horiba Scientific, Xplora Plus, France) at room temperature with an excitation wavelength of 532 nm. The wetting behaviors of the samples were examined using a contact angle measurement system (CAM, SEO-300A, Korea). To this purpose, a drop of 5 μL of distilled water was placed on the surface and the contact angle was measured after 10 seconds. Each contact angle value refers to the average obtained from 5 drops.

A CHI920C workstation (CH Instruments, Texas-USA) was employed for SECM measurements. In this case, the electrochemical cell comprised a Pt microdisk electrode 12.5 μm (nominal radius) working electrode, and a Pt wire and an Ag/AgCl (KCl, saturated) as counter and reference electrode, respectively. The Pt microelectrode was manufactured by sealing a platinum wire (Goodfellow Metals, Cambridge, UK) having 25 μm nominal diameter in a glass capillary tube following a standard procedure[2]. Afterward, it was tapered to a conical shape, polished with graded alumina powder (5, 1, and 0.3 μm), placed on a Buehler micro-cloth, and then characterized by CV at low scan rates and by SECM to evaluate the actual electrode radius of the microelectrode and the overall tip radius to the electrode radius ratio (RG)[3]. The RG of the SECM tips varied between 5 and 8. Unless otherwise stated, approach curves were plotted using normalized currents, I/I_0, against normalized distances ($L = d/a$); normalised current were also employed in the SECM

images. They were acquired by using a 2 mM $[Fe(CN)_6]^{4-}$ solution containing 0.1 M KCl as a supporting electrolyte. The EIS measurements were performed by using an impedance analyzer (IM6ex, Zahner-Elektrik GmbH & Co. KG). The measurements were acquired using the $[Fe(CN)_6]^{3-/4-}$ solution in the frequency range of 10^6 - 0.1 Hz, AC amplitude of 5 mV, and an applied potential of +0.3 V.

3.1.8 Preparation of functionalized and exfoliated graphitic carbon foils

Prior to the exfoliation and functionalization, a series of GCFs (each 2×4 cm^2) was sequentially cleaned using organic soap, deionized water, and ethanol by sonication and then dried with a stream of pure N_2 (> 99.99 %, from SIAD, Bergamo, Italy). Then, OGCFs were prepared by placing GCFs in a mixed solution of H_2SO_4 (98%), HNO_3 (63%), and ultrapure water (1:1:1 v/v/v) at 70 °C for 24 h. Afterward, the samples were washed with ultrapure water several times with gentle shaking, dried by N_2, and placed on a hot plate at 50 °C for 24 h. For the preparation of EDA-GCF, an OGCF was immersed into an EDC: NHS solution in PBS (pH 7.4) (EDC and NHS of 1 wt% corresponding to the weight of OGCF) and gently shaking for 5 h at room temperature. Subsequently, the activated OGCF was washed with ultrapure water several times and placed into an EDA solution (20 mL) at 80 °C for 24 h. Then, the sample was washed with ultrapure water by shaking to remove the unbound or physically adsorbed impurities and dried at 40 °C for 3 h. The as-prepared OGCFs and EDA-GCF electrodes were stored at room temperature for further characterizations and applications.

3.1.9 Fabrication of the immunosensor probe

Anti-SARS-CoV-2 was covalently attached through an amide bond between the free $–NH_2$ functional groups of EDA-GCF and the –COOH groups of anti-SARS-CoV-2[4]. Briefly, EDA-GCF was placed in an electrochemical cell with a confined geometric area of 0.096 cm^2, as defined by an O-ring. Then, 400 µL of an EDC (20 mM) and NHS (40 mM) solution in PBS (pH 7.4) was dropped onto the surface of EDA-GCF and kept for 5 h to activate the functional groups. Subsequently, the electrode was washed with PBS (pH 7.4), dried under a N_2 stream, and then 400 µL antibody (1 µg/mL in PBS pH 7.4) solution was dropped onto the activated EDA-GCF surface and incubated at 4 °C. Thereafter, the electrode was washed with PBS to remove the non-immobilized antibody. 1% BSA solution (400 µL) was dropped onto the anti-SARS-CoV-2/EDA-GCF electrode and kept for 1h at 4 °C to block the unspecific sites of the immunosensor. Finally, the anti-SARS-CoV-2/EDA-GCF immunosensor was used to bind SARS-CoV-2 SP with varying concentrations. After each addition, the system was allowed to equilibrate for 30 min at 4 °C, then washed with PBS (pH 7.4) prior to the electrochemical analyses.

Section 3.2 Nanomaterials based therapeutic systems for ovarian cancer

3.2.1 Drug delivery systems

3.2.2 Materials and Reagents

Pristine h–BN (purity 99.5 %, ~325 mesh powder), sulfuric acid (98%), KMnO4 (≥99%), H2O2 (30 Wt.% in water) and bovine serum albumin (≥92%) were purchased from Sigma Aldrich. Phosphate buffers were purchased by Thermo Fisher scientific. A Millipore Milli Q Biocell A10 water purifying system was used to prepare ultrapure water. Fetal bovine serum (tetracycline free)

was purchased from Euro lone. A2780 (Sigma-Aldrich, St. Louis, MO, USA), OVCAR-3, HCT-116 and MRC-5 (ATCC, Manassas, VA, USA) cell lines were grown accordingly to manufacture's instruction. LysotrackerTMGreen DND-26, Hoechst 33342 and rhodamine B were purchased from Thermo Fisher Scientific (Waltham, Massachusetts, USA).

3.2.3 Apparatus and measurements

A field-emission scanning electron microscopy (FE-SEM, Carl Zeiss Sigma VP, Germany) and a high-resolution transmission electron microscope (HR-TEM, JEM-2100 (HRP)) was utilized to analyze the morphology of the synthesized hydroxylated boron nitride nanoparticles (OH-BN). HR-TEM was used to characterize the selected area diffraction pattern (SAED) and the lattice fringe. X-ray diffractometer (XRD, Philips) with a Cu Kα radiation (λ = 1.5406 Å) and Fourier-transform infrared (FTIR) spectrophotometer (MIDAC, M4000) were used to characterize the structural properties of OH-BN. The functional groups of the sample were measured by XPS (Thermo Scientific™, Thermo Fisher Scientific, UK) using Al–Kα as a monochromatic x-ray source. The optical absorption spectra were obtained by a UV–vis spectrophotometer (Lambda 35, Perkin Elmer, USA). Raman spectra (Horiba Scientific, XploRA PLUS, France) were acquired under ambient temperature with a laser having excitation wavelength of 532 nm. To calculate IC50 values, luminescence was read with a Tecan infinite M1000 Pro instrument (Tecan, Männedorf, Switzerland). AnnexinV was evaluated with BD FACSCantoII instrument (BD Bioscences, San Jose, CA, USA). Fluorescence images were capture with a Nikon Ti eclipse inverted microscope (Nikon, Minato City, Tokyo, Japan).

3.2.4 Synthesis of hydroxylated Boron Nitride

A very simple method has been utilized to synthesize hydroxylated boron nitride nanoparticles with the modification of a literature method[5]. Briefly, 2 g of pristine BN powder was mixed into H_2SO_4 (98%, 50 mL) solution with gentle stirring for 30 min. Then, 1g of $KMnO_4$ was added gradually into the above solution set previously at 0 °C and stirred for 12 h. Subsequently, 5 mL of H_2O_2 (30% w/w solution water) was added to the mixture and stirred again for 5 h. The resulting solution was centrifuged at 3000 rpm for 10 min to separate the large size BN particles. Later, the supernatant was sequentially washed with water until the leached solution reached pH 7.0. Finally, the obtained powder was dried in an oven at 40 °C, kept under vacuum for 24 h.

3.2.5 Artificial *in vivo* Stability Test of hydroxylated Boron Nitride

The artificial *in vivo* environments were mimicked by mixing 1 mg/mL of OH-BN into serological solution, pH. 7.4, that was put into sealed tubes. The serological solution, containing fetal bovine serum, was prepared according to a previously reported protocol[6]. The sealed tubes were placed into the incubator set at 37 °C, in the dark (to make exactly body-like environment). At different time intervals, tubes were taken out for further characterizations. In a similar way, an *in vivo* tumour environment was created by adjusting to pH 5.5 the serological solution and the n performing same stability tests as those for pH.7.4 conditions.

3.2.6 Loading and Release of Doxorubicin on OH-BN Nanoparticles

The loading of doxorubicin on OH-BN was performed by simple mixing of OH-BN (10 mg) with doxorubicin solution (1mL, with total concentration of 2mg/mL) at room temperature on the rotator overnight. Later, the suspension was centrifuged (10,000 RPM) and washed several times

with PBS solution. The loading efficiency was calculated by measuring the drug in the supernatant, compared to the initial amount of the drug. The nanoparticles load was evaluated to be around 40-45 %. The release experiment was performed at two different pH (i.e., 5.5 and 7.4). Briefly, 200 µL of OH-BN nanoparticles loaded with doxorubicin (OH-BN/Doxo) were put onto the dialysis membrane, which was sealed from the top side, thus avoiding the solution to evaporate. The dialysis membrane was incubated in 1 L PBS (pH. 7.4 and 5.5) on a hot plate at 37 °C, while gentle stirring. The measured drug concentration was evaluated after taking solution off from the dialysis membrane at each interval time, specifically at 1 h, 3 h, 6 h, 12 h, 24 h, 48 h, 72 h and 96 h). For comparison the bulk boron nitride material was used for the same loading and release experiments.

3.2.7 The IC50 treatment

The OH-BN were tested on different cell lines that were seeded in 96 multiwell plates at the concentration of $1x10^3$ cancer cells or $8x10^3$ normal cells. Cell viability was measured using the CellTiter-Glo® assay system according to the manufacturer's instructions (Promega, Madison, Wisconsin, USA) after 96 hours. Six serial dilutions 1:10 of the OH-BN and BN suspensions were utilized to calculate the IC50 values with GraphPad software utilizing the non-linear regression method.

Section 3.3 Carrier Free Delivery Systems

3.3.1 Materials and Reagents

Human serum albumin (HAS, ≥96%), hexadecyltrimethylammonium bromide (CTAB, ≥ 98%), Pluronic® F-127 (suitable for cell culture and acetonitrile) were purchased from Merck, Darmstadt, Germany. For Bradford protein assay, dye reagent was purchased from Bio-Rad, Hercules, CA, US; methanol for LC/MS was purchased from Carlo Erba, Milan, Italy; chloroform

from Thermo Fisher Scientific, Waltham, MA, US. Water was purified with Milli-Q® (Millipak® 0.22μm) system. Compound MAGL23 was synthetized as previously reported method.

3.3.2 Apparatus and measurements

The apparatus utilized in this experiment (MAGL) was same as those described in section 2.1.2.

3.3.3 Nanocrystallization and Albumin Formulation

The nanocrystallization of MAGL23 was carried out by following the method reported in the literature[7]. Typically, 6 mg of the drug and 24 mg of Pluronic F-127 (F-127) were mixed in 3 mL of chloroform inside a round-bottom flask. The mixture was mixed to ensure the complete dissolution of the drug. Later on, chloroform was evaporated while putting the round-bottom flask containing the solubilized drug and surfactant onto a hot plate, kept at 30°C. A thin amorphous layer of the mixture was achieved into the walls on the round-bottom flask; it was further recovered in 6 mL of milli-Q water attaining a final drug concentration of 0.82 mg/mL. To recover fully the nanocrystals in water, bath sonication (1 min) and probe sonication (10 min, with 40% frequency) was performed and the resultant solution contained the solubilized nanocrystals of drug. The same procedure was employed by replacing 24 mg of F-127 with 2.4 mg of CTAB to check the solubility and other effects through in vitro study on different cell lines.

To formulate the drug nanocrystals for safe in vivo applications, 4 mg of HSA were mixed with 1mL nanocrystals solution of drug at room temperature on rotation (30 rpm), for 24h. This ensured the maximum coverage or interaction between HSA and nanocrystal surfaces. Later, the samples were centrifugation (38000 rpm, 4°C) for 1h to remove the unbounded albumin and remaining extra surfactants. Lastly, the nano crystal pellet was lyophilized and resuspended in milli-Q water while maintaining the same starting volume (1 mL) for further experiments.

3.3.4 Solubility Test of Drugs

The solubility of the inhibitor was calculated theoretically and confirmed with experimental tests. The theoretical prediction was obtained by the "Chemicalize" software (Chemicalize.com; ChemAxon Ltd., Budapest, Hungary). The theoretical solubility of the drug was calculated at different pH[8]. Experimental results were performed by dissolving 1 mg/mL of drug powder in milli-Q water for 1 hour. Then the solution was centrifuged at 10000 rpm for 10 minutes to separate the insolubilized fraction of the compound, which was further examined quantitatively through UV-Visible spectroscopy analysis.

3.3.5 Yield and Formulation

The yield of the nanocrystals was obtained d by UV-Vis measurements at 252 nm (Agilent 8453 spectrophotometer) through a calibration curve procedure. The concentration of the drug nanocrystals was quantified by diluting the solution in methanol, then it was centrifuged (12000 rpm, 2 min) to precipitate HAS. Finally, the amount of drug present in the supernatant was detected. The yield % of the nanocrystal formulation was measured as the concentration of the formulated nanocrystals at final stage, over the amount of the drug utilized for the nanocrystal production; the ratio was then multiplied by 100 to get values in percentage. The quantity of protein (HAS) was analyzed by Bradford protein assay (Bio-Rad reagent) through Agilent 8453 spectrophotometer (λ=595nm) and using a calibration curve freshly constructed for HAS. The percentage of HSA bound to drugs nanocrystals was calculated by the same method as mentioned above for drugs yield quantification.

3.3.6 Cell Viability

Ovarian cancer (A2780, KURAMOCHI, SKOV3, OVCAR3) and colorectal cancer (Colo201, Colo205, HCT116) cell lines and lung fibroblasts (MRC-5) were grown, according to the supplier instructions, at 37 °C in a controlled atmosphere containing 5% CO2. A thousand of cancer cells were plated in 96-multiwell culture plates or 5000 cells for MRC-5. The day after seeding, drugs were added with a serial dilution 1:10 to have a final concentration ranging from (100 µg/mL) to (0.001µg/mL). Cell viability was measured with Tecan Infinite M1000 PRO (Tecan, Mannedorf, Switzerland) after 96h with CellTiter-Glo® assay according to the supplier (Promega, Madison, WI, US) instructions. Cell viability data were analyzed using a nonlinear regression dose-response curves by GraphPad Prism 8 Software. The experiments were performed in triplicated to obtain average values, relevant errors and standard deviations.

3.3.7 Release Profile

The drugs release profile was obtained through dialyzing 1 mL of drugs against PBS (pH 7.4, isotonic solution) placing the nanocrystal sample in a Slide-A-Lyzer MINI Dialysis Device 20k MWCO (Thermo Scientific) placed at 37°C. Aliquots of the solution were collected at different times and then measured with Agilent 1260 Infinity II HPLC with a Variable Wavelength Detector, equipped with an Accucore-150-C18 column (5 cm x 2.1 mm, particle size 2.6 µm) (Thermo Fisher Scientific, Waltham, MA, US). A mixture of acetonitrile and MQ water 50:50 was used as mobile phase with a flow rate of 0.5 mL/min. The quantification of the inhibitor was measured using a 252 nm wavelength and a previously constructed calibration plot. Aliquots of the solutions were processed before HPLC analysis to remove HSA. The nanocrystal samples were diluted into acetonitrile and centrifuged at 13000 g for 15 minutes, then the supernatant was further diluted 1:1 with MQ water.

3.3.8 Lysotracker Analysis

The internalization and localization of the drug nanocrystals into the cells were analyzed. Typically, 150,000 cells were plated on top of a sterile coverslip into transparent microplate wells. The fluorescent dye rhodamine B (30 µg/mL) was mixed with nanocrystals under continuous rotation at room temperature for an hour. Then, 50 µg/mL of the rhodamine B-nanocrystals were added into each well for different times (1h, 6h, and 24h). After incubation, the media was removed from the cells and new media was added with 200 nM of LysotrackerTMGreen DND-26 (Thermo Fisher Scientific, Waltham, MA, US) to label lysosomes and 0.02 ng/mL Hoechst 33342 for three hours to label the cell nucleus. Subsequently, the media was removed, and cells were washed three times by PBS and fixed with paraformaldehyde 4% for 20 minutes. The cells were analyzed with an inverted fluorescence microscope (Nikon, Tokyo, Japan).

Section 3.4 Self-therapeutic nanomaterials-based system

3.4.1 Materials and Reagents

The materials and reagents of this systems already stated in section 3.1.1.

3.4.2 Synthesis of $Co(OH)_2$ NS

The synthesis is reported in detail in section 3.1.3.

3.4.3 Cell viability

The $Co(OH)_2$ NS were treated on different cell lines that were seeded in 96 multiwell plates at the concentration of $1x10^3$ (cancer cells) or $8x10^3$ (MRC-5) cells. Cell viability was measured using the CellTiter-Glo® assay system according to the manufacturer's instructions[9] (Promega, Madison, Wisconsin, USA) after 96 hours. Six different serial dilutions 1:10 of the compounds

were utilized to perform the IC50 analysis and the results were analyzed with GraphPad software using the non-linear regression method.

3.4.4 Stability of $Co(OH)_2$ NS

An artificial in vivo system was prepared by mixing Co(OH)2 NS (3mg/mL) in physiological solutions having two different pH (pH 5.5 & pH 7.4). Then, the solutions were placed in an incubator at 37 °C. The samples were collected at different day intervals (zero- seven; DO, D1, D2, D3, D5 & D7, respectively), centrifuged, and collected. Then, the UV-Vis absorption spectra of the samples were acquired by dispersing them in DI water.

3.4.5 Intracellular localization

The internalization and localization of the $Co(OH)_2$ NS into the cells were observed with fluorescent probes. Typically, 150,000 cells were seeded into a transparent microplate containing a glass coverslip. To label $Co(OH)_2$ NS, 30 µg/ml of rhodamine B was mixed with $Co(OH)_2$ NS through continuous rotation at room temperature for one hour. Subsequently, cell lines were treated with 50 µg/mL of $Co(OH)_2$ NS for different time (1h, 6h, and 24h). After two times washing with PBS, cells were incubated according to the manufacturer's instructions with 200 nM of Lysotracker™Green DND-26 (ThermoFisher scientific) and 200 ng/mL Hoechst 33342 for lysosomes and nuclear staining, respectively. Later, cells were fixed with paraformaldehyde 4% for 20 minutes and the coverslip was mounted using Fluorsave mounting media (Merck Millipore, Burlington, MA, USA) for cellular imaging. Hoechst, LysoTracker Green DND-26 and Rhodamine B were detected under a fluorescence microscope with suitable filters. Images were analyzed with ImageJ and JacoP plugins.

3.4.6 Flow cytometry analysis

3 x 10^5 A2780 cells were cultured as indicated by the supplier for indicated time points. Annexin V analysis was performed using PE-Annexin V Apoptosis Detection Kit from Becton-Dickinson (Franklin Lakes, NJ, US) according to manufacturer's protocol using FACS Canto II from Becton-Dickinson (Franklin Lakes, NJ, US) and BD FACS DIVA software.

3.4.7 Cancer Organoids

Cancer organoids were generated from totally anonymized specimens. However, biobank informed consent for research purposes was available to collect the samples at National Cancer Institute (CRO) of Aviano. HGSOC specimens from ascites and tumor tissues were collected to generate organoids. Briefly, fluids were centrifuged (1000 rpm, 10 min) and cell pellets were washed in Hanks' Balanced Salt solution for two times (HBSS, Gibco Cat. No. 14175-053). Cold Red blood cell lysis Buffer (Roche Diagnostics, Cat. No. 30020500) was added for erythrocytes lysis. After 10 min on ice, cells were centrifuged and resuspended in Cultrex growth factor-reduced Basement Membrane Extract (BME), Type2 (R&D Systems Cat. No. 3533-001-02). Differently, solid tumor tissue specimens were washed for 30 minutes in Dulbecco' s Modified Eagle's medium/Nutrient Mixture F-12 Ham with antibiotics (Levofloxacin 100ug/mL, Vancotex 25ug/ml, Ciproxin 5ug/ml, Gentamicin 200ug/mL, Fungizone 5ug/mL). Then, tissues were minced with a fine scissors, treated with 2 mg/mL of collagenase type I (Gibco Cat. No:17018029) at 37 °C for 20 min. and mechanically dissociated by repetitive pipetting. After centrifugation, tissue fragments were resuspended in Cultrex growth factor reduced BME, Type2. Both ascites and tissue organoids were seeded on prewarmed 24-well cell culture plate, and after cultrex

solidification, 450µl of organoid medium derived from Kopper et al., [10] was added to each well. Medium was subsequently refreshed every 2-3 days.

3.4.8 Histopathology analysis

Sections of formalin-fixed, paraffin-embedded ascites and solid tumour organoids were used for histopathological analyses. Organoids were collected, fixed in phosphate-buffered 10% formalin, and embedded in paraffin using Micro NextGen CellBloking™ Kit (Cat n°: M20; AV Bioinnovation) following manufacture instructions. Subsequently, 5µm sections were stained with haematoxylin and eosin (H&E) by using the Leica ST5020 multistainer and 2µm sections were cut for immunohistochemistry (IHC) analysis. IHC staining was performed with UltraVision LP Detection System HRP DAB kit (Thermo Scientific, Waltham, USA). Heat-induced antigen retrieval was performed using 10 mM citrate buffer pH 6.0. The following antibodies were used to characterize patient's derived organoids and parent tumour: PAX8 (ProteinTech Group, Germany, EU; 10336-1-AP); Ca125 (Santacruz Biotechnology, TX, US; sc-52095); WT1 (Abcam, UK; ab89901). Tissues were analysed with a light microscope using different magnifications.

3.4.9 Statistical analysis

Statistical analysis was performed with GraphPad Prism software and a p-value <0.05 was considered significant.

References

[1] B. N. Bhadra, P. W. Seo, N. A. Khan, S. H. Jhung, *Inorg. Chem.* **2016**, *55*, 11362.

[2] M. V. Mirkin, W. Nogala, J. Velmurugan, Y. Wang,. *Phys. Chem. Chem. Phys.* **2011**, *13*, 21196–21212.

[3] L. Ying, L. Yue-Ping, D. Bo, R. Feifei, W. Yue, D. Jinya, H. Qianchuan, *medRxiv* **2020**.

[4] B. Mojsoska, S. Larsen, D. A. Olsen, J. S. Madsen, I. Brandslund, F. A. Alatraktchi, *Sensors* **2021**, *21*, 1.

[5] M. Adeel, M. M. Rahman, J. J. Lee, *Biosens. Bioelectron.* **2019**, *126*, 143.

[6] D. Li, X. Hu, S. Zhang, *Biomaterials* **2019**, *202*, 12.

[7] J. Park, B. Sun, Y. Yeo, *J. Control. Release* **2017**, *263*, 90.

[8] E. J. Barbosa, R. Löbenberg, G. L. B. de Araujo, N. A. Bou-Chacra,. *Eur. J. Pharm. Biopharm.* **2019**, *141*, 58–69.

[9] M. Lapillo, B. Salis, S. Palazzolo, G. Poli, C. Granchi, F. Minutolo, R. Rotondo, I. Caligiuri, V. Canzonieri, T. Tuccinardi, F. Rizzolio, *ACS Med. Chem. Lett.* **2019**, *10*, 475.

[10] O. Kopper, C. J. de Witte, K. Lõhmussaar, J. E. Valle-Inclan, N. Hami, L. Kester, A. V. Balgobind, J. Korving, N. Proost, H. Begthel, L. M. van Wijk, S. A. Revilla, R. Theeuwsen, M. van de Ven, M. J. van Roosmalen, B. Ponsioen, V. W. H. Ho, B. G. Neel, T. Bosse, K. N. Gaarenstroom, H. Vrieling, M. P. G. Vreeswijk, P. J. van Diest, P. O. Witteveen, T. Jonges, J. L. Bos, A. van Oudenaarden, R. P. Zweemer, H. J. G. Snippert, W. P. Kloosterman, H. Clevers, *Nat. Med.* **2019**, *25*, 838–849.

Chapter 04: Results and Discussion

Section 4.0 Electrochemical sensors for Glucose Detection

The electrochemical glucose sensors were fabricated using the nanozymes 2D Metal Azolate Framework (i.e., MAF-5) and $Co(OH)_2$ nanosheets. For the sake of simplicity of presentation, this main section is divided in two main **sub-sections** devoted to the **MAF-5 and $Co(OH)_2$** results.

Section 4.1 Electrochemical measurements of 2D MAF-5-Co^{II} NS for glucose oxidation

The graphical abstract of the work is illustrated in **Figure 4.1**

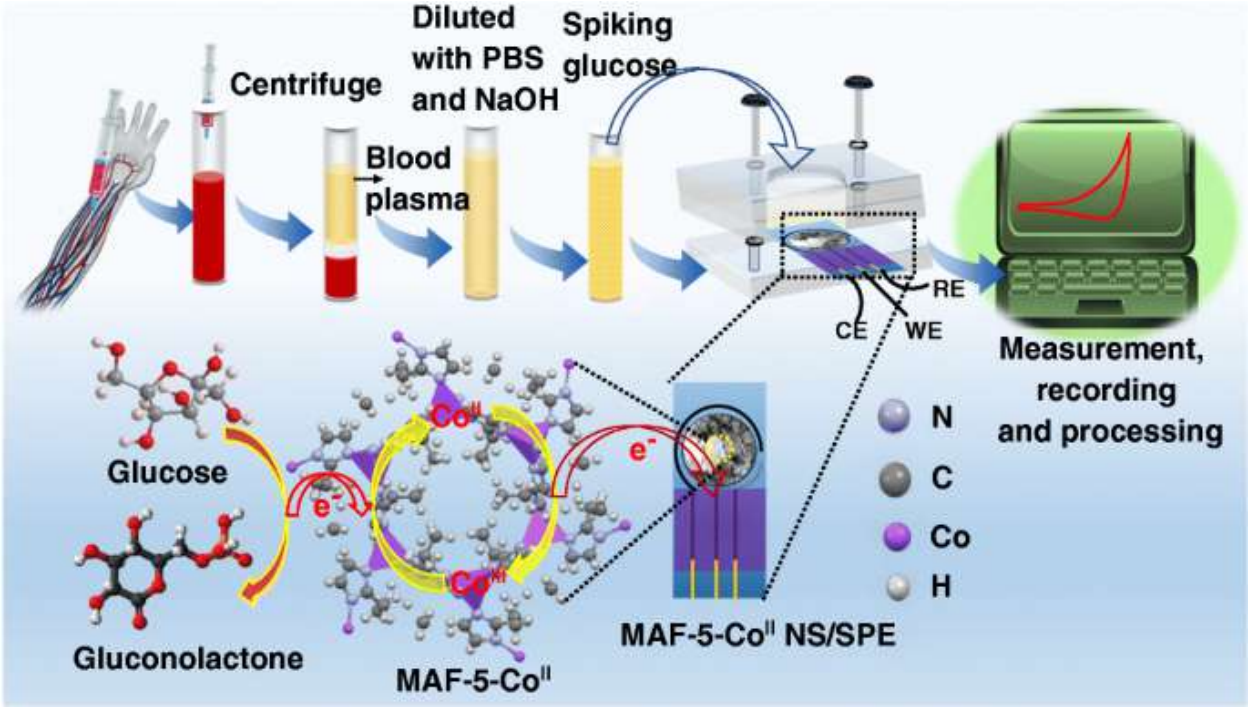

Figure 4.1.: Schematic Illustration of MAF based Glucose Sensor (copy right Adeel et al.2021).

4.1.1 XRD, FTIR, and surface area analyses of MAF-5-Co^{II} NS

A simple room temperature method was employed to synthesize pure MAF-5-CoII NS as shown in **(Figure 4.1.1a)**. (**Figure 4.1.1b)** shows the X-ray diffraction (XRD) pattern of the synthesized MAF-5-CoII NS, of $Co(OAc)_2$ precursor and that simulated for MAF-5 (Zn). The XRD pattern of MAF-5-CoII NS and MAF-5 (Zn) matches well, indicating that MAF-5-CoII NS is isostructural with MAF-5 (Zn)[1]. No additional peak of unreacted Co(OAc)2 precursor was observed, denoting the successful synthesis of MAF-5-CoII and its high purity. Moreover, the sharp and intense major XRD peaks of MAF-5-CoII with the hkl reflections of (211), (220), (321), (400), (332), and (521) at 2θ angle values of ca. 8.05, 9.51, 12.25, 13.25, 15.51, and 18.25°, respectively, point to its high crystallinity. FTIR spectra of MAF-5-CoII NS and EIM were measured to investigate the nature of the chemical bonding, and they are shown in **(Figure 4.1.1c)**. The FTIR spectrum of EIM shows the characteristics strong absorption bands of C-N, C=N, and C=C stretching at ca. 1046, 1457, and 1570 cm-1, respectively, together with a wide band of N-H stretching in the range of ca. 2500-3150 cm-1 [1,2]. The synthesized MAF-5-CoII NS shows a similar strong absorption band of C-N, C=N, and C=C at ca. 1050, 1450, and 1570 cm-1, respectively. However, the FTIR spectra of MAF-5-CoII NS exhibits a strong decrease of the N-H stretching band and the appearance of a strong band at 610 cm-1. The latter can be assigned to the Co-N stretching, due to the formation of a Co-N coordination bond[3], and thus confirming the effective synthesis of MAF-5-CoII NS.

The surface area (SABET) of the MAF-5-CoII NS was measured from the N2 adsorption isotherm **(Figure 4.1.1d)**. SABET of ca. 1155 m2/g was found. The high SABET MAF-5-CoII NS is advantageous, as it allows increasing the number of catalytically active sites, and this can provide an increased rate of reaction.

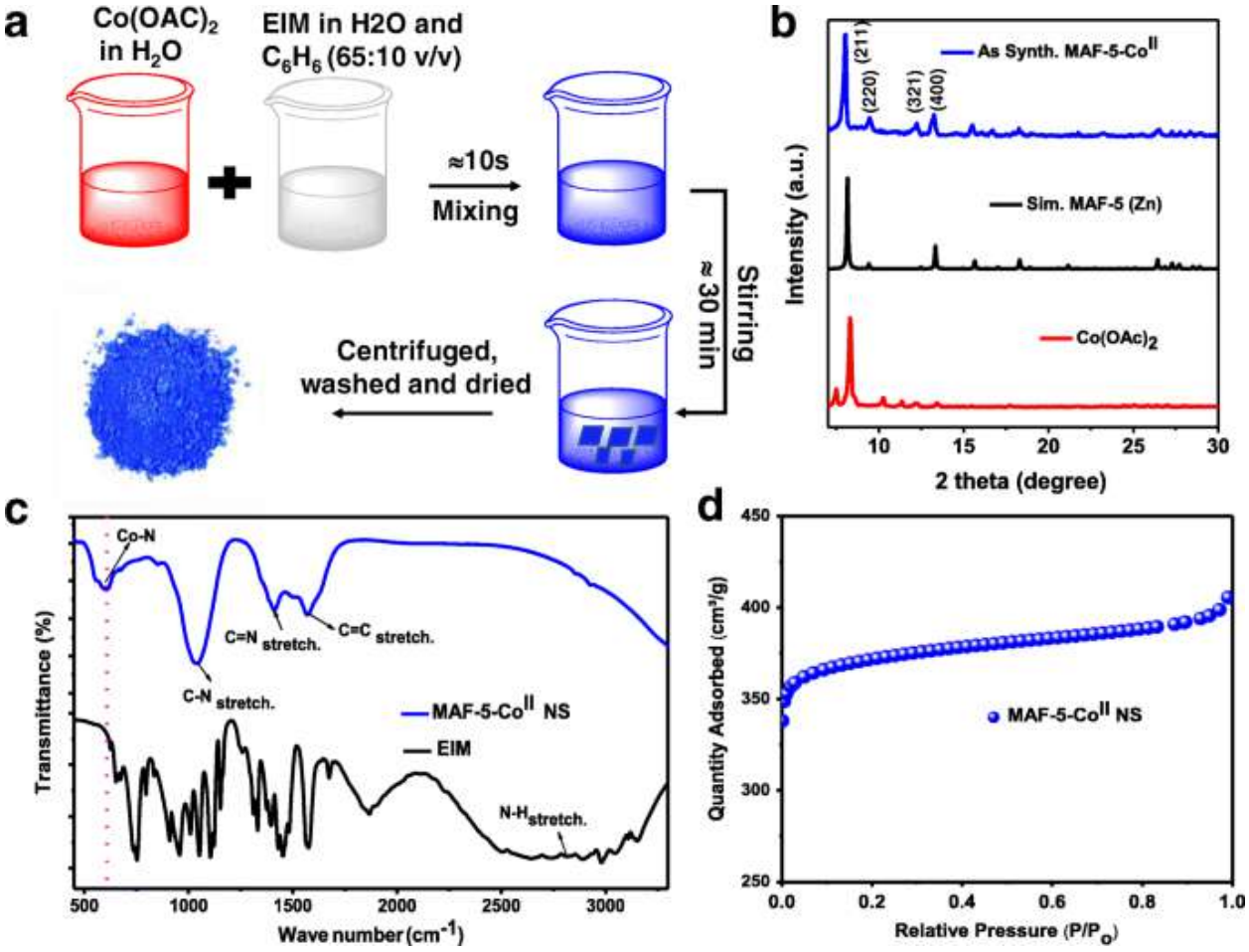

Figure 4.1.1 (a) schematic of the synthesis of MAF-5-Co^{II} NS. (**b)** XRD patterns of MAF-5-Co^{II} NS and $Co(OAc)_2$ precursor together with simulated XRD pattern of MAF-5 (Zn). (**c)** FTIR spectra of MAF-5-Co^{II} NS and EIM. (**d)** N_2 adsorption isotherm of MAF-5-Co^{II} NS (copy right Adeel et al.2021).

4.1.2 Morphological characterization of MAF-5-Co^{II} NS

The surface morphologies of the MAF-5-CoII NS were analyzed by FE-SEM and HR-TEM. The FE-SEM image of MAF-5-CoII NS **(Figure 4.1.2a)**, represented the formation of two-dimensional (2D) nanosheets (NS). The HR-TEM results **(Figure 4.1.2b)** further evidence for the formation of 2D MAF-5-CoII NS. The high transparency of the electron beam of the MAF in the HR-TEM image indicates the formation of ultrathin layer of NS without the presence of any aggregations.

The SAED pattern of the MAF-5-CoII NS demonstrated a bright ring pattern with bright spots with the hkl reflections of (211), (220), and (321) **(Figure 4.1.2c)**. This agrees with the XRD findings and further support the excellent crystallinity of MAF-5-CoII NS. The EDS study of MAF-5-CoII NS **(Figure 4.1.2d)** provided, effectively peaks due to Co, N, and C atoms, the Cu peaks being appeared from the HR-TEM grid, hence further signifying the formation of MAF-5-CoII NS with high purity[3].

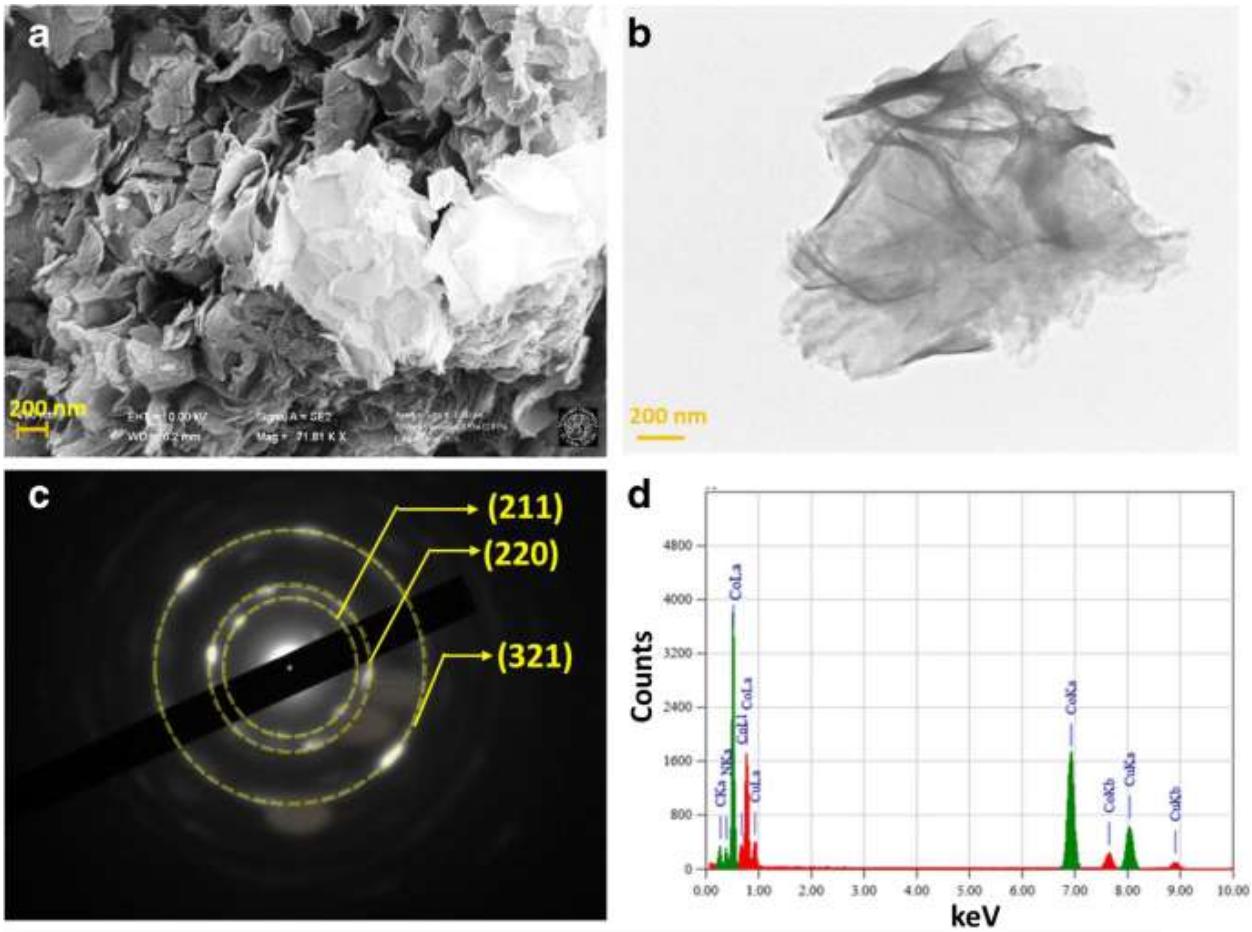

Figure 4.1.2 (a) FE-SEM and **(b)** HR-TEM images of MAF-5-CoII NS. **(c)** SAED pattern and **(d)** EDS spectra of MAF-5-CoII NS (copy right Adeel et al.2021).

4.1.3 XPS characterization of MAF-5-Co^{II} NS

The elemental composition and the oxidation state of Co in MAF were examined by XPS. (**Figure 4.1.3a)** represents a survey XPS spectrum (100-900 eV) of MAF-5-CoII NS, in which the characteristic peaks of Co, N, and C elements appear. The additional peak feature of elemental O appears, possibly, from chemisorbed O_2. **Figures. 4.1.3 (b-d)** show the core-level XPS spectra of C 1s, N 1s, and Co 2p, respectively. The fitted high-resolution spectrum of C 1s presents three peaks with variable intensity at the binding energies (BE) of 283.40, 284.80, and 287.50 eV. This could be assigned to the existence of C-C/C=C, C-N, and C=N bonding characteristics, respectively, in the MAF-5-CoII NS, and this agree well with literature reports[1]. The de-convoluted core-level N 1s spectrum indicates two peaks of C=N and C-N at the BEs of 397.60 and 398.70 eV, respectively[3]. The bonding nature of C-C and C-N in the C 1s and N 1s spectra suggests the presence of EIM linkers in the MAF-5-CoII NS. The high-resolution XPS spectra of Co 2p exhibit two main peaks at the BEs of ca. 779.80 and 795.60 eV with the separation of 15.8 eV, which agrees with the previous literature reports. The former peak could be assigned to the Co 2p3/2, while the other to the Co 2p1/2. Both Co 2p3/2 and Co 2p1/2 peaks indicated their corresponding strong satellite peaks at the BEs of ca. 784.22 and 801.30 eV, respectively, this suggests the oxidation state of Co in the MAF is +2[3].

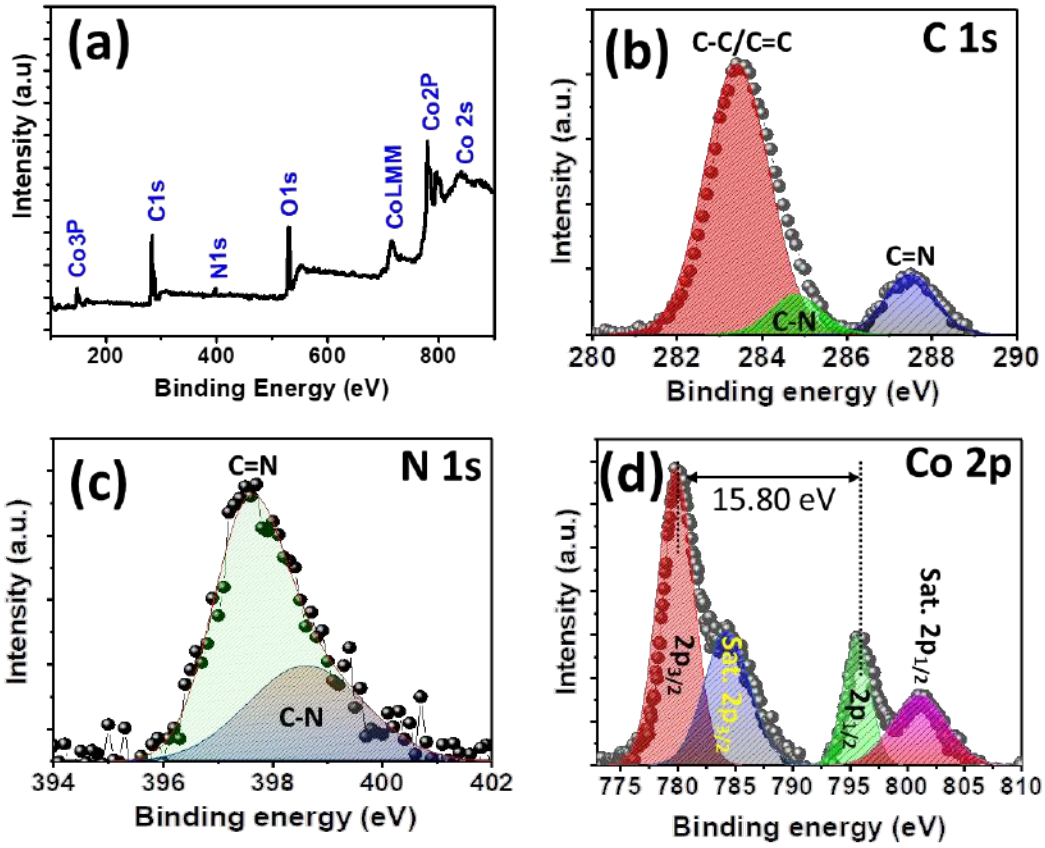

Figure 4.1.3 (a) XPS survey spectra of MAF-5-Co^{II} NS. High-resolution XPS spectra of (**b)** C 1s, (**c)** N 1s, and (**d)** Co 2p in MAF-5-Co^{II} NS (copy right Adeel et al.2021).

4.1.4 Electrochemical measurements of MAF-5-Co^{II} NS for glucose oxidation

(Figure 4.1.4 a) show the graphic representation of the synthesis of the MAF-5-Co^{II} NS modified SPE electrode (MAF-5-Co^{II} NS/SPE).

(Figure 4.1.4 b) shows CVs recorded at bare SPE and MAF-5-Co^{II} NS/SPE in PBS, in the absence and presence of 2 mM of glucose. As a result, at the bare SPE, in both cases, negligible currents were observed. This agrees with results reported for carbon-based electrodes previously, where, glucose oxidation was recorded essentially, over the examined potential zone in this research. However, a small anodic/cathodic characteristic at potentials anodic to 0.3 V are observed on MAF-5-Co^{II} NS/SPE, this may be due to the Co^{2+}/Co^{3+} redox couple of the

nanostructured material. A series of measurements was performed at different scan rates **(Figure 4.1.4 c)** using MAF-5-Co^{II} NS/SPE. Results demonstrated that both anodic and cathodic current densities for glucose oxidation increased with the increase of scan rate. The anodic current density (J) at 0.4 V was proportional to the square root of the scan rate (inset of **Figure 4.1.4 c**, the linear regression analysis of experimental data provided the equation J ($\mu A/cm^2$) = 1.57 ($\pm$0.02) $\times$ $\nu^{1/2}$ $(mV/s)^{1/2}$ – 2.14 ($\pm$ 0.21; R^2 = 0.997), indicating the occurrence of a diffusion-controlled oxidation process.

A similar set of data was obtained as described above in PBS, was recorded in 0.1 M NaOH solution. (**Figure 4.1.4 d)** shows CVs obtained at SPE and MAF-5-Co^{II} NS/SPE with no glucose and in the presence of 2 mM of glucose. As expected, bare SPE did not showed any redox activity both in the absence and presence of glucose. MAF-5-Co^{II} NS/SPE showed a couple of oxidations (I) and reduction (I') peaks at ca. 0.35 and 0.17 V, respectively, that can be ascribed to the Co^{II}/ Co^{III} redox system of the MAF nanostructured material. A similar justification was given for other MAF family like MAF-4-Co^{II}, MIL-53-Cr^{III}, and CPO-27-Ni^{II}, containing the redox couple of the metal ions present in their structures[2,4]. In the presence of 2 mM glucose in 0.1 M NaOH solution, offered an increase of the oxidation current density with a shift towards less positive values indicating a clear clue of the high electrocatalytic activity of MAF-5-Co^{II} NS for electrocatalytic oxidation of glucose to gluconolactone. Scan rates analysis by CV was performed over the range 10 - 100 mV/s, also revealed that the oxidation peak current density of glucose is proportional with the square root of the scan rate (**Figure 4.1.4 e** and inset of **Figure 4.1.4 e**). The linear regression analysis of the experimental data providing the equation J ($\mu A/cm^2$) = 102.60 ($\pm$ 1.61) $\times$ $\nu^{1/2}$ $(mV/s)^{1/2}$ – 203.10 ($\pm$ 11.97) (R^2 = 0.998), indicating the existence of a diffusion-controlled oxidation process of glucose[5].

The enzymeless electrochemical oxidation of glucose at the MAF-5-Co^{II} NS/SPE, in both PBS and NaOH solutions, can be summarized as follows:

$$MAF\text{-}5\text{-}Co^{II} \rightarrow MAF\text{-}5\text{-}Co^{III} + e^{-} \quad (1)$$

$$MAF\text{-}5\text{-}Co^{III} + glucose \rightarrow MAF\text{-}5\text{-}Co^{II} + gluconolactone + 2H^{+} \quad (2)$$

A schematic illustration of the mechanism is also provided in **Figure 4.1.4f**. Therefore, the porous structure with high surface area of MAF-5-Co^{II} NS favor the interaction between the active form of MAF (i.e., the Co(III) site) with glucose.

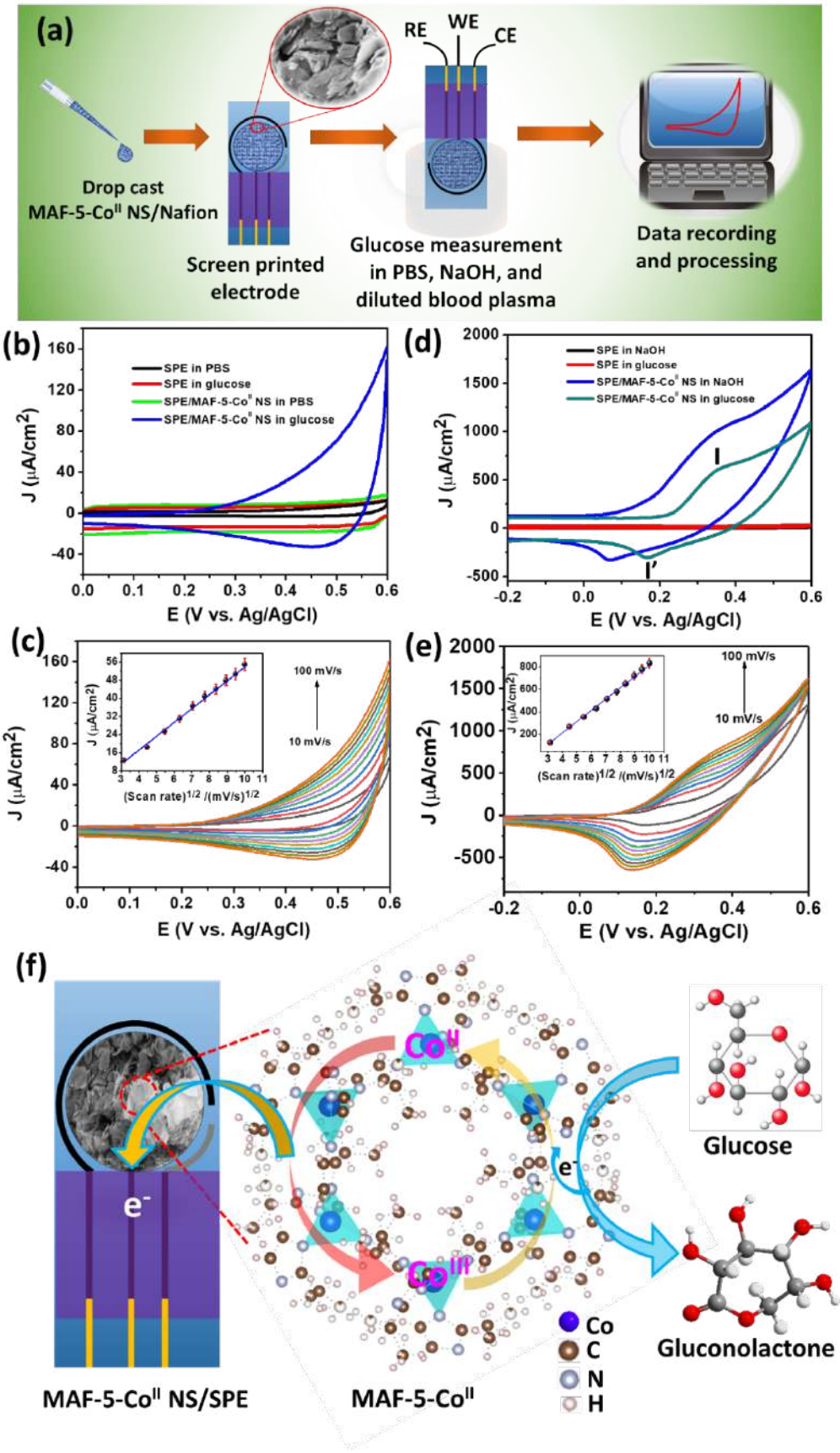
(a)
RE
WE
CE
Drop cast
MAF-5-Co^{II} NS/Nafion
Screen printed electrode
Glucose measurement in PBS, NaOH, and diluted blood plasma
Data recording and processing
(b)
SPE in PBS
SPE in glucose
SPE/MAF-5-Co^{II} NS in PBS
SPE/MAF-5-Co^{II} NS in glucose
J (μA/cm^2)
E (V vs. Ag/AgCl)
(d)
SPE in NaOH
SPE in glucose
SPE/MAF-5-Co^{II} NS in NaOH
SPE/MAF-5-Co^{II} NS in glucose
I
I'
J (μA/cm^2)
E (V vs. Ag/AgCl)
(c)
100 mV/s
10 mV/s
J (μA/cm^2)
(Scan rate)$^{1/2}$ /(mV/s)$^{1/2}$
E (V vs. Ag/AgCl)
(e)
100 mV/s
10 mV/s
J (μA/cm^2)
(Scan rate)$^{1/2}$ /(mV/s)$^{1/2}$
E (V vs. Ag/AgCl)
(f)
e$^-$
Co^{II}
Co^{III}
e$^-$
Glucose
Gluconolactone
Co
C
N
H
MAF-5-Co^{II} NS/SPE
MAF-5-Co^{II}

Figure 4.1.4 (a) Schematic presentation of the fabrication of MAF-5-CoII NS/SPE sensor and glucose measurement. (b) CVs of SPE and MAF-5-CoII NS/SPE sensor in PBS in the absence and presence of glucose at a scan rate of 100 mV/s. (c) CVs of glucose (2 mM) in PBS at the MAF-5-CoII NS/SPE sensor with varying scan rates from 10 to 100 mV/s (inset shows the plot of anodic current density at 0.4 V vs. root over scan rate). (d) CVs of SPE and MAF-5-CoII NS/SPE sensor in NaOH solution in the absence and presence of glucose at a scan rate of 100 mV/s.(e) CVs of glucose (2 mM) in NaOH solution at the MAF-5-CoII NS/SPE sensor with varying scan rates from 10 to 100 mV/s (inset shows the plot of anodic peak current density vs. root over scan rate). (f) Possible mechanism for the electrocatalytic oxidation of glucose at the MAF-5-CoII NS/SPE sensor in both PBS and NaOH solutions (copy right Adeel et al.2021).

4.1.5 Detection of glucose in neutral and alkaline conditions

Chronoamperometry (CA) was used to examine the different concentration of glucose with respect to current density. This technique, the sensitivity is strongly depending on the amount of applied potential[2]. Different potential ranges were investigated from 0.35 to 0.55 V in PBS and from 0.3 to 0.45 V in 0.1 M NaOH. The steady-state currents at the various potentials are summarized in the insets (left sides) in (**Figures. 4.1.5a and b)**. It is observed that the steady-state current increases as the potential is set more positive. However, higher applied potentials may perhaps affect the selectivity of the sensor because of the presence of other oxidizing species. To minimize the interference effects without compromising too much the sensitivity, we selected 0.45 and 0.35 V for the detection of glucose in PBS and NaOH solution, respectively.

Figures 4.1.5a and 4.1.5b (main pictures) present the CA plots of different glucose concentrations in PBS and NaOH solution, respectively. The steady-state plots between oxidation current against glucose concentration are comprised in the insets (right side) of **Figures 4.1.5a and 4.1.5b**. The results showed that in both media, current responses increase by increasing the glucose concentration. However, linearity is noticed in two well-defined concentration ranges. All the parameters like dynamic ranges, linear regression equations, sensitivities and LODs under the different conditions are summarized in **Table 4.1.1**. The existence of the two linear ranges,

observed in the calibration plots, has also been reported in the literature for other family of MOFs. For the glucose oxidation, it was explained as due to the accumulation of gluconolactone oxidation product within the porous structure of the material. At low concentrations, glucose spread within the nanostructure and is promptly oxidized due to the presence of a large number of active sites, providing current responses described by high sensitivity. While, at higher glucose concentrations, the correspondingly higher oxidation product can act as a barrier for glucose diffusion, which leads to current responses of lower sensitivity[3,6].

The data shown in **Table 4.1.1** indicate that the analytical performance (e.g., sensitivity, LOD) of the sensor is better in NaOH solution than in PBS. This could be attributed to the improved efficiency of MAF-5-Co^{II}/MAF-5-Co^{III} redox pair in recycling its active form. In general, the analytical performance of the investigated sensor in PBS is comparable to others involving nanomaterial systems used for the non-enzymatic glucose oxidation. Therefore, MAF-5-Co^{II} NS showed a favourable low-cost material for the detection of glucose from biological fluids in physiological pH and alkaline media.

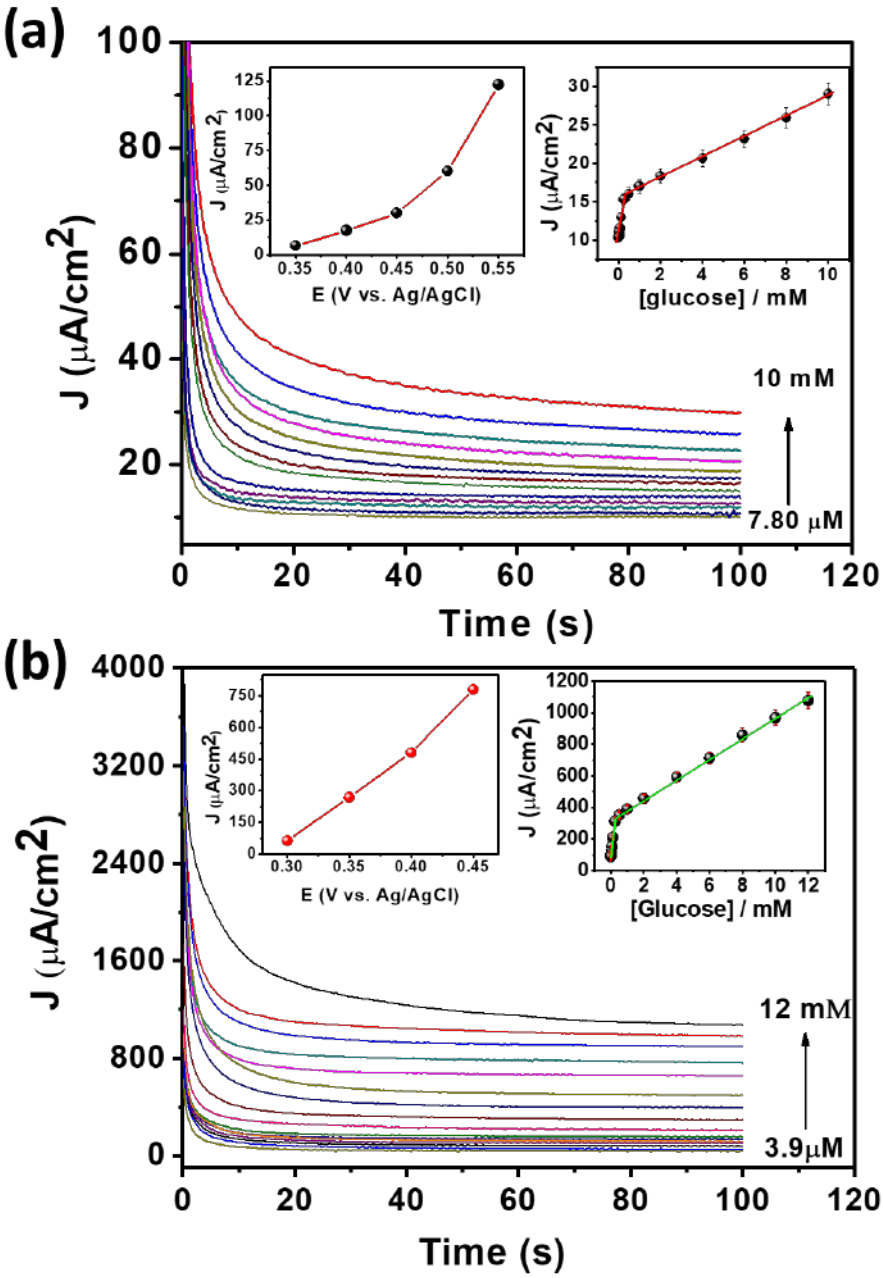

Figure 4.1.5 (a) CA responses of glucose oxidation in PBS with different concentrations from 7.80 to 10 mM (7.81, 15.6, 31.25, 62.6, 125, 250, 500, 1000, 2000, 4000, 6000, 8000, and 10,000 μM, respectively) at the MAF-5-Co^{II} NS/SPE sensor at an applied potential of 0.45 V (inset shows the plots of current density vs. applied potential for the oxidation of glucose (2 mM) and current density vs. [glucose] obtained from the CA responses). **(b)** CA responses of glucose oxidation in NaOH solution with varying concentrations from 7.80 to 10 mM (3.9, 15.6, 31.25, 62.6, 125, 250, 500, 1000, 2000, 4000, 6000, 8000, 10,000, and 12,000 μM, respectively) at the MAF-5-Co^{II} NS/SPE sensor at an applied potential of 0.35 V (inset shows the plots of current density vs. applied potential for the oxidation of glucose (2 mM) and current density vs. [glucose] obtained from the CA responses) (copy right Adeel et al.2021).

Medium	Dynamic Range	Linear regression equation (R^2)	Sensitivity $\mu A/cm^2/mM$	LOD μM
PBS	0.5 μM - 10 mM	$J\ (\mu A/cm^2) = 1.32\ (\pm 0.03) \times C_{Glu}\ (mM) + 15.50\ (\pm 0.13)\ (R^2 = 0.997)$	1.32	-
	7.81 μM - 250 μM	$J\ (\mu A/cm^2) = 24.22\ (\pm 1.50) \times C_{Glu}\ (mM) + 10.60\ (\pm 0.14)\ (R^2 = 0.985)$	24.22	0.30
PBS diluted BP	250 μM - 8 mM	$J\ (\mu A/cm^2) = 2.50\ (\pm 0.14) \times C_{Glu}\ (mM) + 7.45\ (\pm 0.70)\ (R^2 = 0.973)$	2.52	-
	7.81 - 125 μM	$J\ (\mu A/cm^2) = 36.55\ (\pm 1.55) \times C_{Glu}\ (mM) + 0.03\ (\pm 0.1)\ (R^2 = 0.993)$	36.55	0.25
NaOH	250 μM to 12 mM	$J\ (\mu A/cm^2) = 66.50\ (\pm 1.76) \times C_{Glu}\ (mM) + 313.0\ (\pm 6.20)\ (R^2 = 0.995)$	66.50	
	3.90 to 125 μM	$J\ (\mu A/cm^2) = 1012.70\ (\pm 25.90) \times C_{Glu}\ (mM) + 86.20\ (\pm 1.10)\ (R^2 = 0.997)$	1012.70	0.09
NaOH diluted BP	125 μM - 10 mM	$J\ (\mu A/cm^2) = 80.40\ (\pm 0.35) \times C_{Glu}\ (mM) + 118.70\ (\pm 1.70)\ (R^2 = 0.999)$	80.40	
	3.90 - 125 μM	$J\ (\mu A/cm^2) = 1361.65\ (\pm 78.51) \times C_{Glu}\ (mM) + 32.43\ (\pm 2.53)\ (R^2 = 0.988)$	1361.65	0.05

Table 4.1.1 Analytical performance of the MAF-5-Co^{II} NS/SPE sensor under various experimental conditions. C_{Glu} is the concentration of glucose (copy right Adeel et al.2021).

4.1.6 Detection of glucose in diluted blood plasma

For the real sample analysis, blood plasma (BP) samples were collected from 40 healthy volunteers without having diabetes at Centro di Riferimento Oncologico di Aviano, National Cancer Hospital, Italy. The normal (average) concentration of glucose in the BP is considered equal to 5.5 mM[6]. A series of PBS or 0.1 M NaOH solution–diluted BP samples (100 times) were spiked with glucose in the range from 3.9 μM to 10 mM. In these solutions, the total concentrations of glucose are the

sum of spiked concentrations and the normal concentration after dilution (55 μM). The corresponding CA plots for glucose oxidation at the MAF-5-CoII NS/SPE sensor are shown in **Figures 4.1.6 a and 4.1.6 b**, in PBS- and NaOH-diluted BP, respectively. In both cases, the steady-state current of glucose oxidation increased with increasing the concentration of glucose, which also demonstrated linear responses in two concentration ranges (insets of **Figures 4.1.6 a and 4.1.6 b**), as observed above in PBS and NaOH solutions (**Figures 4.1.5**). Dynamic ranges, linear regression equations, sensitivities, and LODs in both PBS and 0.1 M NaOH–diluted BP samples are summarized in **Table 4.1.1**. These results suggested that the MAF-5-CoII NS is suitable for the development of disposable type sensors for point-of-care detection of glucose concentration in biological fluids at physiological pH and alkaline medium.

4.1.7 Stability, interference studies, repeatability, and reproducibility

Long-term stability of the electrode materials is necessarily important to develop a reliable glucose sensor. These features were investigated by CA (**Figure 4.1.6c**) and CV **(Figure 4.1.6d)**, using diluted BP samples (with either PBS or 0.1 M NaOH), spiked with 2 mM of glucose. It was observed that after 1000s, the glucose oxidation currents decreased of 3.95 and 8.10%, in PBS and NaOH diluted BP samples, respectively, representing a perspective good stability for a series of point-of-care measurements. Furthermore, the stability of the sensor was also evaluated by performing a series of consecutive CVs, which better than CA can give information on the stability of the material over a larger potential range. **Figures. 4.1.6 d and 4.1.6 e** show the CV behavior noted during 100 consecutive cycles. After 100 CV cycles, the anodic current for the oxidation of glucose in both PBS and NaOH diluted BP samples remained essentially unchanged. This can be

due to the presence of inert/hydrophobic EIM linkers in the MAF-5-Co^{II}, which can easily hinder the attack of solvent (water) or other molecules to the coordinated metal centers.

The interference study was performed by using other common sugar molecules, namely, fructose, galactose, and lactose, using MAF-5-Co^{II} NS/SPE sensor by investigating CA signal in both PBS and NaOH diluted BP samples, spiked with 2 mM glucose and 5 mM each of other compounds. **Figure 4.1.6 f** summarizes the steady-state oxidation current thus obtained, the variation in the glucose oxidation current by the presence of interfering species was of 5.6, 6.4, and 5.2%, in PBS diluted BP samples, and 3.51, 7.4, and 12.2%, in NaOH diluted BP samples, for Fructose, galactose and lactose, respectively, these results validate the good selectivity of the sensor for non-enzymatic detection of glucose in diluted blood plasma. Further selectivity tests on electroactive potential interferents, like ascorbic acid, uric acid, etc. have to be performed for a full validation.

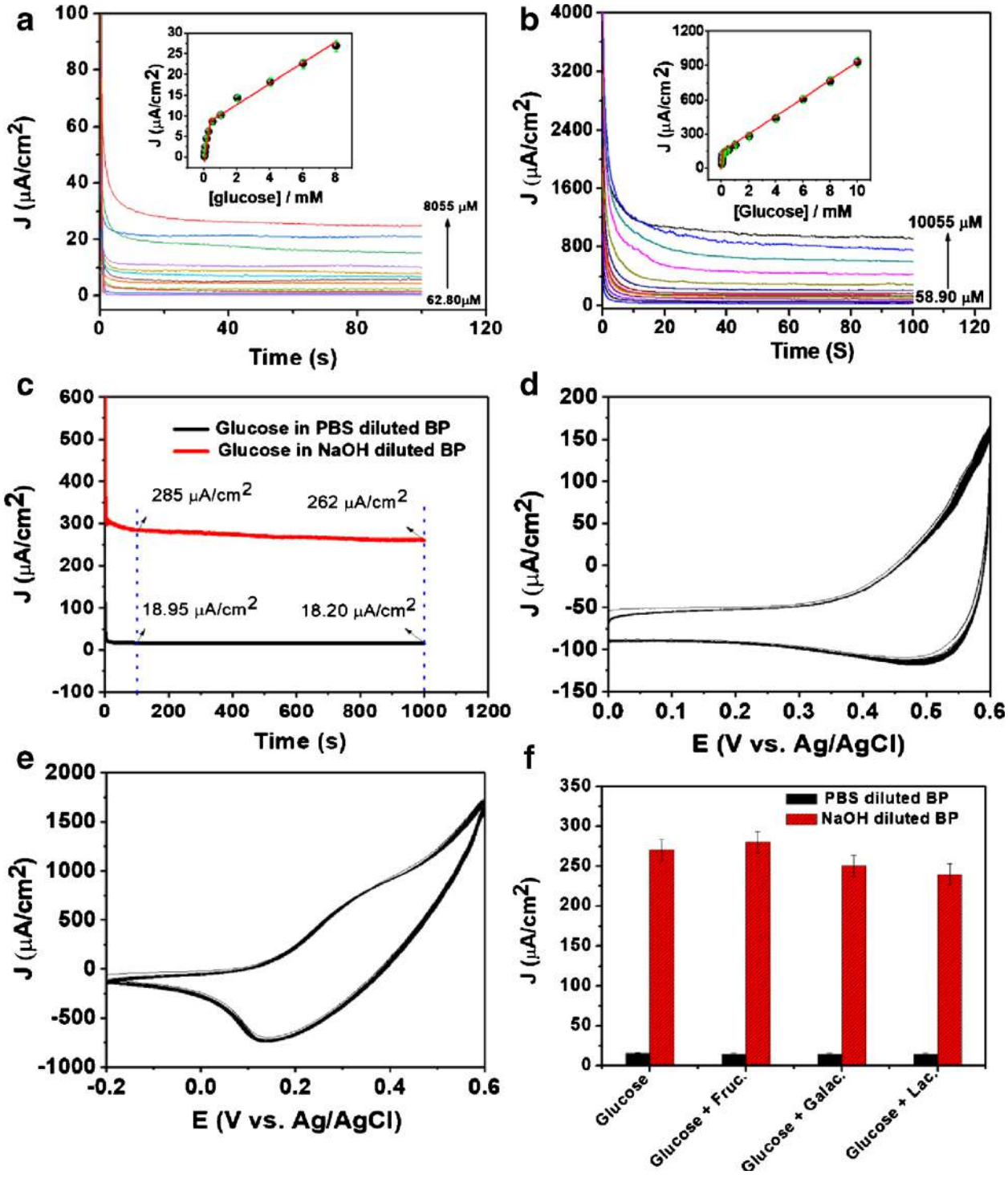

Figure 4.1.6 (a) CA responses of glucose oxidation in PBS-diluted BP samples with varying concentrations (62.80, 70.60, 86.25, 117.60, 180, 305, 555, 1055, 2055, 4055, 6055, and 8055 μM, respectively) at the MAF-5-CoII NS/SPE sensor at an applied potential of 0.45 V (inset shows the plot of current density vs. [glucose]). **(b)** CA responses of glucose oxidation in NaOH-diluted BP samples solution with varying concentrations (58.90, 70.60, 86.25, 117.6, 180, 305, 555, 1055, 2055, 4055, 6055, 8055, and 10,055 μM, respectively) at the MAF-5-CoII NS/SPE sensor at an

applied potential of 0.35 V (inset shows the plot of current density vs. [glucose]). **(c)** CA responses of PBS and NaOH solution–diluted BP samples with the spiked glucose concentration of 2 mM for 1000s. Consecutive CV sweeping (100 cycles) of the MAF-5-CoII NS/SPE sensor in glucose (2 mM) spiked **(d)** PBS and **(e)** NaOH-diluted BP samples at a scan rate of 100 mV/s. **(f)** Bar diagram of the glucose (2 mM) oxidation current responses in the absence and presence of different interferences (copy right Adeel et al.2021).

Section 4.2 Electrochemical measurements of 2D $Co(OH)_2$ NS for glucose oxidation

The graphical illustration of the work is shown in Figure 4.2

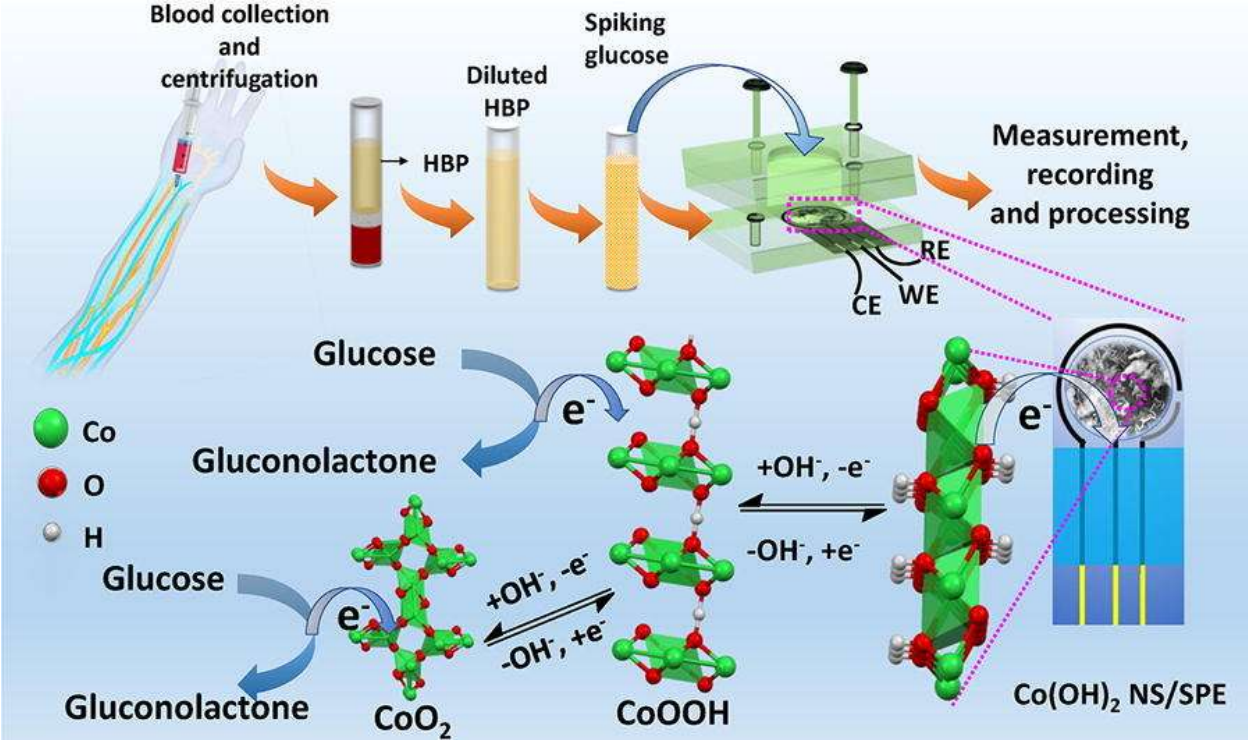

Figure 4.2: Schematic Illustration of 2D $Co(OH)_2$ NS based Glucose Sensor (copy right Adeel et al.2021).

4.2.1 $Co(OH)_2$ NS Synthesis and morphological characterizations

The procedure for the synthesis of $Co(OH)_2$ is schematically shown in **Figure 4.2.1 a**. The basic EIM and TEA molecules are hydrolysed by water and form hydroxyl (OH^-) ions. Upon addition

of $Co(CH_3CO_2)_2$, OH^- ions react with the Co^{2+} and form $Co(OH)_2$ (Eqs. 1-3). During stirring, the water-immiscible nature and low specific gravity of benzene in the water-benzene solvent can induce an outward pushing force, enabling the formation of NS. In addition to the production of $Co(OH)_2$ NS, both EIM and TEA can be etching the NS to form mesopores by coordinating with Co^{2+}.

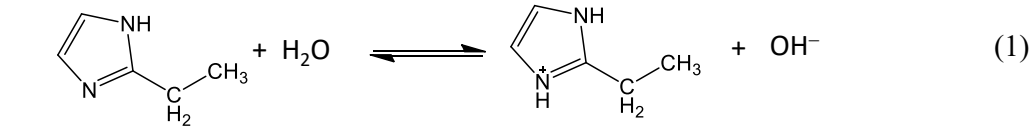

(1)

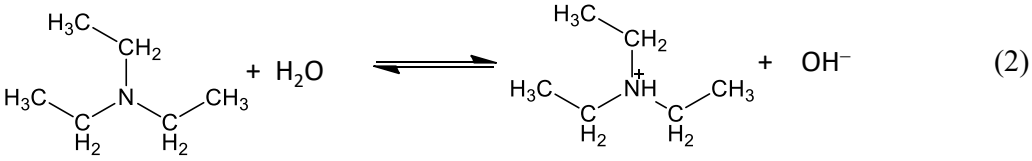

(2)

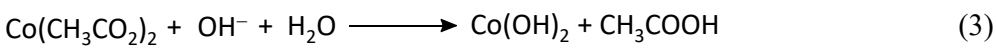

(3)

The **Figure 4.2.1b** indicated the FE-SEM results of the as-prepared $Co(OH)_2$, which shows the formation of interconnected and porous 2D-NS. The thickness of the NS was measured in the range between ca. 80-120 nm. The HR-TEM results **(Figure 4.2.1c)** also presented the formation of NS, which corresponds to the FE-SEM image. The SAED pattern of the $Co(OH)_2$ NS demonstrated bright spots with bright rings pattern (**Figure 4.2.1d**) with the *d*-spacing of 2.35, 1.45, 1.26, and 0.99 Å, which can be assigned to the *hkl* reflections of (001), (100), (011), and $(10\overline{2})$, respectively. This result suggests the good crystallinity of as synthesized $Co(OH)_2$. The measured lattice spacing of (001) plane was 2.37 Å between the adjacent fringes of the $Co(OH)_2$

NS crystal (**Figure 4.2.1e**), which is close to the measured *d* spacing value from the SAED results[7].

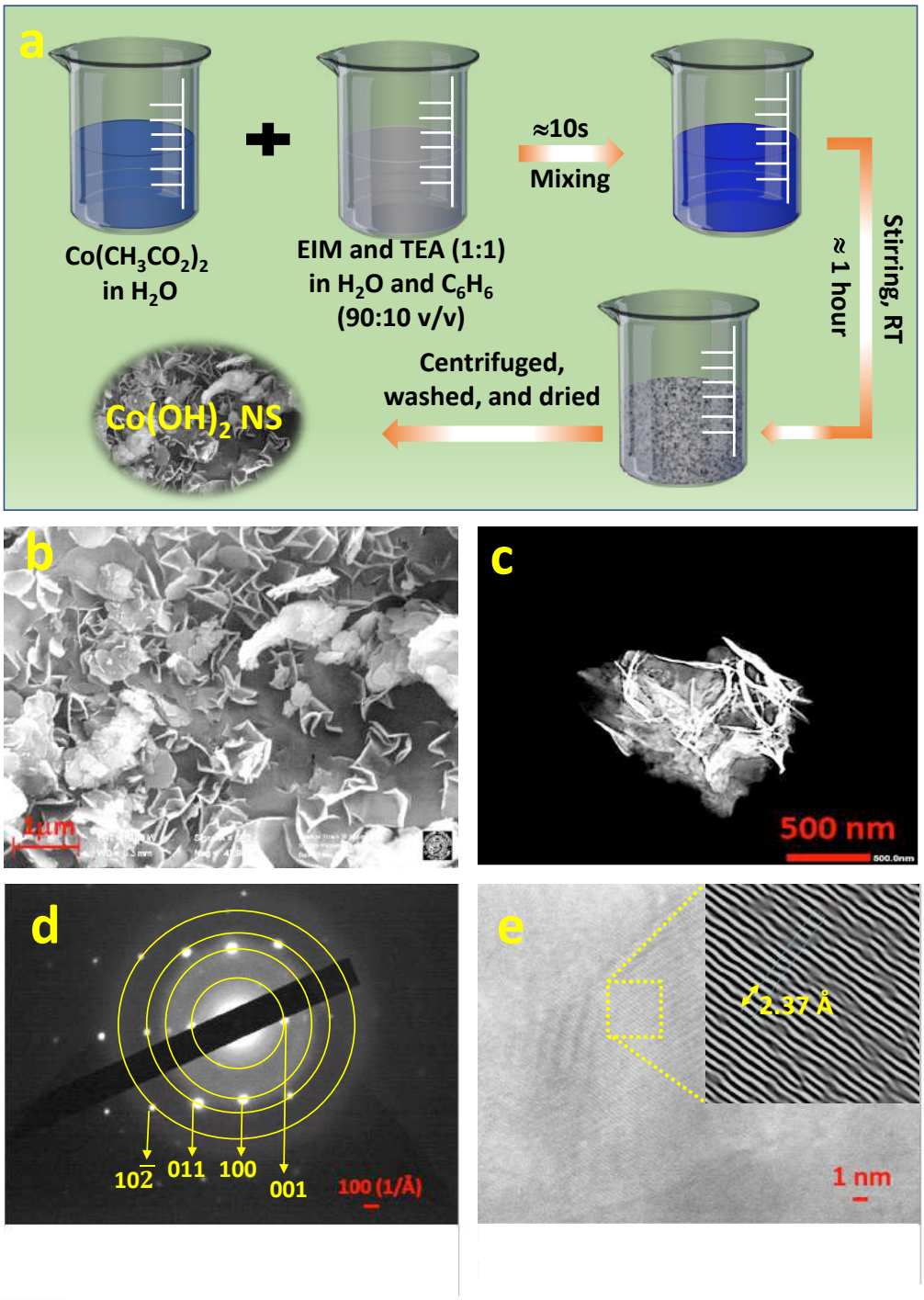

Figure 4.2.1 (a) Scheme of the synthesis of $Co(OH)_2$. (b) FE-SEM and (c) HR-TEM images, and (d) SAED pattern of the as-synthesized $Co(OH)_2$. (e) Lattice spacing (Inset shows the magnified calibrated lattice fringes) of $Co(OH)_2$ for (001) plane (copy right Adeel et al.2021).

4.2.2 XRD, BET, TGA, and spectroscopic characterizations

Figure 4.2.2 a presents the XRD results of the as-synthesized $Co(OH)_2$ NS together with the simulated XRD pattern. The crystallographic pattern of the $Co(OH)_2$ NS matches perfectly with the simulated results. The sharp and high intense peaks with no impurity peak confirm the formation of highly crystalline and pure $Co(OH)_2$. The major intense XRD peaks of $Co(OH)_2$ NS at 2θ angle values of 19.30, 32.60, 38.10, 51.35, 57.98, and 61.75° can be assigned to the *hkl* reflections of (001), (100), (011), $(10\bar{2})$, (110), and $(11\bar{1})$, respectively[8]. The characteristics of the chemical bonding in the $Co(OH)_2$ NS were investigated using FTIR and a typical spectrum is shown in **Figure 4.2.2 b**. It showes a strong absorption band due to the O-H stretching at ca. 3435 cm^{-1}, arising from the Co-OH groups and the adsorbed water molecules[9]. The weak absorption band at ca. 1090 and 1630 cm^{-1} can be attributed to the C-O stretching and C-H bending, respectively, originating from the adsorbed or intercalated CH_3COO^- ions into the $Co(OH)_2$ NS. A low intense peak at ca. 650 cm^{-1} relates the Co-OH bending vibration and the peak at ca. 650 cm^{-1} can be ascribed to the Co-O bending vibration, as similarly observed for $Ni(OH)_2$, and $Co(OH)_2$, and $Ni(OH)_2$-$Co(OH)_2$ layered double hydroxide in the literature[8–10]. **Figure 4.2.2 c** shows the N_2 adsorption and desorption isotherms, which provided a SA_{BET} value for the $Co(OH)_2$ NS equal to 97.15 m^2/g. The SA_{BET} value for the $Co(OH)_2$ NS is very high as compared to reported results in the literature for $Co(OH)_2$ and cobalt oxides (i.e., 39 - 26 m^2/g), synthesized by different synthetic methods[11,12]. The higher SA_{BET} value of the $Co(OH)_2$ NS indicates higher number of electrocatalytic active sites. **Figure 4.2.2 d** represent the TGA plot of $Co(OH)_2$ NS, which indicated two-step weight loss. The weight loss of ca. 4% in the first-step up to 170 °C can be assign to the removal of chemisorbed water and unreacted species; the sharp weight loss (ca. 11%) from 170 °C to 350 °C can be attributed to the decomposition of $Co(OH)_2$ NS. This implies that

$Co(OH)_2$ NS is very suitable for the development of sensors with good thermal stability, over the typical temperatures ranges in which the glucose levels are detected.

The XPS spectroscopy was used to analyse the elemental composition and the oxidation state of Co in the Co(OH)2 NS. The XPS survey spectrum of Co(OH)2 NS, which reveals the presence of all the characteristic elemental peaks of Co and O with an additional impurity peak of C element. This C peak possibly arises from the contamination, as similarly observed in the EDS spectrum. **Figure 4.2.2 e** shows the core-level XPS spectra of Co 2p. The high-resolution spectra of Co 2p exhibited two-spin orbit doublets for Co 2p3/2 and Co 2p1/2 together with their corresponding strong satellite peaks at the binding energies of 784.24 and 801.10 eV, respectively. The appearance of these two satellite peaks with the binding energy separation of 15.75 eV, suggesting the + 2 oxidation state of Co in the Co(OH)2 NS[10]. To deduce the additional insight, the curve was fitted by Gaussian-Lorentz functions, which showed two fitted peaks for Co 2p3/2 at the binding energy of 780.60 and 779.80 eV. The former can be ascribed to the Co2+, while the latter can be assigned to Co^{3+} [28]. The presence of Co^{3+} in $Co(OH)_2$ NS can be attributed to the unavoidable oxidation of Co2+ to Co3+ during the synthesis. However, the ratio of Co^{2+}/Co^{3+} is substantially higher, suggesting the generation of Ov on the surface of $Co(OH)_2$ NS . This was further analysed by the core-level XPS spectra of O 1s (**Figure 4.2.2 f**) which revealed two fitted peaks with different types of surface oxygen species [28]. The peak at lower binding energy (531.12 eV) can be assigned to the surface lattice oxygen (Olatt.), while the peak at higher binding energy (533.55 eV) can be attributed to the surface oxygen ion with low coordination, indicating the existence of Ov. The ratio of the Olatt./Ov is substantially higher, which is well agreed with the ratio of the Co^{2+}/Co^{3+}[28]. Note that the concentration of Ov reflects the $Co(OH)_2$ NS surface only, while the relative concentration of Ov in bulk is believed to be considerably smaller[8].

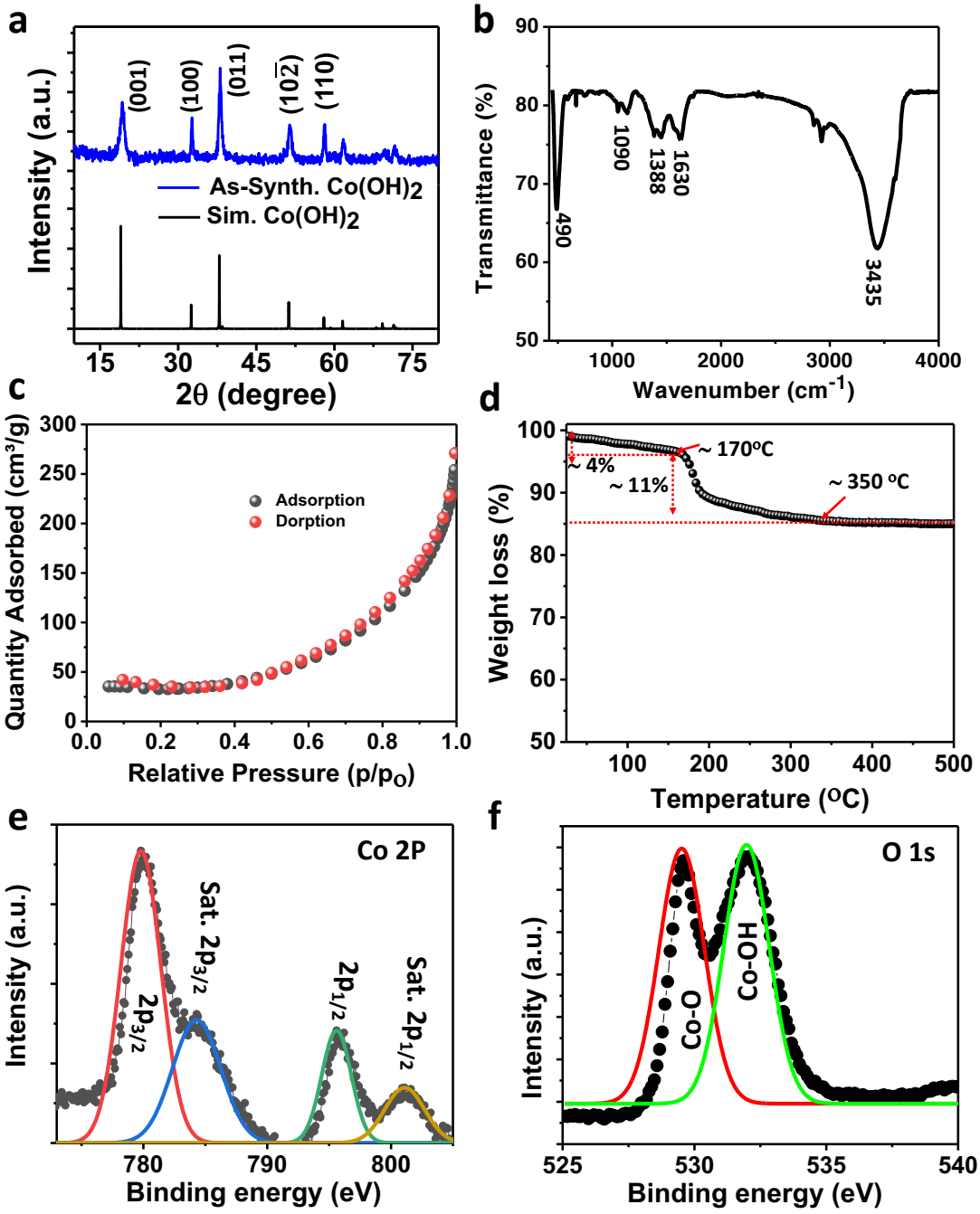

Figure 4.2.2: (a) XRD patterns of as-prepared $Co(OH)_2$ NS together with simulate pattern. (b) FTIR spectrum, (c) N_2 adsorption isotherm, and (d) TGA plot of $Co(OH)_2$ NS. Core-level XPS spectra of (e) Co 2p and (f) O 1s in $Co(OH)_2$ NS (copy right Adeel et al.2021).

4.2.3 Electrochemical characterization of $Co(OH)_2$ NS/SPE glucose sensor

Figure 4.2.3a shows the schematic demonstrations of the fabrication of $Co(OH)_2$ NS/SPE sensor. **Figure 4.2.3b** presents the CVs of SPE and $Co(OH)_2$ NS/SPE in PBS without and with (12 mM glucose). As is evident, the bare SPE does not display any redox process due to oxidation of glucose, as the background current recorded in PBS remains unaffected upon the addition of glucose, consistently with previous reports[13]. However, $Co(OH)_2$ NS/SPE shows a well-defined oxidation/reduction behavior in the potential range between 0.0 to 0.4 V due to the quasi-reversible redox process of $Co(OH)_2$ to CoOOH. It must be noted that at potential positive to 0.4 V the current increases slightly, probably due to the oxidation of CoOOH to CoO_2, as similarly explained in literature, though performed in alkaline media[14]. While, upon the addition of glucose in PBS, a general current increase is recorded, due to the oxidation of glucose to gluconolactone, assisted by both CoOOH and CoO_2, thus indicating the good catalytic activity of $Co(OH)_2$ NS for glucose oxidation. The peak current for glucose oxidation at the $Co(OH)_2$ NS/SPE increased by increasing the scan rate (**Figure 4.2.3 c**), the analysis of the anodic peak current density as a function the square root of the scan rate was linear (**inset of Figure 4.2.3 c**), providing the linear regression equation of $J\ (\mu A/cm^2) = 79.70 \pm 0.9 \times \nu^{1/2}\ (mV/s)^{1/2} - 265.60 \pm 9.10$ with the correlation coefficient (R^2) of 0.998. This result recommended the occurrence of a diffusion-controlled oxidation process involving glucose at the $Co(OH)_2$ NS/SPE sensor[2].

Figure 4.2.3 d indicates the CVs results with the bare SPE and the $Co(OH)_2$ NS/SPE sensor in NaOH solution without and with 12 mM glucose. Again, in the same potential window, the bare SPE does not show any redox behavior either in the absence or in the presence of glucose. However, the CV measured with $Co(OH)_2$ NS/SPE shows a general redox activity similar as in PBS. Particularly, the CV of $Co(OH)_2$ NS/SPE, without any glucose, displays, in the potential

range between 0.0 and 0.35 V, the pattern due to the $Co(OH)_2$/CoOOH redox pair. However, in this case, at potential positive to 0.35 V, the current increases abruptly, due to the oxidation of CoOOH to CoO_2. On the addition of glucose, a general increase of the oxidation current about 0.3 V occurs. It is likely that CoOOH and CoO_2 both act as oxidants towards glucose to produce gluconolactone.

The oxidation peak current (at 0.35 V) for glucose oxidation increased by increasing the scan rate (**Figure 4.2.3 e**); the analysis of the anodic peak current density was directly proportional to the square root of the scan rate (inset of Figure 5.2.3e) with the linear regression equation of J ($\mu A/cm^2$) = $19.0\pm0.14 \times \nu^{1/2}$ $(mV/s)^{1/2} - 59.70\pm1.35$ ($R^2 = 0.999$), demonstrating the occurrence of a diffusion-controlled oxidation phenomena[2,3]. Based on the above results and discussion, the possible reaction process for the oxidation of glucose in both PBS and NaOH is illustrated in **Figure 4.2.3 f**. The overall reaction for glucose oxidation at the $Co(OH)_2$ NS/SPE sensor can be explained as follows:

$$Co(OH)_2 + OH^- \leftrightarrow CoOOH + H_2O + e^- \quad (4)$$

$$CoOOH + OH^- \leftrightarrow CoO_2 + H_2O + e^- \quad (5)$$

$$CoOOH + glucose \rightarrow Co(OH)_2 + gluconolactone \quad (6)$$

$$2CoO_2 + glucose \rightarrow 2CoOOH + gluconolactone \quad (7)$$

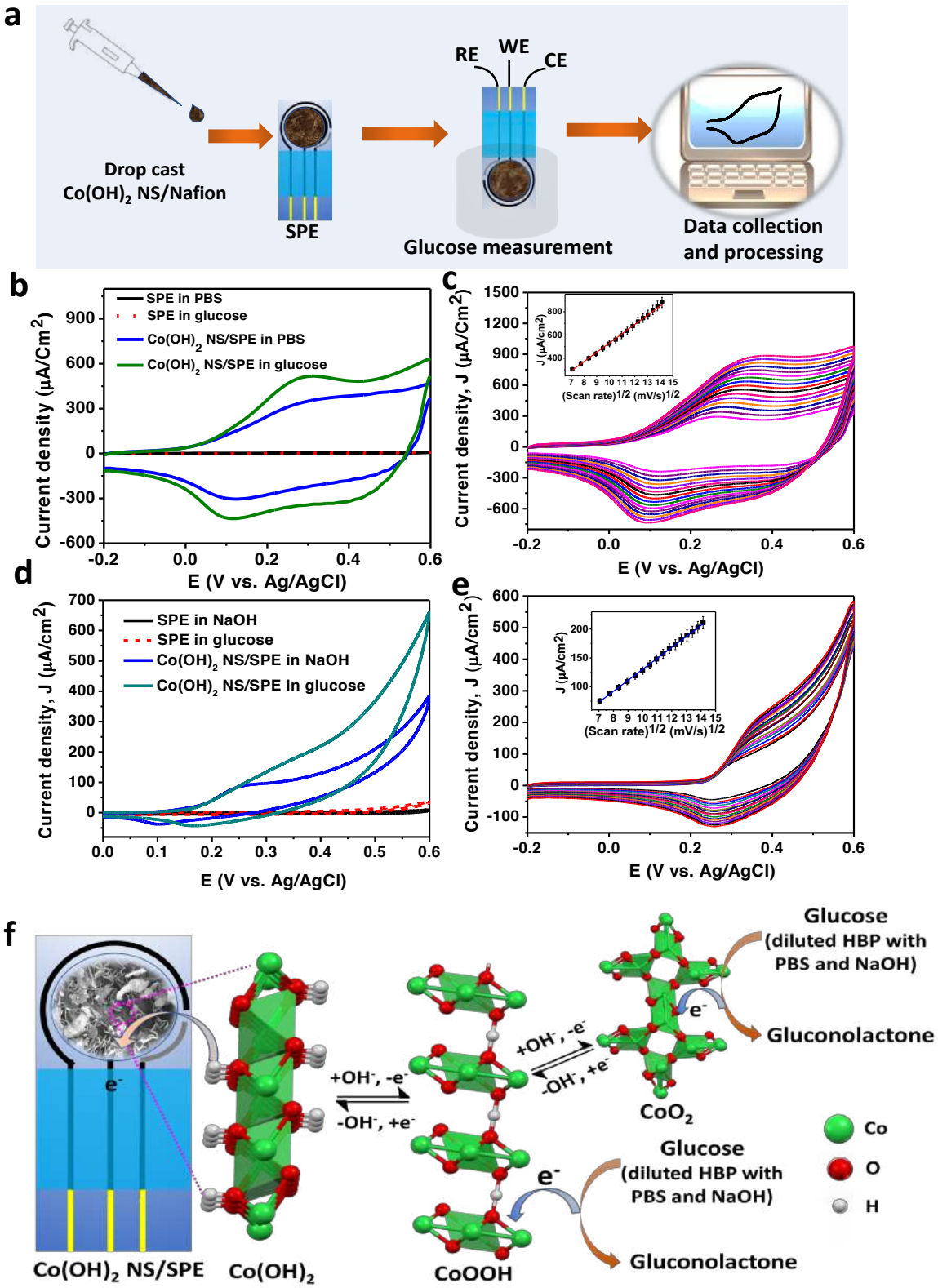

Figure 4.2.3: (a) Schematic illustration of the fabrication of $Co(OH)_2$ NS/SPE sensor and glucose detection. (b) CVs of SPE and $Co(OH)_2$ NS/SPE sensor in PBS with and without glucose at a scan

rate of 100 mV/s. (c) CVs of glucose in PBS at the $Co(OH)_2$ NS/SPE sensor with varying scan rates from 50-200 mV/s (inset shows the plot of anodic peak current density *vs.* root over scan rate). (d) CVs of SPE and $Co(OH)_2$ NS/SPE sensor in NaOH solution with and without glucose at a scan rate of 100 mV/s. (e) CVs of glucose in NaOH solution at the with and without sensor at different scan rates from 50-200 mV/s (inset shows the plot of anodic peak current density *vs.* root over scan rate). (f) A possible mechanism for the electrochemical oxidation of glucose at the sensor in both PBS and NaOH solutions (copy right Adeel et al.2021).

4.2.4 Detection of glucose in PBS and NaOH

For the glucose detection, chronoamperometry (CA) was employed. To optimize the applied potential, series of potential steps were performed at various potentials in the range from 0.25 to 0.55 V in PBS and 0.35 to 0.55 V in NaOH solutions. The steady-state oxidation current of glucose of concentration12 mM in both PBS and NaOH solutions increased with the increase of the applied potential (**insets of Figure 4.2.4 a and b**, respectively) correspondingly with the results acquired by CV. However, when higher potential is applied, the selectivity of the sensor could be disturbed, due to the oxidations of interferents present in the matrix under investigation[3]. Therefore, to achieve enough sensitivity while minimizing interference effects, hereafter, 0.45 and 0.35 V were chosen for the detection of glucose in PBS and NaOH solution, respectively.

Figures 4.2.4 a and b display the CA results obtained at the $Co(OH)_2$ NS/SPE sensor by varying the glucose concentrations in PBS and NaOH solution, respectively. The steady-state oxidation current in both solutions increased linearly by increasing the glucose concentrations in two concentration ranges (**insets of Figures 4.2.4 a and b**). This behavior is similar to that obtained in other porous materials in the literature[2,3]. This mechanism has been explained in the following, at low concentrations, glucose spread within the sensor surface is instantly oxidized by many active sites available on the surface of sensor ($Co(OH)_2$ NS), providing current responses characterized by high sensitivity[3]. On the other hand, at higher glucose values, the consistently higher oxidation product (i.e., gluconolactone) can act as a barrier for glucose diffusion, which

precedes to current responses of lower sensitivity[3]. The analytical performance of the proposed sensor is summarized in **Table 4.2.1**. These results imply that the analytical performance (e.g., sensitivity, LOD) of this sensor is much higher in physiological conditions than alkaline medium, which agrees with the CV results (**Figures 4.2.3 b and d**). Thus, $Co(OH)_2$ NS is a potential electrode modifier for the detection of glucose in physiological pH and an alkaline medium.

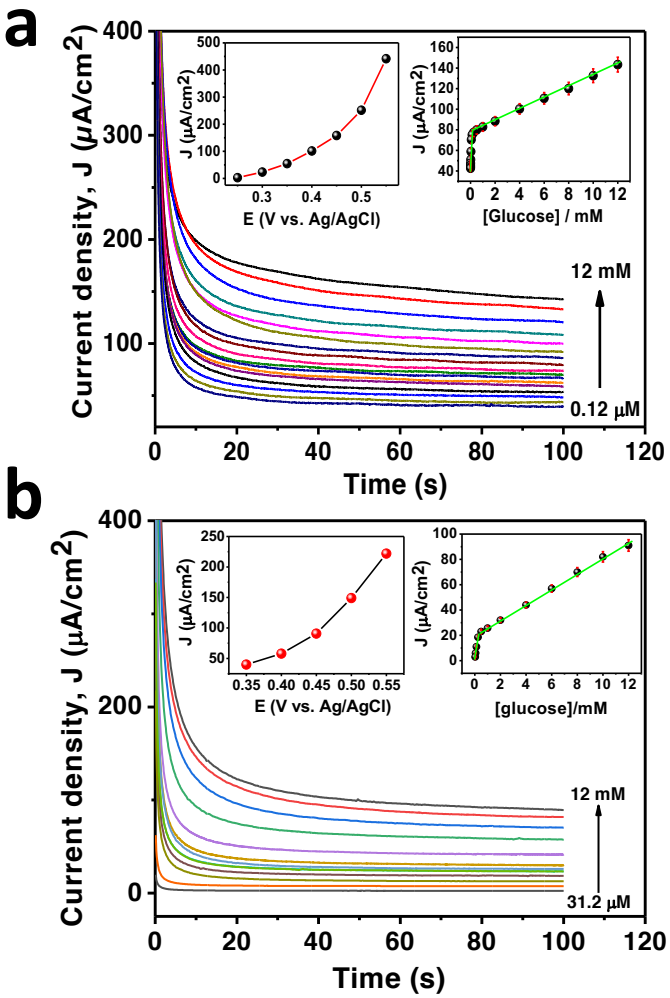

Figure 4.2.4: (a) CA responses of glucose oxidation in PBS with varying concentrations from 0.12 μM to 12 mM (0.12, 1.95, 3.9, 7.8, 15.6, 31.25, 62.6, 125, 250, 500, 1000, 2000, 4000, 6000, 8000, 10000, and 12000 μM, respectively) (inset displays the plots of *J vs.* applied potential, and *J vs.* [glucose]). (b) CA responses of glucose oxidation in NaOH solution with varying concentrations from 7.80 μM to 10 mM (31.2, 62.6, 125, 250, 500, 1000, 2000, 4000, 6000, 8000, 10000, and 12000 μM, respectively) (inset displays the plots of *J vs.* applied potential, and *J vs.* [glucose]). (Copy right Adeel et al.2021).

Medium	Dynamic Range	Linear regression equation (R^2)	LOD (μM)
PBS	125 μM -12 mM	J (μA/cm^2) = 5.60±0.08 × C_{Glu}/mM + 76.51±0.5 (R^2 = 0.998)	0.08
	0.12 - 62.5 μM	J (μA/cm^2) = 443.36±17.50 × C_{Glu}/mM + 43.50±0.47 (R^2 = 0.990)	-
PBS/Diluted HBP	125 μM -12 mM	J (μA/cm^2) = 8.0±0.27 × C_{Glu}/mM + 60.50±1.65 (R^2 = 0.990)	0.082
	0.12 - 62.5 μM	J (μA/cm^2) = 430±14.95 × C_{Glu}/mM + 16.40±0.40 (R^2 = 0.992)	-
NaOH	500 μM - 12 mM,	J (μA/cm^2) = 6.10 ± 0.10 × C_{Glu}/mM + 20.0±0.70 (R^2 = 0.998)	2.5
	31.2 - 250 μM	J (μA/cm^2) = 77.74±7.10 × C_{Glu}/mM + 0.60±0.40 (R^2 = 0.975)	-
NaOH/Diluted HBP	250 μM - 12 mM	J (μA/cm^2) = 6.13±0.22 × C_{Glu}/mM + 30.70±0.80 (R^2 = 0.989)	2.2
	7.8 - 125 μM	J (μA/cm^2) = 98.18±8.12 × C_{Glu}/mM + 11.25±0.37 (R^2 = 0.980)	-

Table 4.2.1: Analytical performance of the sensor under various experimental conditions. C_{Glu} is the concentration of glucose (Copy right Adeel et al.2021).

4.2.5 Detection of glucose in diluted human blood plasma samples

Several CA measurements were performed by using diluted HBP samples. They were spiked with glucose in the range 0.12 μM - 12 mM and 7.8 μM - 12 mM in PBS and NaOH diluted HBP, respectively. The subsequent CA plots are presented in **Figures 4.2.5 a and b**, respectively. Like the PBS and NaOH solutions, the steady-state oxidation current increased with increasing the concentrations of glucose and represents linear responses in two concentration ranges (**insets of Figures 4.2.5 a and b,** respectively). The analytical performance of purposed sensor (summarized in **Table 4.2.1)** is comparable or higher than the other reported MOHs-nanomaterials-based non-enzymatic glucose sensor systems[3]. This result shows that $Co(OH)_2$ NS is highly appropriate for self-monitoring and point-of-care detection of glucose in biological fluids.

4.2.6 Stability, Reproducibility, repeatability, and Interference studies

Figure 4.2.5 c shows the CA results measured in PBS and NaOH diluted HBP samples, spiked with 12 mM of glucose. As is evident, the current decreased only by 4.20 and 13.0% (after 1000s), and by 10.67 and 15.0% (after 36000s), in PBS and NaOH diluted HBP samples, respectively, implying, in general, an excellent long-term stability of the purposed sensor.

The influence of the interfering compounds like fructose (Fruc.), galactose (Galac.), and lactose (Lac.), two times higher (20 mM) in concentration than the glucose (10 mM) concentration, was also estimated. **Figure 4.2.5 d** shows the bar diagram of the summary of oxidation current of glucose at the $Co(OH)_2$ NS/SPE sensor in the absence/presence of interfering compounds in both PBS and NaOH diluted HBP samples. The deviation of *J* for glucose oxidation in the presence of Fruc., Galac., and Lac., was of 2.70, 2.40, and 8.2%, respectively, in PBS diluted HBP samples, while it was 2.60, 6.5, and 4.10%, respectively, in NaOH diluted HBP samples, suggesting the excellent selectivity of the sensor for non-enzymatic detection of glucose in diluted human blood plasma. Further selectivity tests on electroactive potential interferents, like ascorbic acid, uric acid, etc. should to be performed for a full validation. This aspect will be considered in further investigations.

The reproducibility of the purposed sensor was examined using eight independent sensors (fabricated independently). The relative standard deviation (RSD) in the oxidation current in 10 mM of glucose in PBS and NaOH diluted HBP samples was 1.22 and 4.50%, respectively. The sensors also exhibited tremendous repeatability, which was studied after storing the sensor in ambient atmospheric conditions for five days. The CA profiles for glucose in PBS and NaOH diluted HBP samples were assessed in every 24 hours' interval, showing a very low RSD of 2.10% and 5.15%, respectively. This specifies the suitability of $Co(OH)_2$ NS for glucose monitoring in

physiological pH and alkaline media with very high stability, excellent reproducibility, and tremendous repeatability.

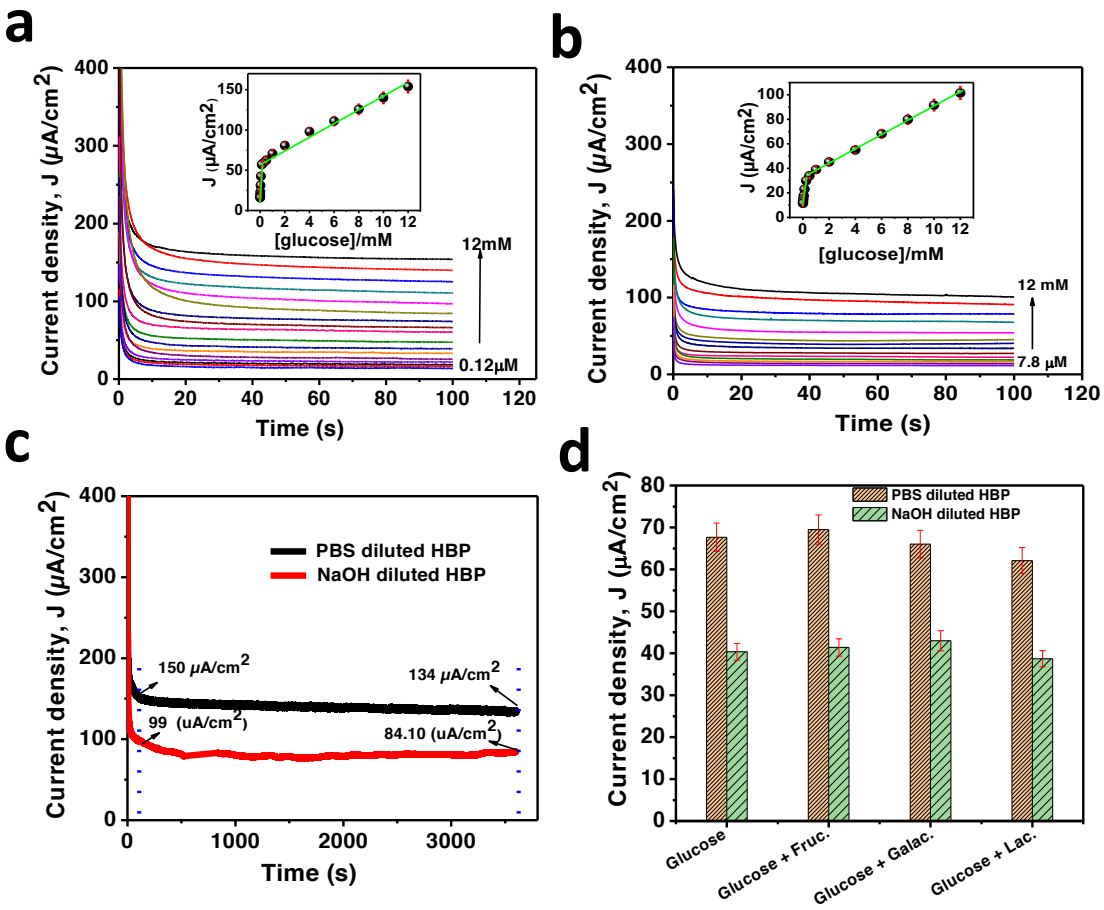

Figure 4.2.5: (a) CA responses of glucose oxidation in PBS diluted HBP samples with varying concentrations from 0.12 µM to 12 mM (0.12, 1.95, 3.9, 7.8, 15.6, 31.25, 62.6, 125, 250, 500, 1000, 2000, 4000, 6000, 8000, 10000, and 12000 µM, respectively) (inset shows the plot of *J vs.* [glucose]). (b) CA responses of glucose oxidation in NaOH diluted HBP samples solution with varying concentrations from 7.80 µM to 12 mM (7.8, 15.6, 31.25, 62.6, 125, 250, 500, 1000, 2000, 4000, 6000, 8000, 10000, and 12000 µM, respectively) (inset shows the plot of *J vs.* [glucose]). (c) CA responses of glucose oxidation for 36000s. (d) Bar diagram of glucose oxidation currents in the absence and presence of interferences (Copy right Adeel et al.2021).

Section 4.3 Electrochemical Biosensor for the COVID-19 Detection

The graphical abstract of the work carried out in this section is shown in **Figure 4.3**

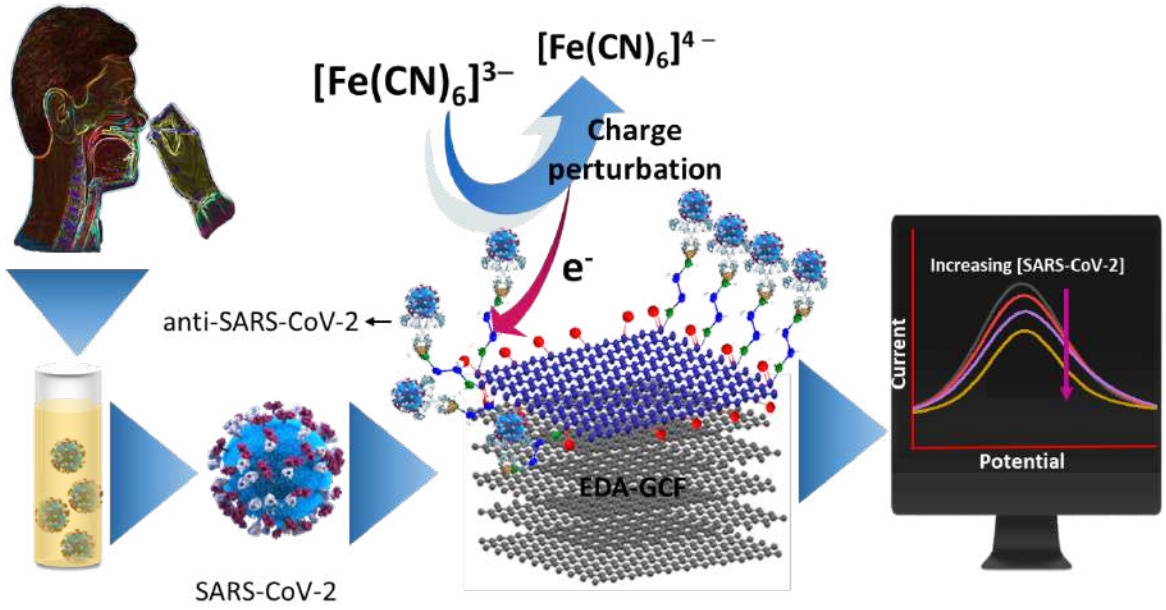

Figure 4.3: Schematic Illustration of Covid-19 immunosensor for spike protein detection (Copy right Adeel et al.in submission).

4.3.1 XRD, Raman, and FTIR characterizations

The degree of the exfoliation, oxidation, and functionalization of the GCF surface was investigated using X-ray diffraction (XRD) analyses. **Figure 4.3.1a** shows the XRD patterns of the GCF, OGCF, and EDA-GCF. The GCF exhibited a high intensity typical sharp (002) peak of graphite at a 2θ angle of 26.10° with the interlayer spacing (d_{002}) of 3.41 Å [15,16]. Upon the oxidation of the GCF, a new low-intensity peak appeared at 2θ = 20.40°, attributed to the partial and fractional oxidation of the GCF surface only down to few layers. The intercalation of oxygen atoms throughout the interlayer space, or in between the basal planes of the GCF, was excluded by the absence of the graphene oxide (GO) peak at about 10°, as instead was the case when GO was synthesized from graphite [16,17]. The above mentioned peak shifted to a higher 2θ angle (22.85°) in EDA-GCF can be ascribed to the EDA attachment to the –COOH moieties as well as to the partial reduction of the surface oxygen functional groups of OGCF induced by the EDA reducing

agent[17,18]. The new low-intensity peak appeared at 2θ =11.35° in EDA-GCF is possibly due to the intercalation of EDA throughout the interlayer space or in between the basal planes of GCF, as similarly observed for the intercalation of oxygen functionalities in between the basal planes of GO, prepared from graphite[16,17]. Furthermore, the high intense (002) peak was shifted to 26.45° for the EDA-GCF (**Figure 4.3.1b**), suggesting the decrease of the interlayer spacing (d_{002} = 3.36 Å)[19]. This can be ascribed to the stitching of the GCF and OGCF layers by the EDA, induced by the covalent interaction and hydrogen bonding with the oxygen functional groups in GCF and OGCF at the edges and basal planes[20]. The full width at half maximum (FWHM) of the (002) plane for GCF was 0.39°, and was increased to 0.52° for EDA–GCF, indicating the reduction of the crystalline size of EDA-GCF (**Figure 4.3.1b**)[19].

The compositions and the crystal structures of the GCF, OGCF, and EDA-GCF were examined further by Raman spectroscopy, and the resulting spectra are shown in **Figure 4.3.1c**. All the samples display the characteristics G band (1590 cm^{-1}), 2D band (2715 cm^{-1}), and D (1350cm^{-1}) band without any noticeable shifting of the peak positions [21]. However, both GCF and OGCF exhibit an additional D′ band (1615 cm^{-1}), indicating the disordered structure due to the presence of oxygen functional groups in their structure[21,22]. The intensity of this D′ band in OGCF is higher than that of GCF, suggesting the formation of a highly disordered structure induced by the oxidation. These disordered structures or defects decreased after the EDA functionalization and the partial reduction of OGCF. Additionally, both OGCF and EDA-GCF exhibit the 2D peak with two peak profiles ($2D_1$ and $2D_2$), indicating the formation of perfectly A-B stacked few layers GO like OGCF and EDA-GCF. In contrast, GCF shows a single peak profile with multilayer structures, which is consistent with the general characteristics of graphite[22]. However, the intensity of the 2D peak in OGCF is decreased compared to the GCF due to the presence of defects and functional

groups, which were increased in EDA-GCF, suggesting the reduction of the defects by EDA functionalization and partial reduction of oxygen functionalities, consistent with the intensity profiles of D bands of the samples[21].

Figure 4.3.1d shows the FTIR spectra of the samples. All the samples exhibited the common FTIR band of O–H stretching vibrations at 3534 cm^{-1}, due to the presence of adsorbed water molecules, the C=C stretching vibrations (1630 cm^{-1}), $-CH_2$ stretching bands (2930 and 2845 cm^{-1}), and the C–O bands (1060 cm^{-1})[17,20]. The OGCF displays the additional C=O stretching band of the COOH groups at 1708 cm^{-1} and C–OH vibrations at 1170 cm^{-1}. The EDA-GCF shows the additional strong N−H stretching (wide) and bending vibrations at 3090 and 1580 cm^{-1}, respectively, and C–N vibrations at 1320 cm^{-1} together with the C=O stretching and C–OH vibrations at 1120 cm^{-1} [20]. These results further suggest the successful synthesis of OGCF and EDA-GCF. Nevertheless, the reduction of the C–O peak area and intensity in the EDA-GCF compared to the OGCF indicates the partial reduction of the OGCF induced by the EDA, which is consistent with the XRD observations.

Figures 4.3.1 (**e-g**) show the contact angles and wetting behaviour of the electrodes, measured after 10 sec when the water drop was applied on the surfaces of the electrodes. It is apparent that the surface wettability of the GCF is enhanced somewhat, upon the oxidation and EDA functionalization. The decrease of the contact angles passing from GCF (73.51°) to OGCF (41.93°) is conceivably induced by the hydrogen bonding between the water molecules and the oxygen functionalities generated by the oxidation. The further decrease of the contact angle (33.46°), upon OGCF functionalization with EDA, supports the success of the reaction and intercalation of the molecule.

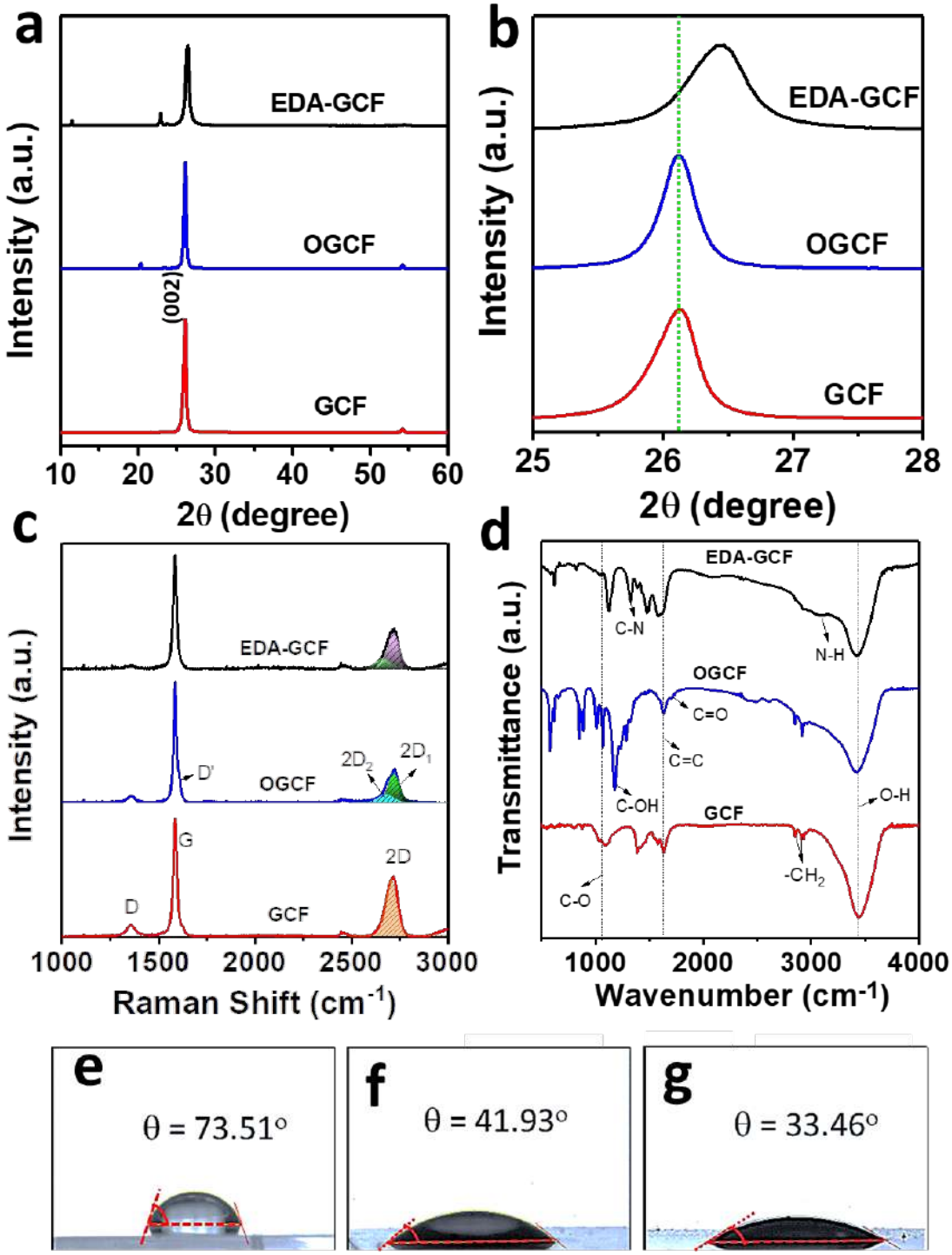

Figure 4.3.1: (a) XRD pattern, (b) magnified XRD pattern, (c) Raman spectra, and (d) FTIR spectra of GCF, OGCF, and EDA-GCF. (e-g) contact angles of GCF, OGCF, and EDA-GCF, respectively, using ultrapure water (Copy right Adeel et al.in submission).

4.3.2 Morphological characterization

Figures 4.3.2 (**a-f**) show the FE-SEM images of the GCF, OGCF, and EDA-GCF surfaces. The GCF surface exhibits small wrinkles, while that of the OGCF is covered with partially exfoliated GO nanosheets. The EDA functionalization induced the decrease in the size of the nanosheets and an increase of the EDA-GCF surface roughness, compared to that of GCF. This is also evident from the corresponding digital pictures and could also be observed by the naked eye (insets of **Figures 4.3.2** (**b-f**), respectively). The spectra show the presence of high-density oxygen functionalities in OGCF, compared to that of GCF. The EDA functionalized-electrode surface examined by EDS mapping revealed the presence of high density and homogeneous distribution of carbon, nitrogen, and oxygen (**Figures 4.3.2** (**g-i**), respectively.

The mechanism of exfoliation, oxidation, and EDA functionalization of GCF is schematically shown in **Figure 4.3.2j**. Upon the mild acid treatment, the SO_4^{2-}, NO_3^-, and H^+ ions are easily intercalated into the GCF layers. This can led to a much higher interlayer distance between the graphite sheets (0.334 nm), compared to the ionic radius (r) of the H^+ (r_{H^+} = 0.037 nm), SO_4^{2-} ($r_{SO_4^{2-}}$ = 0.258 nm), and NO_3^- ($r_{NO_3^-}$ = 0.179 nm)[19]. This enabled the expansion and oxidation of the GCF layer and the formed OGCF. The low hydrophilicity and the floating behaviour of the GCF and the absence of any forced convection (stirring, sonication, etc.) enabled controlling the partial oxidation and exfoliation of the GCF surface only in contact with the acidic solution.

The increase of the hydrophilicity of the OGCF enabled the EDA functionalization through a covalent bond between the –COOH groups of OGCF and the $–NH_2$ groups of EDA, favoured by EDC and NHS activation. The spontaneously formed oxygen functionalities (–OH and –COOH) at the edges and basal planes of GCF can also induce a chemical interaction (hydrogen bonding) with the intercalated small EDA molecules. Both these interactions can be able to stitch the GCF

sheets through basal planes and edges (**Figure 4.3.2j**), and the smaller GCF or OGCF sheets are stitched easily and decrease the size, as is evident in the FE-SEM image of EDA-GCF. Furthermore, bridging or stitching through basal planes between the adjacent GCF layers can induce the decrease in the interlayer distance in EDA-GCF, as was evident from the XRD results.

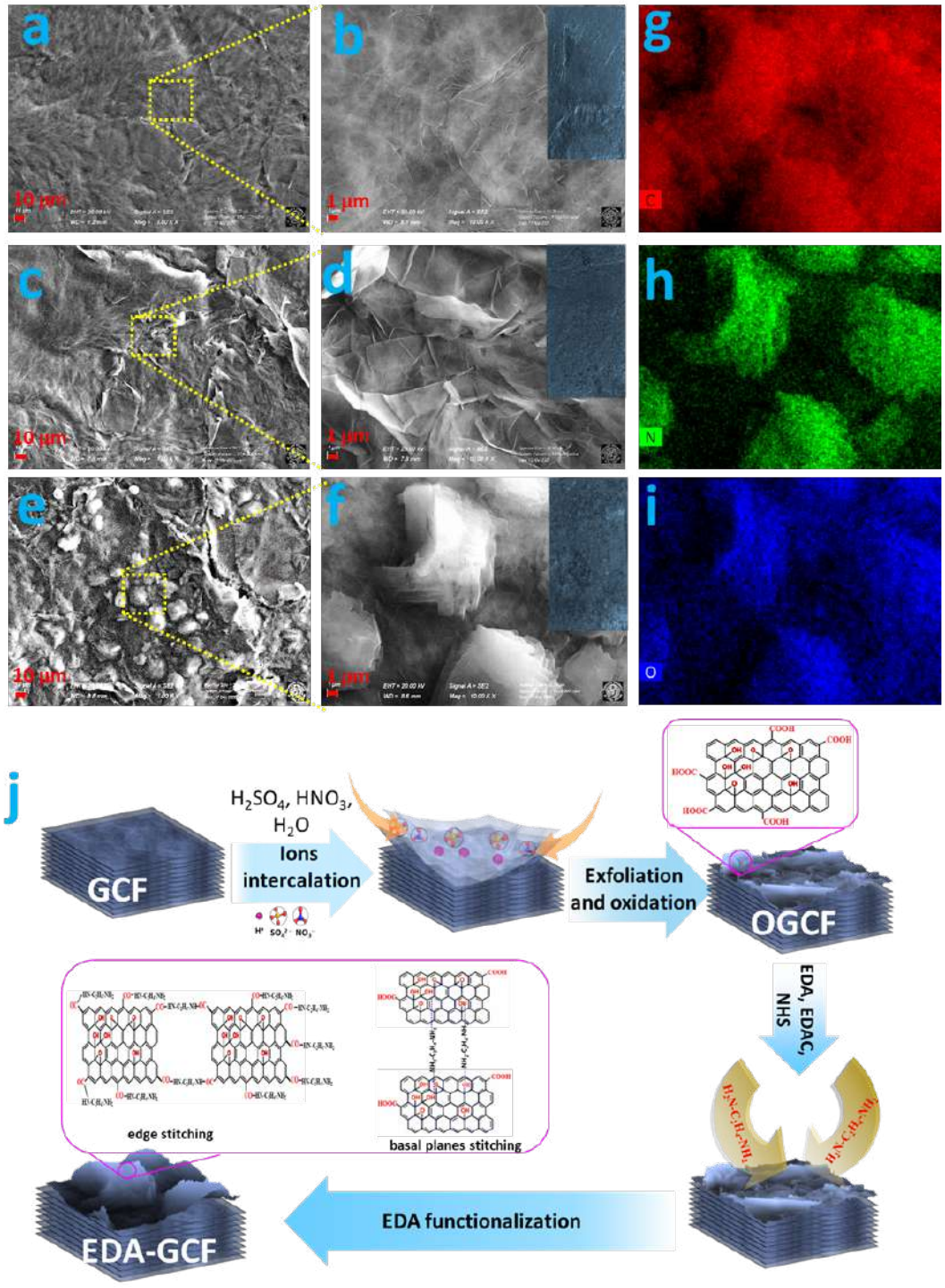

Figure 4.3.2: FE-SEM images of (a-b) GCF, (c-d) OGCF, and (e-f) EDA-GCF (insets of b, d, and f show the digital photographic images of GCF, OGCF, and EDA-GCF, respectively). (g-i) EDS mapping of C, N, and O, respectively, in EDA-GCF. (j) Schematic of the mechanism of controlled partial exfoliation and the preparation of OGCF and EDA-GCF (Copy right Adeel et al.in submission).

4.3.3 XPS Characterization

XPS was used to examine the elemental compositions and the bonding types that exist in the GCF, OGCF, and EDA-GCF. As anticipated, the XPS survey spectra of all the samples predominantly show the presence of carbon and oxygen peaks, while EDA-GCF exhibits an additional nitrogen peak arising from the EDA functionalization (**Figure 4.3.3a**). The oxidation process can effectively increase the surface oxygen content from 14.33 at% for GCF to 30.84 and 22.88 at% for OGCF and EDA-GCF, respectively. While the higher N (26.97 at%) content in EDA-GCF and the decrease of the O at% suggest the incorporation of EDA between the adjacent GCF layers, the partial reduction of OGCF, and the covalent attachment of EDA. The high-resolution XPS spectra of C 1s and N 1s were investigated to examine the types of chemical bonding and the vacancies or defects present in the samples. **Figure 4.3.3b** shows the C 1s spectra of the GCF, OGCF, and EDA-GCF. The high-resolution C 1s XPS spectra for all the samples were fit into five component peaks. The peaks positioned at 284.80 eV for all the samples can be ascribed to the delocalized C=C bonds, while the peaks located at 286.60 and 286.12 eV for GCF and OGCF, respectively, can be attributed to the localized C-C bonds with the percentage of 40.44% and 39.55%, respectively[23]. The increase of the intensity of this peak for EDA-GCF at 286.30 eV with 46.75% can be ascribed to the combination of localized C–C and C–N peaks[23,24]. Both GCF and OGCF exhibit –COOH peaks at 290.0 and 289.50 eV, respectively, with the percentage of 2.10% and 6.20%, respectively, indicating the high degree of oxidation of GCF[24]. This –COOH peak is diminished in EDA-GCF and a new peak arises at lower binding energy (288.31 eV), which corresponds to the C=O bond originating from the amide bond[25]. All the samples exhibit the additional small intensity peaks of C–OH for GCF (286.69 eV), OGCF (286.15 eV), and EDA-GCF (286.50 eV), together with the C atoms neighbouring lattice vacancies 5.28%, 8.6%, and

4.41%, respectively, for GCF, OGCF, and EDA-GCF at 284.0, 284.15, and 283.95 eV, respectively[24]. The variation of the degree of lattice vacancies is highly consistent with the Raman results. Further, we analyzed the high-resolution N 1s spectra of EDA-GCF as shown in **Figure 4.3.3c**. The spectra can be fitted into three component peaks. The high-intensity peak located at 401.75 eV can be assigned to the C–N bond, while the other low-intensity peaks located at 399.5 and 402.10 eV can be ascribed to the $–NH_2$ and N–C=O bonds[24–26], suggesting the successful EDA functionalization.

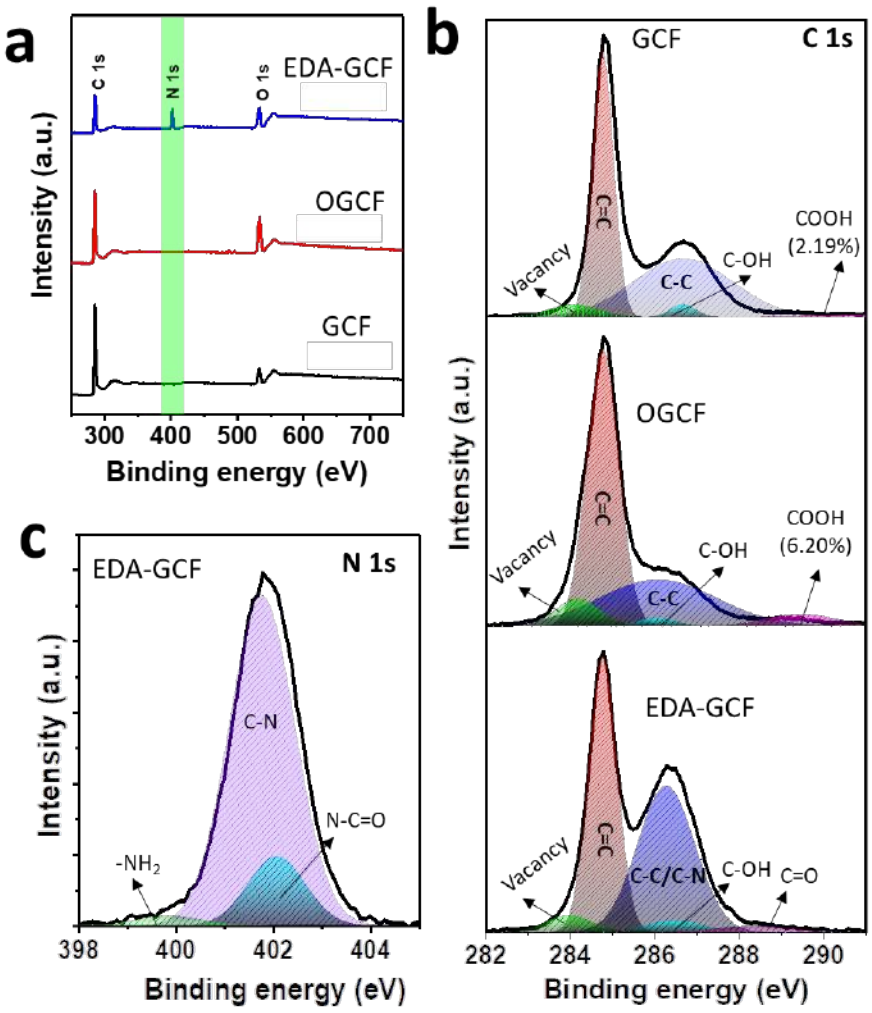

Figure 4.3.3: (a) XPS survey spectra of the GCF, OGCF, and EDA-GCF. (b) High-resolution C 1s spectra of GCF, OGCF, and EDA-GCF, and (c) N 1 s spectra of EDA-GCF. Solid lines and the shaded area indicate the experimental and fitted data, respectively (Copy right Adeel et al.in submission).

4.3.4 Electrochemical Characterization

The general electrochemical behavior of the GCF, OGCF, activated OGCF (Act. OGCF), and EDA-GCF electrodes were, preliminary, characterized by cyclic voltammetry (CV) (**Figure 4.3.4a**) and electrochemical impedance spectroscopy (EIS) (**Figure 4.3.4b**), using an aqueous solution of $[Fe(CN)_6]^{3-/4-}$ in phosphate buffer (PBS, pH 7.4). The inset of **Figure 4.3.4a** summarizes the anodic peak current density (J_{pa}) and the peak-to-peak potential separation (ΔE_p) obtained from the CVs at 100 mV/s with the various electrodes. As is evident, the CV recorded at the GCF exhibits a redox pattern having a quite large ΔE_p (180 mV) and J_{pa} of 1.44 mA/cm^2. The apparent sluggish electron transfer process can be in part due to a local electrostatic repulsion between negatively charged carboxyl ions (COO^-), formed spontaneously on the GCF surface (see above), with the negatively charged $[Fe(CN)_6]^{3-/4-}$ redox couple [27]. A more drownout CV, having a somewhat larger ΔE_p (190 mV) and a smaller J_{pa} (1.41 mA/cm^2) was recorded at the OGCF. This can be attributed to the enhanced electrostatic repulsion between the high density of COO^-, present onto the OGCF surface, with the negatively charged $[Fe(CN)_6]^{3-/4-}$ redox probe[27,28], as schematically depicted in **Figure 4.3.4c**. After the activation of the carboxylic groups, by using EDC and NHS, the Act. OGCF displayed a smaller ΔE_p (110 mV) and a higher J_{pa} (2.71 mA/cm^2). This can be ascribed to the neutralization of negatively charged COO^- in the OGCF surface by the small NHS molecules (**Figure 4.3.4c**)[29]. The incorporation of EDA into the porous material led to a small decrease of J_{pa} (2.05 mA/cm^2), while ΔE_p remained essentially constant (110 mV). The information gathered from the CVs were confirmed by EIS measurements. In fact, as is evident from **Figure 4.3.4b**, all the electrodes exhibit Nyquist type plots with the interfacial charge transfer resistance (R_{ct}) and Warburg diffusion resistance (Z_w) at the high and low-frequency region, respectively[30]. The variation of the R_{ct} for all the electrodes well agrees with the electrochemical

features obtained from CVs. In particular, R_{ct} of 852.0, 1729.50, 158.0, and 240.25 Ω were found at the GCF, OGCF, Act. OGCF, and EDA-GCF electrodes, respectively.

Figure 4.3.4d shows the CVs of the EDA-GCF electrode in $[Fe(CN)_6]^{3-/4-}$ redox solution at different scan rates. Both J_{pa} and cathodic peak current density (J_{pc}) increased with increasing scan rate and they were proportional to the square root of the scan rates (inset of **Figure 4.3.4d**). The linear regression analysis of experimental data provided the equations of J_{pa} (mA/cm^2) = 0.24 (±0.0013) × $\nu^{1/2}$ (mV/s)$^{1/2}$ – 0.22 (± 0.007; R^2 = 0.999) and J_{pc} (mA/cm^2) = -0.20 (±0.002 × $\nu^{1/2}$ (mV/s)$^{1/2}$ + 0.11 (± 0.01; R^2 = 0.999), suggesting the occurrence of a diffusion-controlled redox process[31]. Furthermore, the electrochemical stability of the EDA-GCF electrode was analyzed by repetitive CV scans (i.e., 100 cycles, **Figure 4.3.4e**) and chronoamperometric (CA) measurements for 1 h (inset of **Figure 4.3.4e**). The CVs revealed a relative standard deviation (RSD) of only 2.10% for the J_{pa}, while the quasi steady-state current density value in the CA was almost stable for 1h, indicating the high stability of the EDA-GCF electrode and promising for the development of stable electrochemical sensors.

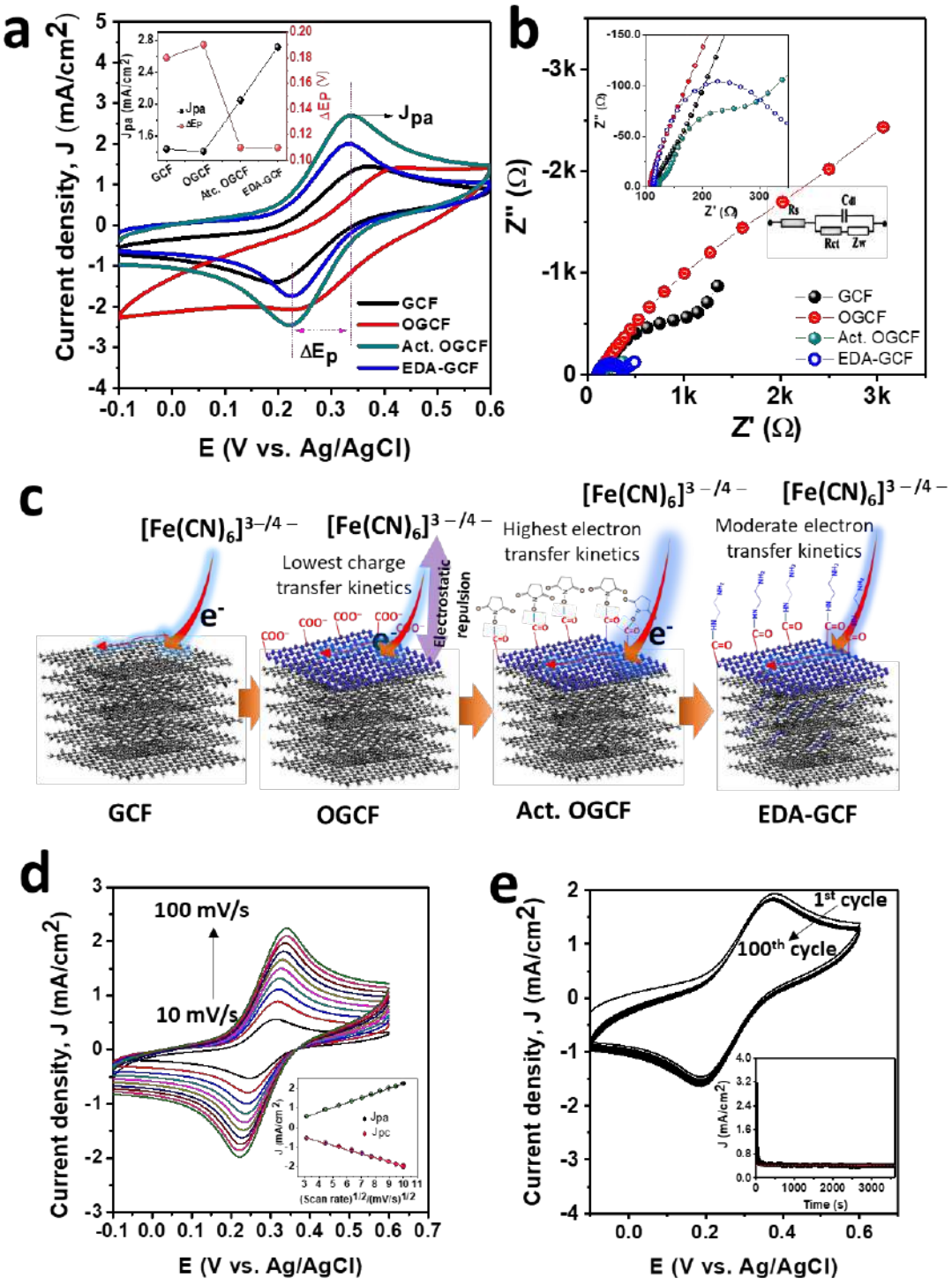

Figure 4.3.4: (a) CVs (scan rate: 100 mV/s) (inset shows the plots of the summary of J_{pa} and ΔE_p) and (b) Nyquist plots (inset shows the magnified Nyquist plots) of GCF, OGCF, Act. OGCF, and EDA-GCF electrodes. (c) Schematic of the GCF modification and electron transport of the various electrodes. (d) CVs of EDA-GCF electrodes in $[Fe(CN)_6]^{3-/4-}$ redox electrolyte solution at different scan rates (10, 20, 30, 40, 50, 60, 70, 80, 90, and 100 mV/s) and (e) consecutive CVs (100 cycles)

of the EDA-GCF electrodes in $[Fe(CN)_6]^{3-/4-}$ redox electrolyte solution at a scan rate of 100 mV/s (inset shows the CA plot of the EDA-GCF electrodes in $[Fe(CN)_6]^{3-/4-}$ redox electrolyte solution at 0.335 V) (Copy right Adeel et al.in submission).

To acquired information on conductivity and, more in general, on the electrochemical activity of the investigated surface materials (of bare, activated, and EDA-functionalized GCF) at micrometer spatial resolution, a series of scanning electrochemical microscopy (SECM) measurements were performed. They were carried out with the substrates being unbiased, thus allowing probing their surface status without any direct electrochemical perturbation. The SECM tip signal was originated from the one electron oxidation of $Fe(CN)_6^{4-}$ to $Fe(CN)_6^{3-}$, while keeping the potential of the microelectrode constant at 0.45 V, vs. Ag/AgCl reference electrode. When the tip was positioned far above the substrate, the diffusion-limited current predicted by Eq. (1)[32] (see the experimental section) was recorded. When the microelectrode tip was approached to the investigated surface, the tip current was perturbed from its value in the bulk solution by the presence of the substrate in a close proximity. Two situations can occur. If the microelectrode tip approaches an insulating or low conducting/active region, the current would decrease as the tip-to-substrate distance decreases, due to blockage of diffusion of the electroactive species toward the tip[33] (negative feedback). Instead when the microelectrode tip approaches a conducting/active region, the current increases with decreasing the tip-to-substrate distance, due to regeneration of the redox mediator at the substrate/solution interface[33]. The current increase is the larger, the higher are the conductivity/activity and the size of the substrate. Therefore, the analysis of the approach curves provided useful information about the nature and reactivity of the investigated substrate. **Figure 4.3.5a** shows typical approach curves obtained above the various substrates. It is evident that in any case positive feedback occurs. However, the normalized current, I/I_0, at close distances, follows the order: Act. OGCF > EDA-GCF > GCF, indicating a decreasing conductivity/activity

(or smaller conductive/active regions) of the substrates in the same order. The local activity of the substrates was ascertained also by imaging about a few hundred μm^2 of the surface area of the substrates by SECM. These experiments were performed by positioning the platinum micro-tip at about 20 µm above the substrate surface (by the use of an approach curve) and then scanning the tip across the *x–y* plane parallel with the surface. From the images (**Figures 4.3.5 b, c, and d**), it was evident that, on average, the highest current values were observed at the Act. OGCF and the lowest at GCF. This trend well agrees with the electrochemical CVs and DPVs measurements.

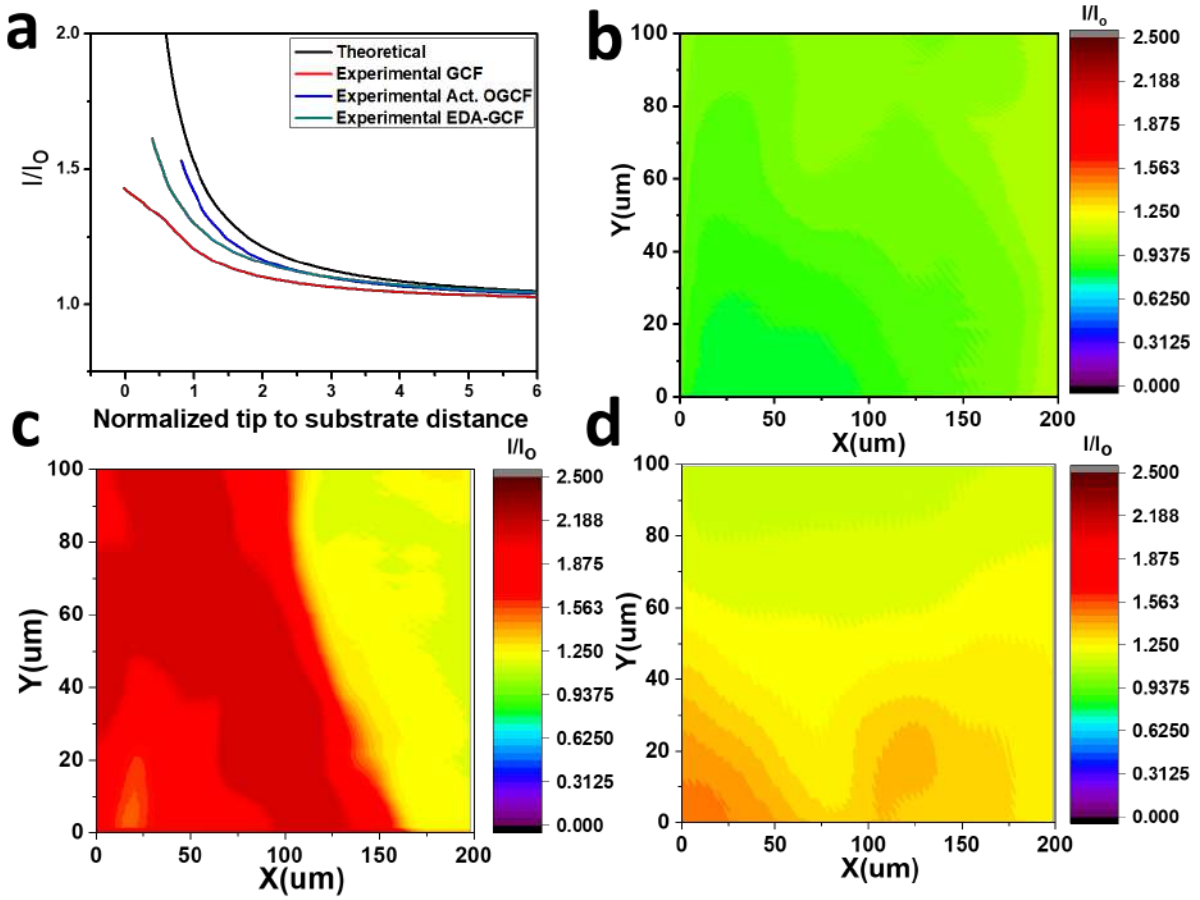

Figure 4.3.5: (a) Approach curves and SECM images recorded above the (b) GCF, (c) Act. OGCF, and (d) EDA-GCF substrates (Copy right Adeel et al.in submission).

Prior to establishing the performance of the immunosensor for the detection of SARS-CoV-2 SP, the effect of the anti-SARS-CoV-2 and the SARS-CoV-2 SP binding time was investigated and

optimized. To this purpose, anti-SARS-CoV-2 (1 μg/mL) was immobilized onto an EDA-GCF electrode with the immobilization time of 30 min, 1 h, and 3 h in a medium containing PBS (pH 7.4). DPV, using the $[Fe(CN)_6]^{3-/4-}$ redox couple, was employed to establish the inhibition effect on the mass transport arising from attachment of anti-SARS-CoV-2 to the modified-electrode surface. It was found that the highest decrease of the current density was obtained after 1h immobilization. This was therefore considered as the optimized immobilization time. Then, SARS-CoV-2 SP (1 μg/mL) was allowed to bind at the optimized anti-SARS-CoV-2 modified electrode for 10, 15, 30, and 45 min in PBS (pH 7.4). The highest decrease of the current density occurred when 30 min incubation was employed. It was used for the detection of SARS-CoV-2 in further electrochemical analyses. The inhibition effect of the mass transport was afterwards exploited for the SARS-CoV-2 SP quantification.

In order to obtain information on surface conductivity/activity upon the attachment of antibody and the SP onto the EDA-GCF surface under the above optimized conditions, SECM images were also recorded. The attachment of the antibody led to the EDA-GCF surface becoming less conductive/active, compared to bare EDA-GCF, due to the antibody steric hindrance, which inhibits the mass transfer of the redox probe towards the active zones of the electrode. The latter effect was further enhanced after the binding of the spike protein to the antibody. This result confirmed that the inhibition effect of the mass transport of the $[Fe(CN)_6]^{3-/4-}$ redox couple could be exploited for the SARS-CoV-2 SP quantification.

Figure 4.3.6a shows the DPV responses obtained at EDA-GCF, anti-SARS-CoV-2/EDA-GCF, and SARS-CoV-2 SP/anti-SARS-CoV-2/EDA-GCF electrodes in the solution containing $[Fe(CN)_6]^{3-/4-}$ redox couple. It is evident that after the covalent immobilization of the antibody onto the EDA-GCF electrode surface, the J_{pa} decreased from 2.07 mA/cm^2 to 0.93 mA/cm^2, while

the anodic peak potential (E_{pa}) shifted from 270 mV to 295 mV, conceivably due to a decrease of the kinetic of the electron transfer process. A similar effect was reported in the literature, upon immobilizing bulky molecules (or other antibodies) onto an electrode surface, and attributed to a steric hindrance, preventing full access of the redox probe at the electrode surface[34,35]. The subsequent binding of the SARS-CoV-2 SP onto the anti-SARS-CoV-2/EDA-GCF, induced an additional decrease of the J_{pa} (down to 0.459 mA/cm^2) and a further positive shift of the E_{pa} (321 mV), related to a further steric hindrance due to the SP, which in turn makes the electrode surface accessibility more difficult[34,35]. The DPV results are highly consistent with the variation of the J_{pa} and the ΔE_p (0.10, 0.17, and 0.20 V, respectively, for EDA-GCF, anti-SARS-CoV-2/EDA-GCF, and SARS-CoV-2 SP/anti-SARS-CoV-2/EDA-GCF) observed in the CVs (inset of **Figure 4.3.6a**).

The effect of SARS-CoV-2 SP concentration on the DPV signals was investigated to obtain a calibration curve. **Figure 4.3.6b** shows a series of DPVs recorded after binding of varying concentrations of SARS-CoV-2 SP (0 -1000 ng/mL in PBS) at the anti-SARS-CoV-2/EDA-GCF probe. The J_{pa} for $[Fe(CN)_6]^{3-/4-}$ redox probe decreased linearly with increasing the SP concentration; the linear regression analysis of the of J_{pa} vs. Log[SARS-CoV-2 SP] (inset of **Figure 4.3.6b**) provided the following equation J_{pa} (μA/cm^2) = – (146.62 ±3.42) log[SARS-CoV-2 SP] (ng/mL) + 467.75±4.20 (R^2 = 0.998). The detection limit obtained as the signal to noise ratio equal to three (S/N = 3) was 27 pg/mL.

The practicability of the immunosensor for the detection of SARS-CoV-2 SP was examined by measuring the SP from diluted human blood plasma (BP) samples. The as-prepared BP was diluted with PBS and subsequently spiked with varying concentrations of SARS-CoV-2 SP. **Figure 4.3.6c** shows the DPV signals recorded for $[Fe(CN)_6]^{3-/4-}$ at the anti-SARS-CoV-2/EDA-GCF

imunosensor after binding of SP over the concentration range (0-1000 ng/mL in diluted BP). As for the PBS solution, the J_{pa} decreased linearly with increasing the SP concentration from 0 to 1000 ng/mL (inset of **Figure 4.3.6c**); the linear regression analysis of the experimental points provided: J_{pa} (μA/cm^2) = – (143.62 ±3.80) log[SARS-CoV-2 SP] (μg/mL) + 461.50±4.65 (R^2 = 0.998) and LOD (S/N = 3) of 25 pg/mL. The values of intercept and slope obtained in dilute blood plasma very close to those evaluated in PBS suggests the suitability of the proposed sensor for the practical detection of SARS-CoV-2 is real biological samples.

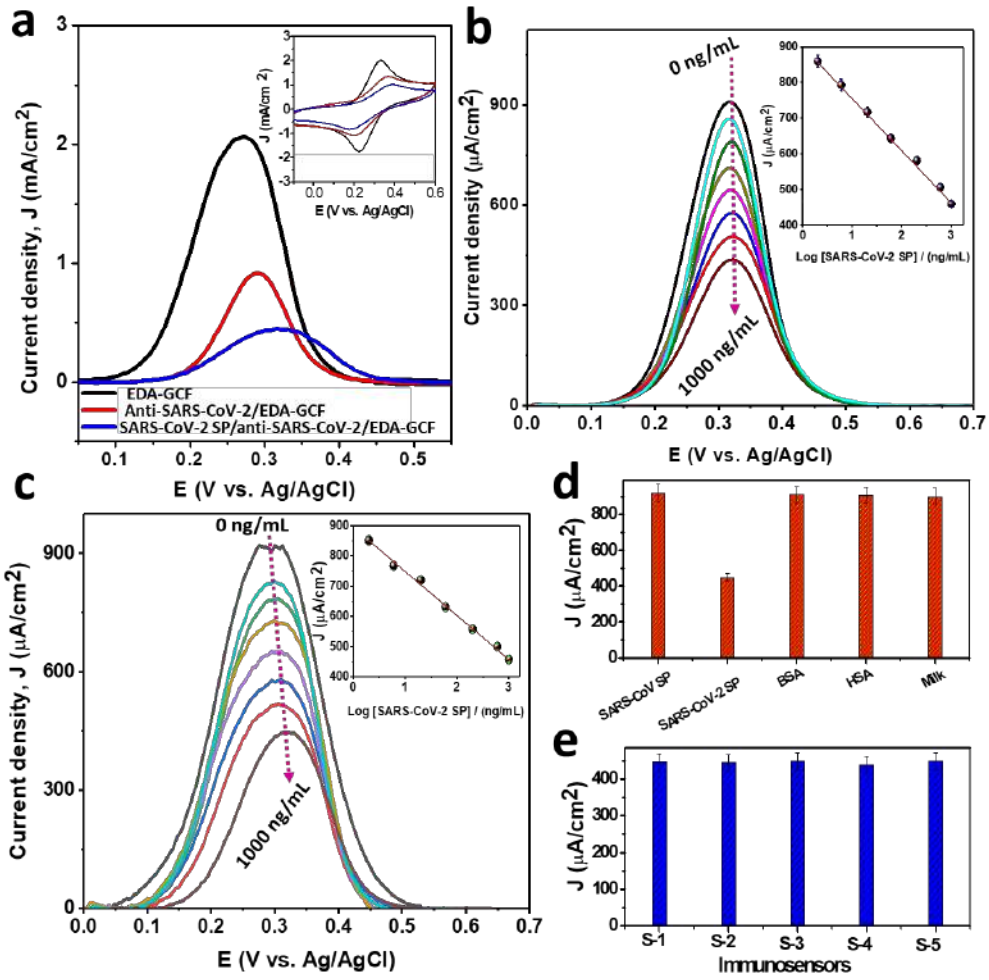

Figure 4.3.6: DPV responses of EDA-GCF, anti-SARS-CoV-2/EDA-GCF, and SARS-CoV-2 SP anti-SARS-CoV-2/EDA-GCF electrodes in $[Fe(CN)_6]^{3-/4-}$ solution (inset shows the corresponding

CV responses at a scan rate of 100 mV/s). (b) DPV responses of the anti-SARS-CoV-2/EDA-GCF sensor probe with the binding of different concentrations of SARS-CoV-2 SP (0, 2, 6, 20, 60, 200, 600, and 1000 ng/mL in PBS) (inset shows the corresponding calibration plot). (c) DPV responses of the anti-SARS-CoV-2/EDA-GCF sensor probe with the binding of different concentrations of SARS-CoV-2 SP (0, 2, 6, 20, 60, 200, 600, and 1000 ng/mL in diluted BP) (inset shows the corresponding calibration plot). (d) Bar diagram of the DPV current responses upon the binding of SARS-CoV-2 SP and different interferences and (e) DPV current responses of five different immunosensors upon the binding of SARS-CoV-2 SP (Copy right Adeel et al.in submission).

The selectivity of the immunosensor was evaluated by comparing the DPVs for the $[Fe(CN)_6]^{3-/4-}$ redox probe obtained with the anti-SARS-CoV-2/EDA-GCF sensor using SARS-CoV SP (5 μg/mL), SARS-CoV-2 SP (1 μg/mL), BSA (5 μg/mL), HSA (5 μg/mL), and different available proteins from diluted milk. The corresponding DPV responses are summarized in **Figure 4.3.6d**. No significant current change was induced by the SARS-CoV SP, BSA, HSA, and proteins from milk, indicating that the immunosensor is highly specific to SARS-CoV-2 SP.

The reproducibility of the anti-SARS-CoV-2/EDA-GCF probe preparation was investigated using five independent immunosensors. The corresponding DPV results (summarized in **Figure4.3.6e**) revealed a very low RSD (1.20%) for the J_{pa} of $[Fe(CN)_6]^{3-/4-}$ signals upon the binding of SARS-CoV-2 SP (1 μg/mL in PBS), suggesting the high reproducibility in the preparation of the immunosensor.

Electrochemical stability of the immunosensor was investigated by seven consecutive DPV (**Figure 4.3.7a**). The DPV results revealed a very low RSD (1.90%) for the J_{pa} of the $[Fe(CN)_6]^{4-}$ oxidation process, while the current density in the CA plot was almost unchanged after 1 h. These results indicated the high electrochemical stability of the immunosensor and its suitability for a series of point-of-care measurements.

The shelf stability of the immunosensor was studied after storing the sensor for three weeks at 4 ^{o}C. The J_{pa} of $[Fe(CN)_6]^{4-}$ oxidation process ,obtained from the DPV responses after the binding

of SP (1 µg/mL in PBS) at the immunosensor probe, measured to at a week intervals, revealed a very low RSD (3.30 %) (**Figure 4.3.7b**). Also, these results confirm that the here proposed immunosensor is highly suitable for the development of accurate and reliable disposable SARS-CoV-2 systems.

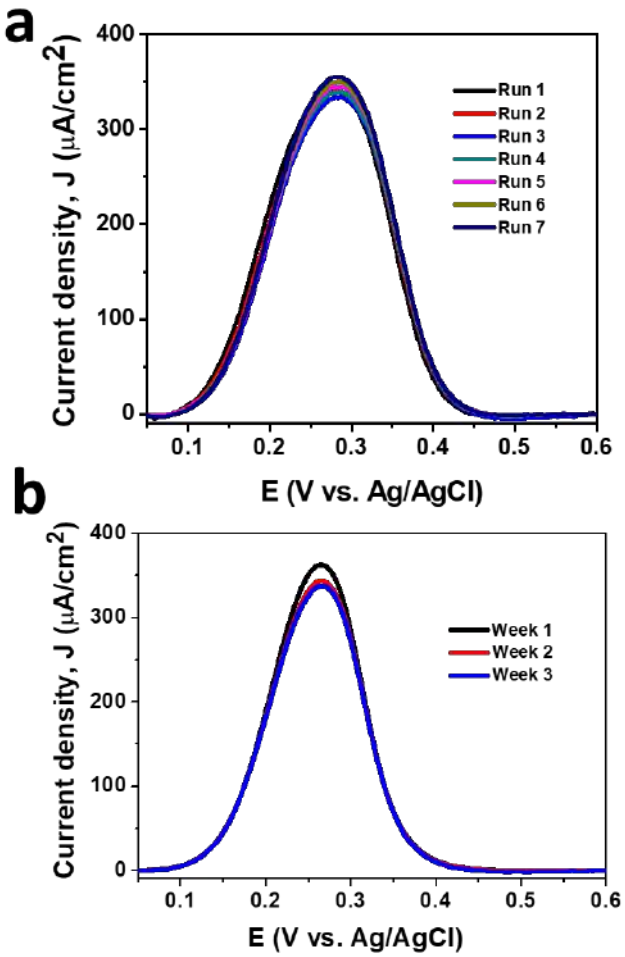

Figure 4.3.7: Repetitive DPV signals of a freshly prepared immunosensor and (b) after storing the sensor for three weeks at 4 °C (measured every week interval) for the oxidation of $[Fe(CN)6]^{3-/4-}$ after the binding of SARS-CoV-2 SP (1 µg/mL) in PBS (pH 7.4) (Copy right Adeel et al.in submission).

Section 4.4 Nanomaterials and therapy to be employed in in ovarian cancer therapy

Presently, cancer therapy including ovarian cancer, is mostly constrained to surgery, radiation, and chemotherapy, but they have several disadvantages and often fail to cure the illness[36]. In this second part of thesis, we propose strategies, exploiting nanomaterials to circumvent some of the problems mentioned in the introduction to bring advancement in ovarian cancer research, but that can also find applications, more in general, in other cancer inhibition treatments. In particular, the following strategies were investigated and will be discussed in detail in the next sections.

-Use of drug delivery systems by using a novel compatible hydroxylated boron nitride nanosheets as carrier of doxorubicin for ovarian cancer therapy.

- Use of carrier-free delivery systems of a hydrophobic drug (MAGL) for ovarian cancer. The super hydrophobic molecules of the drugs were solubilized by reducing their size with different surfactants and then covered with albumin nanocrystals to obtain stable and safe *in vivo* carrier systems.

-Use of self-therapeutic nanomaterials that can act like a “magic nano bullet” free from extra therapeutic compounds or external stimuli dependency to make these systems reliable for practical or clinical purposes.

Each of the above-mentioned approaches have advantages and drawbacks, as will be referred in the sections below.

Section 4.5 Crystalline Biocompatible Hydrolytic Boron Nitride Nano Particles (BN-OH) for Cancer therapy

Here boron nitride nanosheets were synthesized and used as carriers of therapeutic drug (doxorubicin). The materials were loaded with doxorubicin and tested on different ovarian cancer cells line. The schematic illustration of the work is presented in **Figure 4.5**

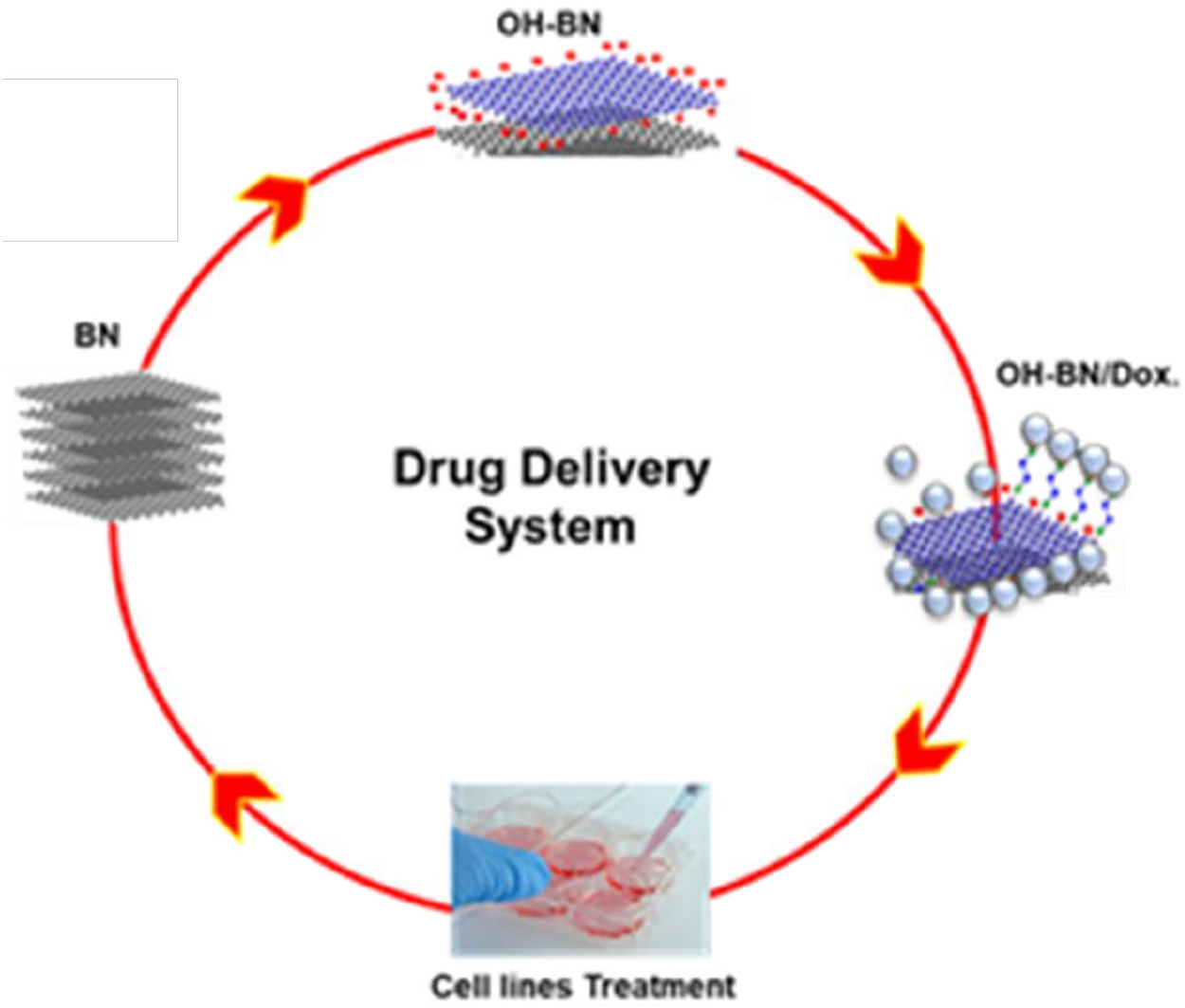

Figure 4.5: Schematic illustration of hydroxylated boron nitride nanosheets for drug delivery application (Copy right Adeel et al.in submission).

4.5.1 Exfoliation Mechanism

A very simple room temperature method was used to synthesize boron nitride nanosheets, following a previously reported method[37,38] (**Figure 4.5.1)**. Bulk boron (BN) was, initially, treated with H_2SO_4; H^+ and SO_4^- ions were intercalated in its structure, thus enlarging the distance between adjacent sheets. A further enlargement occurred after treatment with $KMnO_4$ by the intercalation of K^+ and MnO_4^- ions, and the sheets get exfoliated with the reduction of MnO_4^- to

MnO_2. The exfoliated boron nitride nanosheets containing MnO_2 was further treated with H_2O_2, thus providing impurity-free boron nitride sheets with high OH functionalization[37].

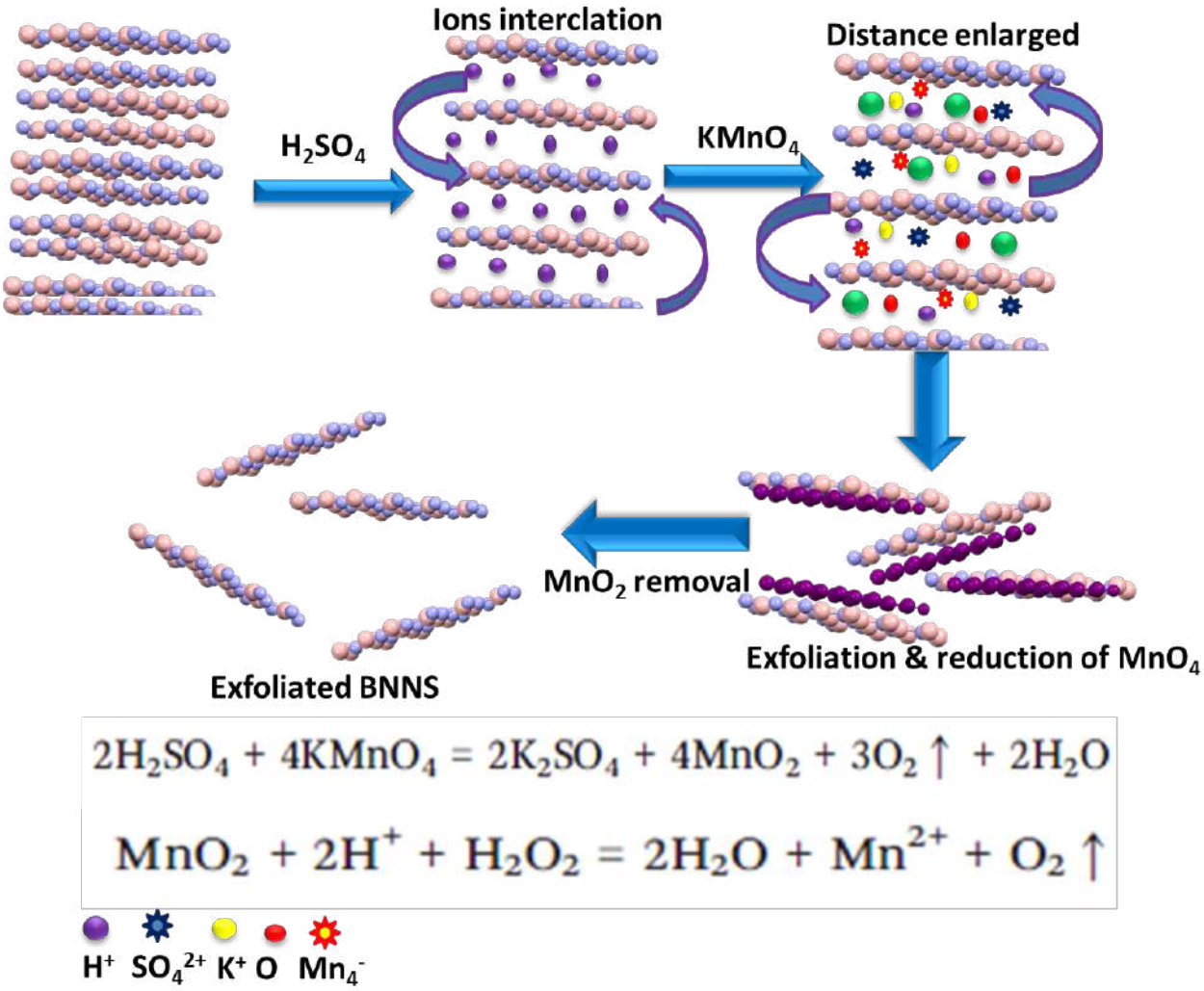

Figure 4.5.1: Schematic illustration of the synthesis of boron nitride nanosheets (Copy right Adeel et al.in submission).

4.5.2 XRD, Raman and FTIR Study

For the structural analysis and to confirm the occurrence of exfoliation of the boron nitride nanosheets from bulk BN, XRD analysis was performed, and relevant results are shown in **Figure 4.5.2 a**. Both bulk and exfoliated boron nitride nanosheets display a well sharp peak at about

26.70° due to the *hkl* reflections of the (002) plan. However, while the BN has a FWHM = 0.42, the OH-BN peak results slightly shifted towards a lower angle and has a FWHM=0.62. This result suggests that the exfoliation of boron nitride (BN) to boron nitride nano sheets occurs across (002) plan and their surfaces are functionalized with OH groups (**Figure 4.5.2 a),** as also reported in the literature[37,38]. Moreover, as the overall results found here are close to the theoretical ones presented in JCPDS card 34-042, they also confirm the purity of the OH-BN samples [38]. **Figure 4.5.2 c** shows the Raman results. A clear E_{2g} phonon mode, due to B-N bond vibration within the plane, is observed in both types of materials. However, the OH- BN Raman E_{2g} signal is shifted towards lower Raman wavenumbers and with a higher FWHM value, which confirms the occurrence of the exfoliation (i.e., the increase of the interlayer distance) and the functionalization with OH groups on the surface of OH-BN (**figure 4.5.2 d**)[37,38]. To further confirm the presence of OH onto the OH-BN surface, FTIR spectra were recorded **(figure 4.5.2 e)**. As is evident, both BN and OH-BN display a series of peaks that fall at very close wavelengths. However, in the region highlighted in green in **Figure 4.5.2 e,** the peaks of OH-BN are slightly shifted towards lower wavenumber values and have a higher intensity, compared to those of BN. This clearly indicates the successful functionalization of the BN surface [37]. The peaks that also appear at the same wavelengths for the BN samples can be due to water absorption from the environment.

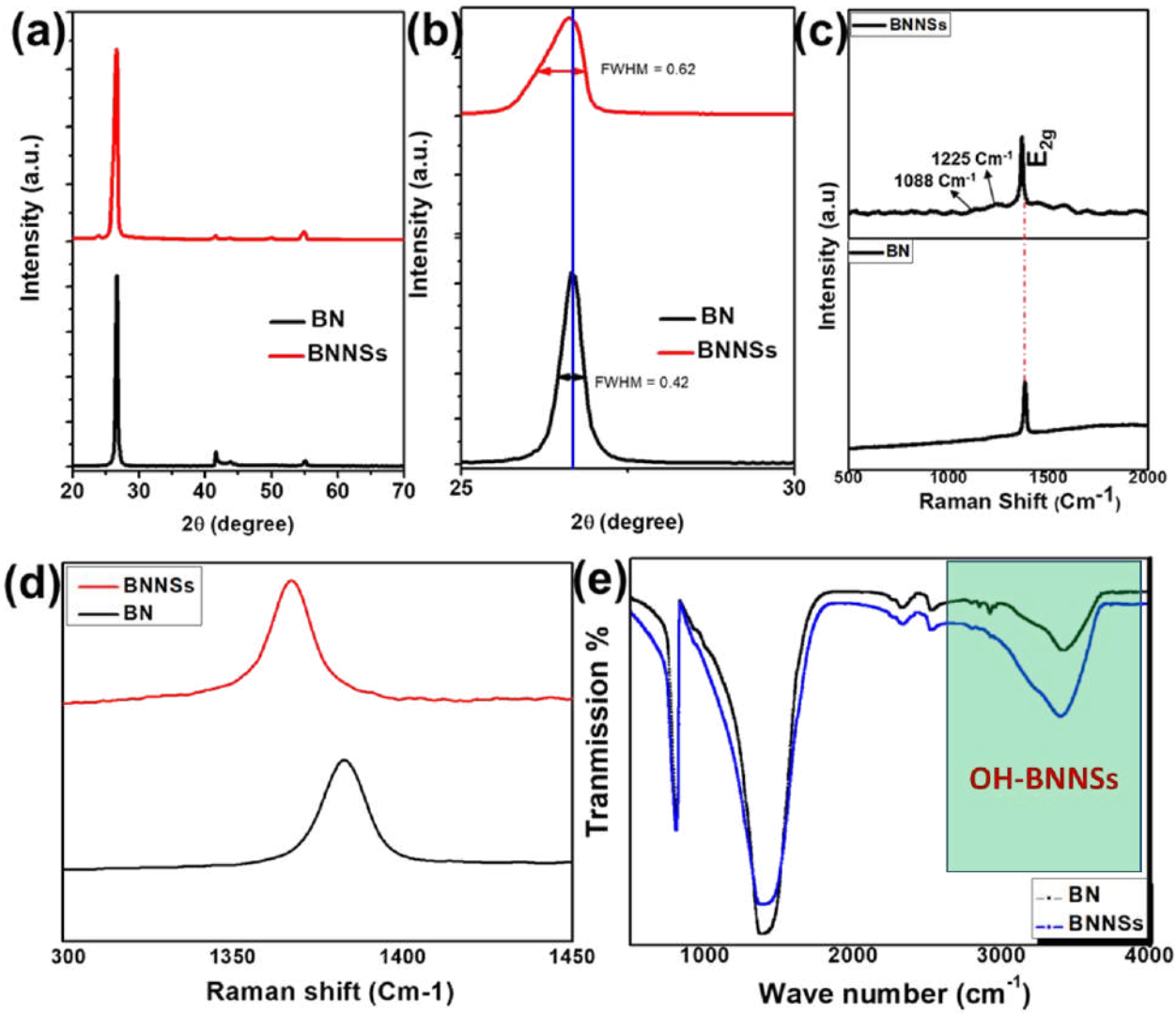

Figure 4.5.2: (a) and (b) are the XRD pattern, (c) & (d) are Raman results and (e) is the FTIR pattern of boron nitride nanosheets (Copy right Adeel et al.in submission).

4.5.3 XPS, UV, BET, DLS and Zeta potential Study

The elemental composition and nature of bonding of the OH-BN was further assessed by XPS measurements. For the BN material, the spectrum was same as that reported in the literature[38] and therefore not shown here. **Figure 4.5.3a** shows the survey spectra of OH-BN. Very clear B, N, and O peaks can be observed without extra peaks due to impurities. Instead, the zoomed spectra (**Figure 4.5.3 b,c)** show peaks at the binding energy of 189.22eV and 396.89 eV**,** indicating the

presence of B-N and N-B bonds[38]. The purity of the OH-BN was further confirmed by UV-spectroscopy (**Figure 4.5.3 d)**. A clear absorption band at 210.7 nm, without extra bands, was observed in the in OH-BN spectrum, and it is close to the 205 nm band of BN . Again, these results agree well with literature reports[38,39].

The BET analysis was performed to evaluate the porosity and particle size of the material. Relevant results are displayed in **Figure 4.5.3 e**. A clear increase in surface area, pore size and pore volume were observed in case of OH-BN, compared to BN. Hydrodynamic radius and surface charge of both OH-BN and BN were obtained by dynamic light scattering (DLS) and Zeta potential measurements **(Figure 4.5.3 f)**. The results indicated that the size of OH-BN material decreased (around to 250 nm), compared to that of bulk BN (above 350 nm). Correspondingly, the zeta potential value of -18.5 mV for OH-BN was lower compared to -26.5 mV for OH-BN, while both materials were characterized by a poly-dispersibility *(PD*) index less than 1, which indicated reliable measurements. The OH functionalization on the surface and smaller size help to increase the aqueous solvent dispersibility of OH-BN, compared to BN[40].

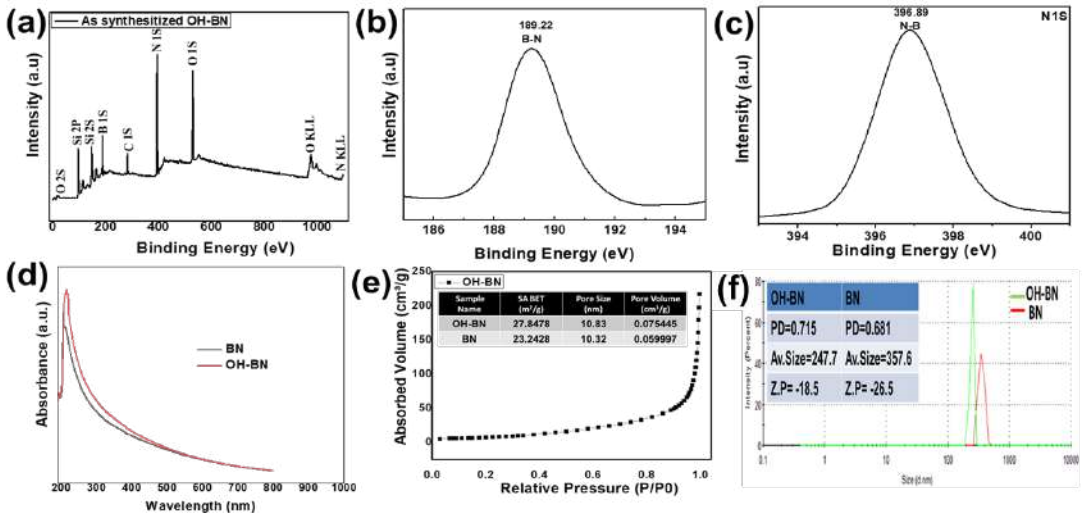

Figure 4.5.3: (a), (b) and (c) are the XPS pattern, (d) is the UV-Vis results, (e) are BET analysis and (f) is the DLS and Zeta potential data. Note that in the figure, the boron nitride nanosheets is indicated as BNNs; it corresponds to OH-BN in the text (Copy right Adeel et al.in submission).

4.5.4 SEM, TEM & EDS Analysis

To acquire information on morphology of the materials, SEM and TEM measurements were performed. **Figure 4.5.4a, b** displays the SEM results of bulk BN and OH-BN. Clearly, a small thin sheet-like structure is observed in OH-BN, compared to BN. Similar results were obtained by the TEM analysis, as is shown in **Figure 4.5.4c** [37]. Both SEM and TEM results confirm the successful exfoliation of BN to provide OH-BN. SAED analysis showed a well concentric ring like behavior that are in agreement with the XRD results. In fact, the first ring corresponds to the (002) plane of XRD, while the second ring corresponds to the (100) plane of the XRD pattern[38] **(Figure 4.5.4d)**. The elemental composition of the materials was obtained by EDS analysis. The distribution of B and N elements in the samples are shown in **Figure 4.5.4e.** Full range EDS spectra are displayed in **figure 4.5.4f**, providing the presence of 53% of B and 46% of N atoms, which are very close to the naturally occruing of alternating B and N atoms in BN compound with 50 to 50 % of frequency[38]. However, the lack of other peaks due to other elements indicated the high purity of the sample after exfoliation and functionalization.

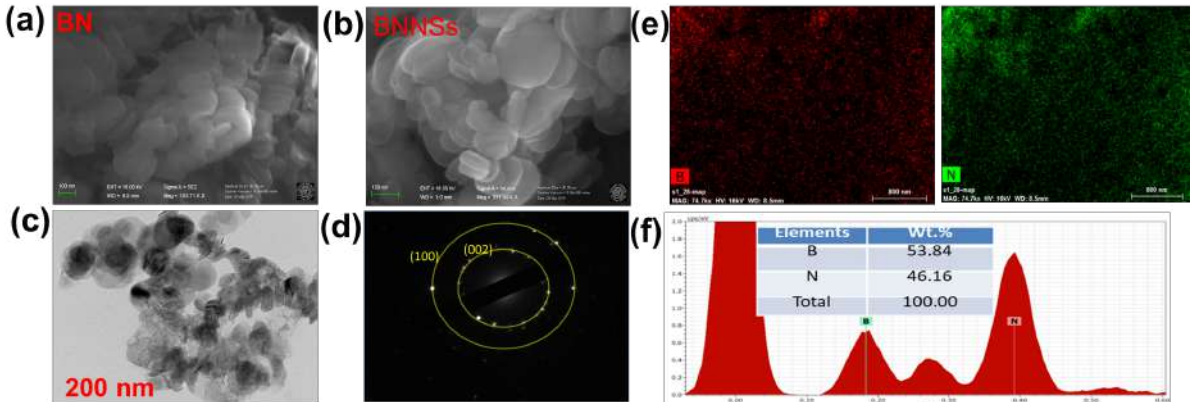

Figure 4.5.4: (a) & (b) are the SEM results of BN and OH-BNNSs, (c) & (d) are the TEM & SAED pattern, respectively (e) are EDS mapping of the component of B and N in OH-BN (f) is the EDS spectra with elemental composition of OH-BN(Copy right Adeel et al.in submission).

4.5.5 Artificial *in vivo* system stability

An artificial *in vivo* system was developed to create tumor and normal body environments. This was done by putting BN and OH-BN (1mg/mL) into physiological solution at 37 °C in the dark and then the pH was modified at the values of 5.5 and 7.4, this to check the stability of the samples under the latter conditions. After each interval of time (T0, T14, T21, T30, T45 and T60) the BN and OH-BN materials were collected and examined using surface and spectroscopic techniques. **Figure 4.5.5 a,b** shows SEM results taken at T0 and T30 for of OH-BN and BN, respectively. It can observe that the OH-BN samples show super high stability at body like and pH 5.5 conditions, compared to BN samples. In the latter cases, in fact, the materials completely degraded and were covered by a protein corona. The different behavior of the two types of materials is also evident by considering the zoom images of the SEM measurements taken at T30, where the degradation of OH-BN was very low (i.e., around 0.05%) at both pH. compared to BN, which was completely degraded morphologically. The stability of the samples was further confirmed by using FTIR spectroscopy. The results (**Figure 4.5.5 c)** showed that the spectra of the OH-BN material did not change with time. This indicating a high stability of the material up to 60 days, result assessed also by SEM analysis. Instead, in the case of BN (**Figure 4.5.5 c)** the spectra showed the appearance of a variety of new peaks in the range 1000-1800 cm^{-1}, indicating structural deformation into different specific planes.

Overall, the above results indicate that *in vivo* artificial systems, OH-BN samples are very stable at both pH investigated and could be suitable for their use as drug carrier.

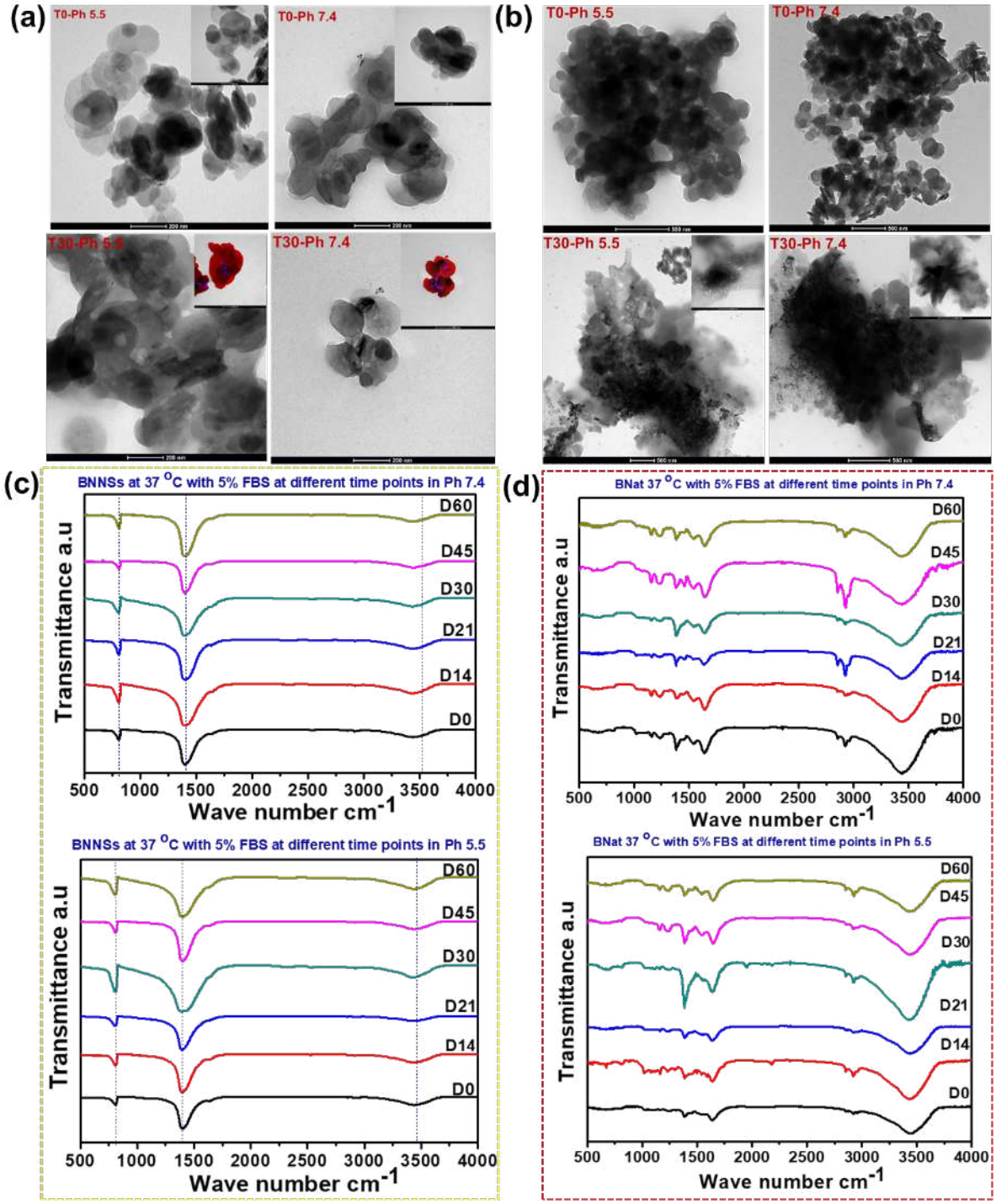

Figure 4.5.5: (a) and (b) are the SEM results of BN and OH-BN, respectively; (c) (left yellow) & (d) (right red) are the FTIR spectra of materials after different interval of time (Copy right Adeel et al.in submission).

4.5.6 Yield, Drug release and IC50 measurements

The OH-BN and, for comparison, the BN materials were utilized as carriers for doxorubicin (Dox). They were loaded with the drug and loading efficiencies of 82% and 95 % for OH-BN (OH-BN-Dox) and BN (BN-Dox), respectively (**Figure 4.5.6a)**, were found, using the UV measurements, as described in detail in **section 4.5.1** and related experimental section. The higher yield found for BN could be due to fact that the amorphous nature of the material allowed a higher amount of Dox to be adsorbed onto the material surface. In the case of OH-BN, the lower yield is conceivably related to the fact that the drug is covalently bound to the material surface through the –OH and -NH_2 groups of OH-BN and Dox, respectively[41,42]. Therefore, the amount of Dox bound is limited by the amount of OH- functional groups.

The release of Dox from the loaded samples was evaluated at pH 5.5 and 7.4, and the results obtained are shown in **Figure 4.5.6b**. It is evident that BN-Dox provided a very sustain release of Dox, compared to OH-BN-Dox. This is congruent with the stronger covalent bond involving the –OH and NH_2 groups, compared to the weaker adsorption phenomenon that characterizes the interaction between the drug and the BN material[42].

The effect of the unloaded and drug-loaded materials was tested in different cell lines in order to verify from one side their biocompatibility and, from the other side, the efficacy in the therapeutic actions, respectively.

As is shown in **Figure 4.5.6c**, both BN and OH-BN resulted to be eco-compatible with the cell investigated. On the other hand, OH-BN-Dox and BN-Dox materials were effective in inhibiting the cell growth. Actually, the inhibition effect was same as that provided by treating the cells with free- Dox[43]. This indicates that Dox loaded in the nanomaterials keeps the same structure as that of the free drug without losing its potency[44].

(a)

Compound	Loading Efficiency
OH-BN	82 %
BN	95 %

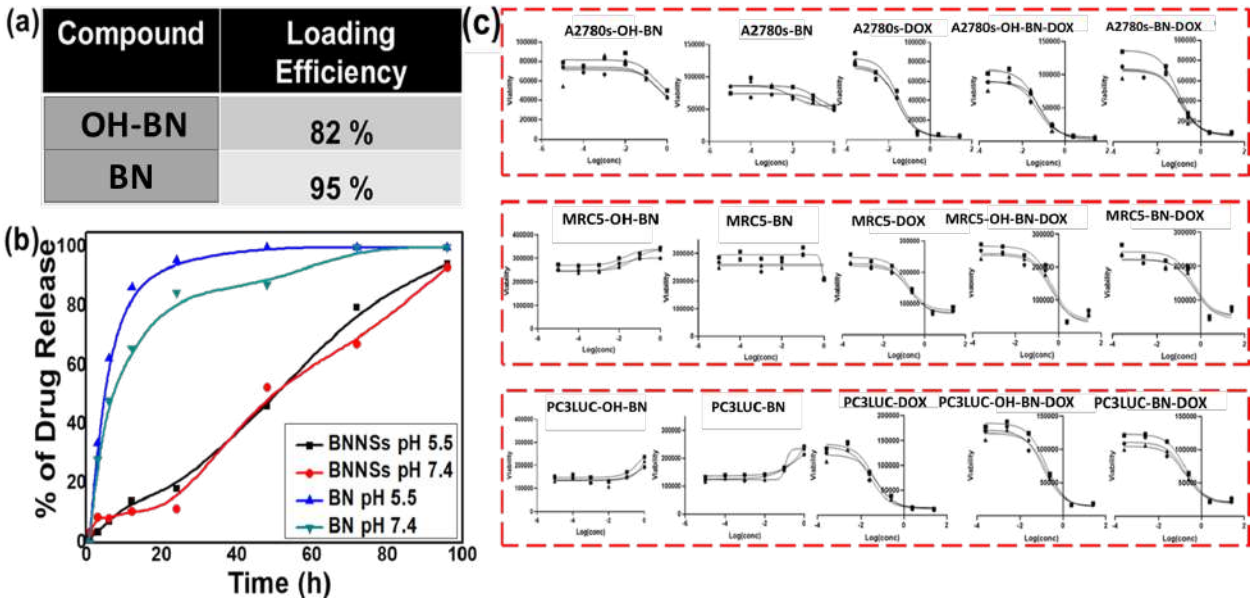

Figure 4.5.6: (a) and (b) are the Loading efficiency and release data of BN and OH-BN, respectively (c) is the IC_{50} values of BN and OH-BN at different cell lines (Copy right Adeel et al.in submission).

Section 4.6 Carrier Free Delivery System of Monoacylglycerol Lipase Hydrophobic Inhibitor for Cancer Therapy

In this part, a so-called "carrier free delivery system" was developed for hydrophobic monoacylglycerol lipase hydrophobic inhibitor for ovarian cancer therapeutic applications. The graphical illustration of the work is shown in **Figure 4.6**.

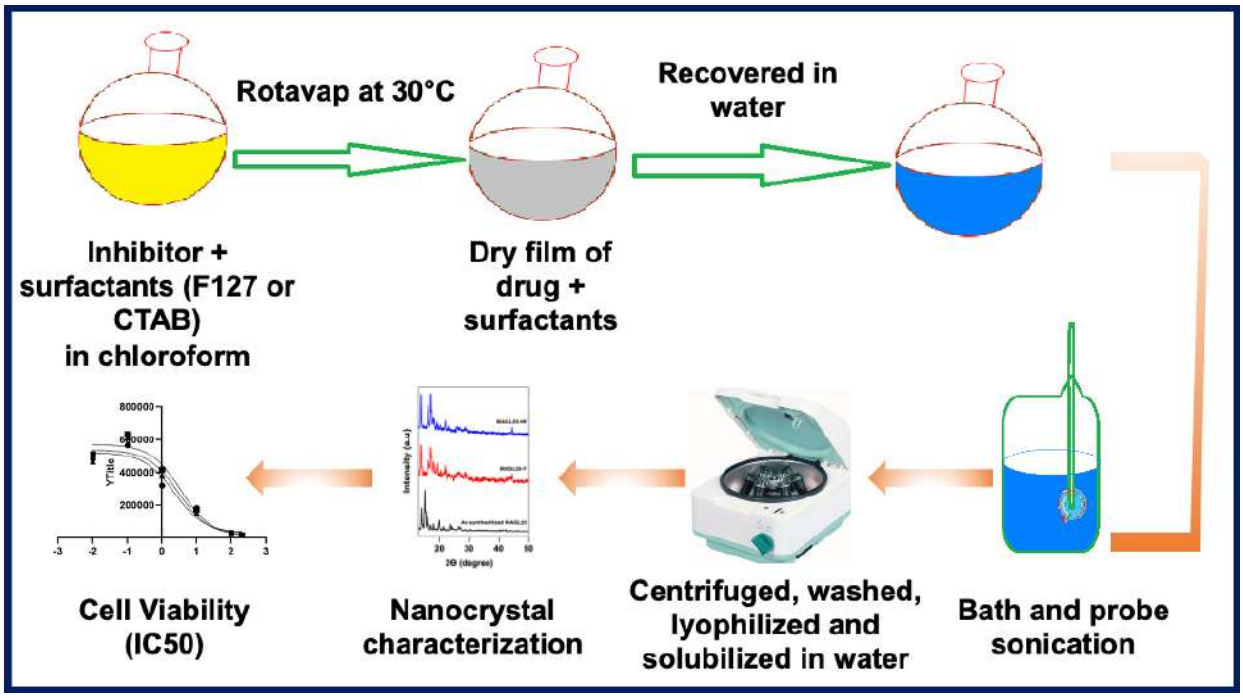

Figure 4.6 Schematic illustration of carrier free delivery system of MAGL23 inhibitor (Copy right Adeel et al.2021).

4.6.1 Nano crystallization of MAGL23

MAGL23 is an organic inhibitor of medium molecular weight (369.436 g/mol). Based on the theoretical prediction by Chemicalize software (predicted physicochemical properties are reported in Error! Reference source not found.**4.6.1**) is highly hydrophobic at physiological pH conditions (**Figure 4.6.1a**) at which it is mainly in its neutral form (94% at pH=7.4) (**Figure 4.6.1b**). To verify the poor solubility of MAGL23 at neutral pH experimentally also, a solubility test was performed on bare inhibitor in powder form. The experimentally solubility was found to be lower than 0.01 mg/ml (the lowest measurable value), which is in accordance with the prediction value.

logP	4.18
Isoelectric point	3.50
Intrinsic solubility	0.808 µg/ml

pKa (strongest acid)	8.63
pKa (strongest base)	-1.64

Table 4.6.1 Physicochemical properties of the drug predicted (by Chemicalize.com) (Copy right Adeel et al.2021).

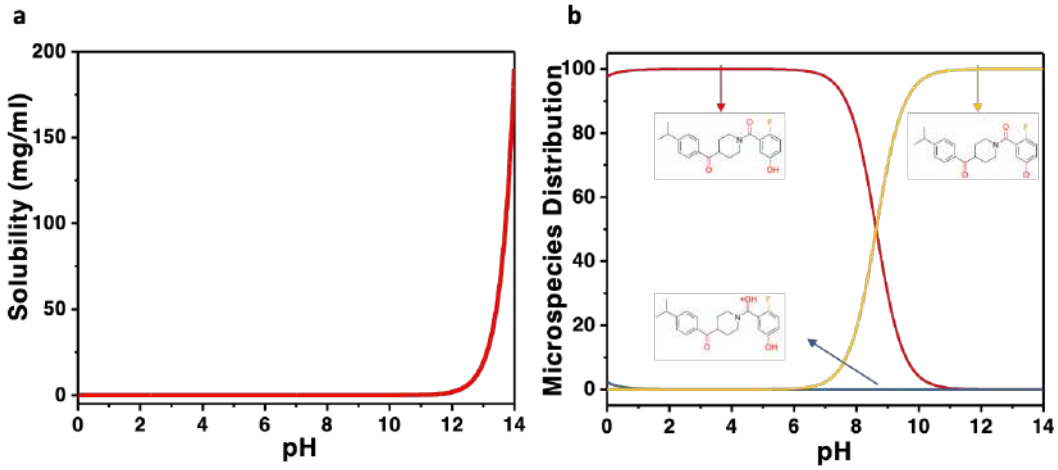

Figure 4.6.1(a) Solubility vs pH trends (predicted by Chemicalize.com) and (b) Microspecies distribution at different pH values, where microspecies in red is the neutral one, in blue is protonated at the oxygen of the amide carbonyl group (basic moiety) and in yellow is deprotonated in the phenolic group (acid moiety) (predicted by Chemicalize.com) (Copy right Adeel et al.2021).

Although neutral compounds (having zero charge) are more advantageous for biological membrane penetration than energetically charged compounds, poor solubility is always an impediment for the development and the clinical use of a cancer therapeutic compounds[45]. However, drug formulation for enhancing aqueous dispersion mostly require the use of surfactants or nanoparticles, which could result in an increased systemic toxicity of the drug[46]. Nanocrystals having high ratio between the carried drug and the excipients avoid toxicity and deliver a substantial amount of drug to the cells[47]. To overcome the MAGL23 solubility issue, the drug was formulated by nano-crystallization and was covered by albumin, because of it strongly binds to lipophilic drugs[47]. Wrapping MAGL23 nanocrystals with albumin was essential for the safe delivery without a toxic nanocarrier and helped to stabilize and to internalize the nanocrystals into

the cells[48]. The formulation resulted in an increase in drug solubility, as confirmed experimentally, and from a 0.82±0.06 mg/mL value, the solubility increased at least eighty-fold in comparison with the stand-alone drug.

4.6.2 Yield and coating

The absorbance in the UV region was employed to measure the loading efficiency of the MAGL23. Almost six separate synthesis experiments were performed; **Table 4.6.2** shows the average of the percentage of loading yield for each analyzed compound and the average of the percentage of HSA bonded to MAGL23 termed as MAGL-AF and MAGL-AC nanocrystal samples, respectively. The results showed that the nano-crystallization process solubilized MAGL23 from 0.82 mg/mL (without formulation) and the percentage of HSA bound to the MAGL23 nanocrystals were 22% and 34% by weight in MAGL23-AF and MAGL23-AC, respectively.

Samples	Yield (%)	% bonded HSA
MAGL23-F	82 ± 6	-
MAGL23-AF	59 ± 7	22 ± 4
MAGL23-C	76 ± 4	-
MAGL23-AC	58 ± 6	34 ± 11

Table 4.6.2 Percentage yield of nanocrystal samples and HAS interaction (data are reported as mean ± standard deviation) (Copy right Adeel et al.2021).

4.6.3 Morphological Analysis

The morphological study was performed by transmission electron microscopy (TEM) on formulated nanocrystal samples and bare drug in powder (MAGL23). The formulation with both surfactants reduced the crystal, the frequency distributions (**Figure 4.6.3 a,b,c**) with average sizes of 389 nm (95% CI: 336-442) and 391 nm (95% CI: 344-439) for MAGL23-AC and MAGL23-

AF, respectively. Due to decrease in size, dispersibility increased compared to MAGL23, while employing pluronic acid as surfactant.

Dispersion and homogeneity of the formulated crystals were evaluated for MAGL23-AF and MAGL23-AC (**Figure 4.6.3 d,e,f**). TEM data support the fact that surfactants allowed to increase the solubility of the drug by forming smaller and more monodisperse nanocrystals. To further confirming the hydrodynamic size of MAGL23-AF, suspended particles were investigated using the DLS technique. The size of the formulated nanocrystals was recorded around 395.4 nm (PdI 0.1), a value close to that identified by analysis on the TEM pictures, highlighting good dispersion of the crystals. Conversely, the hydrodynamic diameter of MAGL23-AC measured by DLS was larger with an average crystal size of 477.2 nm (PdI 0.2) and it could be due to self-agglomeration of the particles in solution. This unfavorable behavior and the higher toxicity of CTAB led us to proceed further with pluronic F127 formulated nanocrystals only.

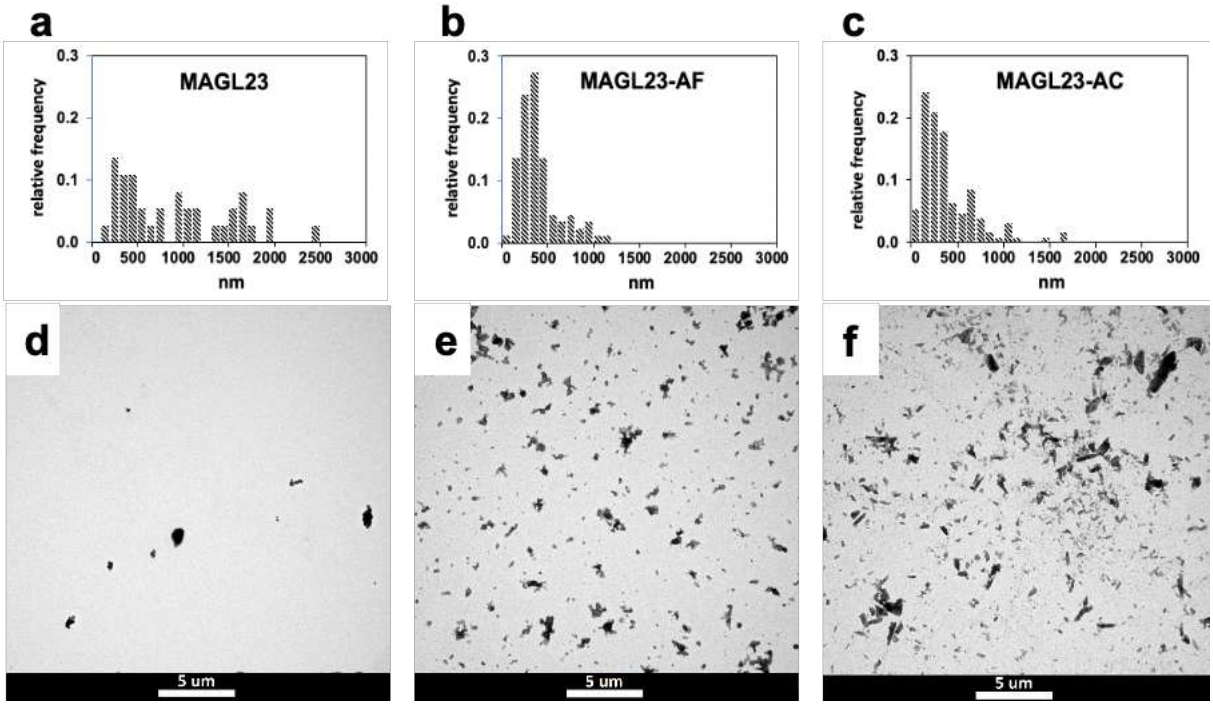

Figure 4.6.3 (a,b,c**)** Relative frequency of crystals size of MAGL23, MAGL23-AF and MAGL23-AC respectively and **(**d,e,f**)** are their corresponding TEM images (Copy right Adeel et al.2021).

4.6.4 Structural Characterizations

The nano-crystallization process was performed, and the chemical and structural properties of the drug were evaluated. In general, the structure of the drug should not change during the crystallization procedure, as any change in the structure may lead to changes of the pharmacokinetic properties.

To analyze the structure of the nanocrystals during the crystallization process, X-ray diffraction (XRD) measurements were performed. XRD pattern of nanocrystal samples MAGL-F, MAGL-AF and MAGL23 are reported in **Figure 4.6.4a** in 2θ ranging from 10 to 40°. Nanocrystals samples and MAGL23 results showed intense and sharp diffraction peaks, which demonstrate their crystalline structure. All major XRD peaks of the MAGL inhibitor are present in nanocrystal samples also, at 2θ values of 13.5, 15.75, 17.95, 18.95, 19.75, 23.5° without any significant shift or appearance of new peak. These results indicate that the crystallization method did not alter the inner crystalline structure of the MAGL inhibitor.

To further confirm the structure stability and analyze the possible interactions between the MAGL nanocrystals and the surfactants present on formulated crystal surface, FTIR spectroscopy analysis was performed (**Figure 4.6.5b**). Nanocrystal samples (MAGL-AF and MAGL-F) show mostly all MAGL23 bands (around 3430 cm^{-1} OH, 3167 cm^{-1} aromatic CH, 2865, 2929, and 2961 cm^{-1} aliphatic CH, 1683 cm^{-1} chetonic CO, 1621 cm^{-1} ammidic CO, 1320 cm^{-1} CF [49]) without any significant shift[50]. The only difference is the strong band at 3438 cm^{-1} steeper in MAGL-F and MAGL-AF, evidencing the presence of water in the samples probably due to the incomplete lyophilization[51]. The Pluronic F-127 weak band at 1100 cm^{-1} in MAGL-F is the only coating component band visible in the nanocrystal samples. Therefore, FTIR spectra demonstrated that the chemical structure of the drug remains same during the crystallization process and the drug

delivery system of MAGL nanocrystals is mainly formed by the active compound with little amount of coating components.

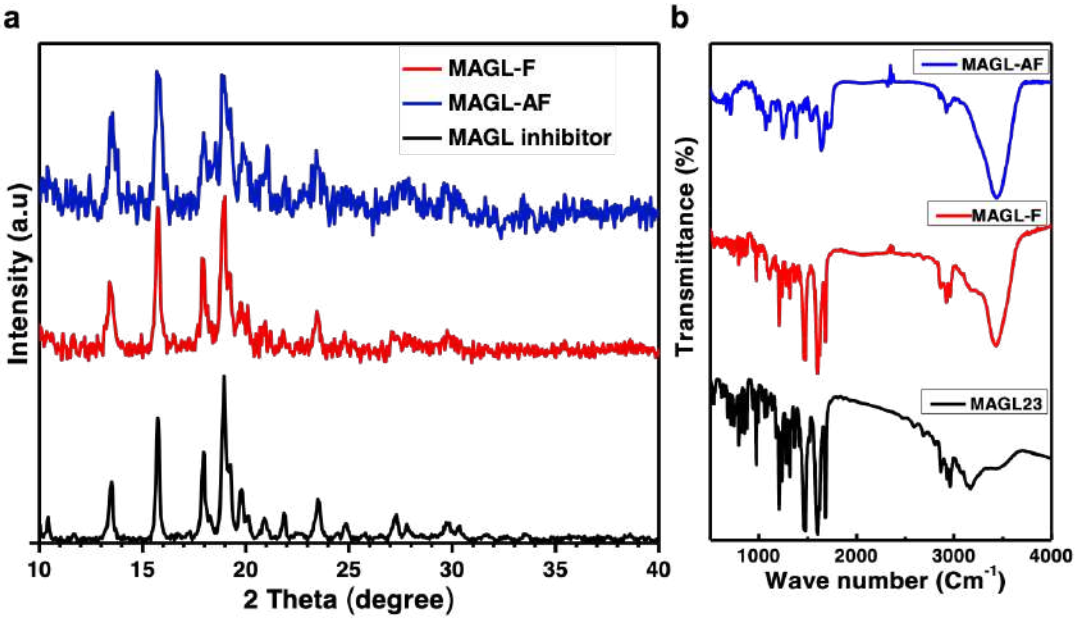

Figure 4.6.4 (a) XRD pattern and **(b)** FTIR spectra of MAGL23 (drug powder) and nanocrystals at different formulation steps (Copy right Adeel et al.2021).

4.6.5 Release profile

The results of the MAGL23-AF in vitro release tests are presented in **Figure 4.6.5** as percentage of the released drug over the initial drug quantity. The results showed that after one day only the 19 (± 7)% of the drug was released, and reached a 42 (± 6)% after three days. The low release rate agrees with the stability of the complex[52]. This means that the nanocrystal formulation allows increasing the solubility, avoiding burst release of the drug that could cause toxic effects during the blood circulation in the body. While taking advantages from the Enhanced Permeability Retention (EPR) effect and the targeting ability of the albumin, the drug should be released mainly

at the targeted site reducing the side effects and promoting the uptake in cancer cells over more cycles of cell division[53].

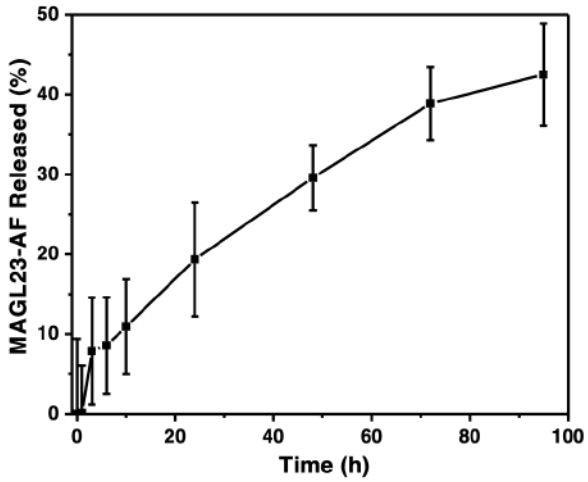

Figure 4.6.5. The release profile of MAGL23-AF as percentage of drug released percentage (%) over time (h) (Copy right Adeel et al.2021).

4.6.6 Cell viability assay

MAGL enzyme is overexpressed in a large variety of cells deriving from ovarian and colorectal cancers and has an important role in tumor progression[54]. Therefore, the new formulations of MAGL23 were tested on tumor cell lines inherent to ovarian (A2780, SKOV3 and OVCAR3) and colorectal cancers (COLO205 and HCT116).

Before testing MAGL23 nanocrystals, the toxicity of the surfactants (pluronic acid F127 and CTAB) was analyzed. The IC_{50} values are reported in **Table 4.6.6**. The IC_{50} values of CTAB are significantly lower than F-127, which suggest a marked self-cytotoxic activity. While pluronic acid F-127 did not display any significant cytotoxic activity, therefore could be considered as the best biocompatible formulant[55]. We therefore only focused on compounds treated with F-127, as a biocompatible surfactant with low intrinsic cytotoxic effects. **Table 4.6.6** shows the calculated IC_{50} values of MAGL23 initially dissolved in DMSO and MAGL23-AF dissolved in an aqueous

solution. In general, IC_{50} values were in the similar range for each tumor cell line treated with MAGL23-AF as MAGL23 stand-alone.

Cell Line	IC_{50} (μM)			
	MAGL23	MAGL23-AF	CTAB	F-127
A2780	4.0±2.0	4.1 ± 0.4	0.6 ± 0.3	>200
SKOV3	15±2*	37 ± 9	0.35 ± 0.03	>100
OVCAR3	57 ±2*	23 ± 13	0.04± 0.01	>200
COLO205	3.0 ± 0.5	27 ± 6	0.042 ± 0.002	>200
HCT116	21 ± 1.0*	16± 2	1.1 ± 0.4	>200

Table 4.6.6. IC_{50} results of MAGL, nanocrystals samples and surfactants (data are reported as mean ± standard deviation).* Data from reference[56] (Copy right Adeel et al.2021).

MAG23-AF and MAGL23 have comparable efficacy, in accord with the results obtained from the nanocrystal characterization, which revealed the maintenance of structural and chemical characteristics of the drug during the nanocrystallization procedure. Therefore, the drug delivery system allows increasing the water solubility without perturbing the molecule and consequently maintaining unaltered their activities on different cell lines. Furthermore, the albumin coating should improve the biodistribution *in vivo* because albumin operates first of all as a carrier to transport molecules in the blood[57], and secondly because albumin has a high affinity with sialoglycoprotein gp60, a protein present in the vascular endothelium and closely related to the formation of caveoles and transcytotic processes and SPARC, which are overexpressed in the tumors[58]. These properties allow MAGL23-AF to extravasate more easily in vivo compared to MAGL23, significantly increasing the possibility of concentrating the drug around the tumor mass and, hence improving its effectiveness.

4.6.7 Lysotracker Analysis

To determine the intracellular localization of MAGL23-AF, A2780 cells were labeled with Hoechst 33342 (blue nucleus) and Lysotracker (green Lysosomes). MAGL23-AF was probed with rhodamine according to the literature[48]. A time course analysis at 1 hour and 24 hours demonstrated that MAGL23-AF accumulates in the lysosomes with a Pearson's correlation coefficient (R) of 0.73 and 0.67, respectively (yellow signals, **Figure 4.6.7**). These data indicate an active mechanism of cellular import with a partial trafficking to lysosomes (**Figure 4.6.7**).

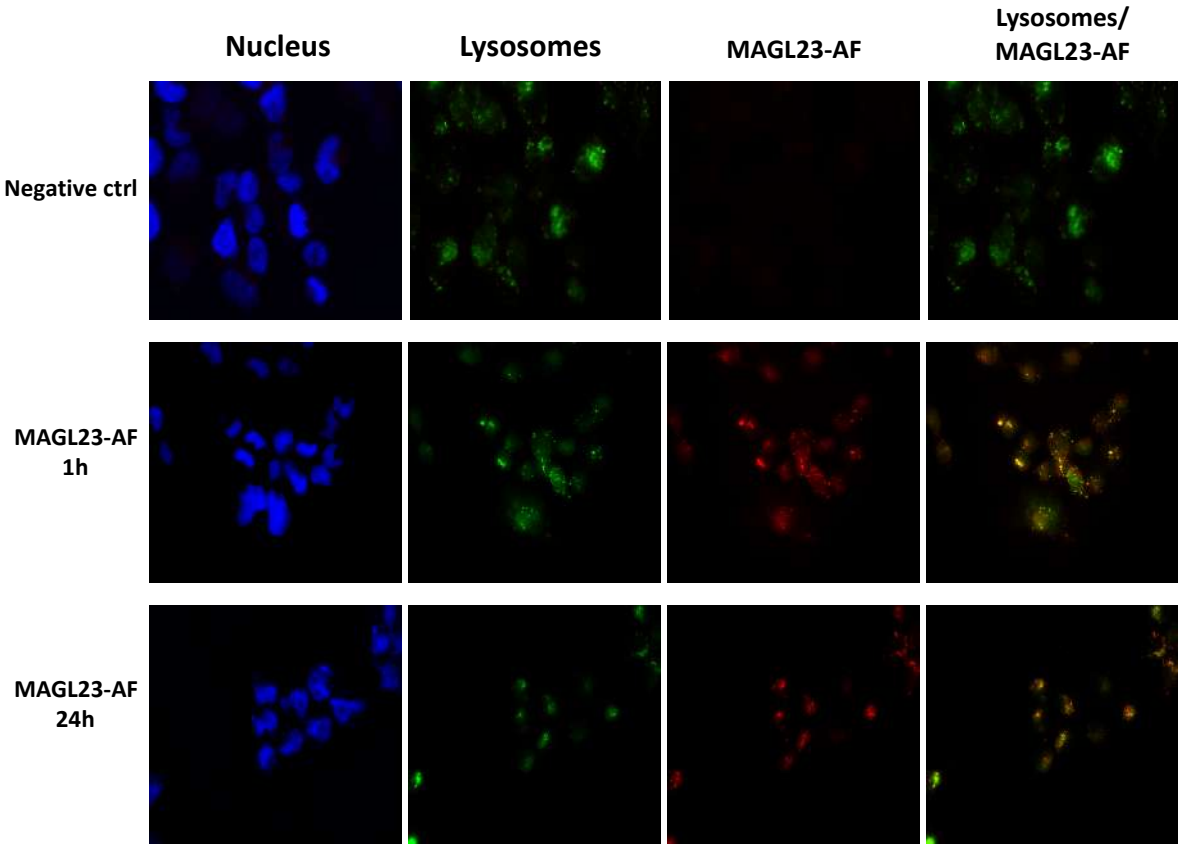

Figure 4.6.7 Cell internalization study of MAGL23-AF nanocrystals at different time points. Nucleus (blue) were stained with Hoechst 33342; Lysosomes (green) were stained with Lysotracker; MAGL23-AF were stained with Rhodamine. Yellow color implied colocalization between lysosomes and MAGL23-AF (Copy right Adeel et al.2021).

Section 4.7 Self-Therapeutic Cobalt Hydroxide Nanosheets (Co(OH)2 NS) for Ovarian Cancer Therapy

In this section we are reporting inorganic cobalt hydroxide nanosheets ($Co(OH)_2$ NS) to inhibit aggressive ovarian cancer tumors. Although high concentration of cobalt is toxic for human, however, nanoformulations have been demonstrated to be potentially safe at least at preclinical level. The graphical abstract of the study is shown in **Figure 4.7**.

Figure 4.7 Schematic illustration of self-therapeutic nanomaterials-based system for cancer therapy (Copy right Adeel et al.2021).

4.7.1 Morphological Observations

Figures 4.7.1(a-b) represents the FE-SEM images of as prepared $Co(OH)_2$, which presents the formation of interconnected 2D NS with a variable size range (ca. 10-120 nm). A very low transparency to the electron beam in the HR-TEM results **(Figure 4.7.1c)** further indicate the formation of interconnected 2D NS, which agrees with the FE-SEM results. The bright spots with a ring-like pattern having *d*-spacing of ca. 2.4, 1.45, 1.26, and 0.99 Å with the corresponding *hkl* reflections of (001), (100), (011), and $(10\bar{2})$, respectively, acquire from the selected area

diffraction pattern (SAED) (**Figure 4.7.1d**), indicating the good crystallinity and purity of $Co(OH)_2$[7]. The (001) plane containing the lattice spacing of ca. 2.40 Å between the adjacent fringes of $Co(OH)_2$NS crystals **(Figures 4.7.1 e-f)** was close to the measured *d* spacing value from the SAED result[7]. All the structural analyses confirmed the high crystallinity and purity of the as-synthesized $Co(OH)_2$NS.

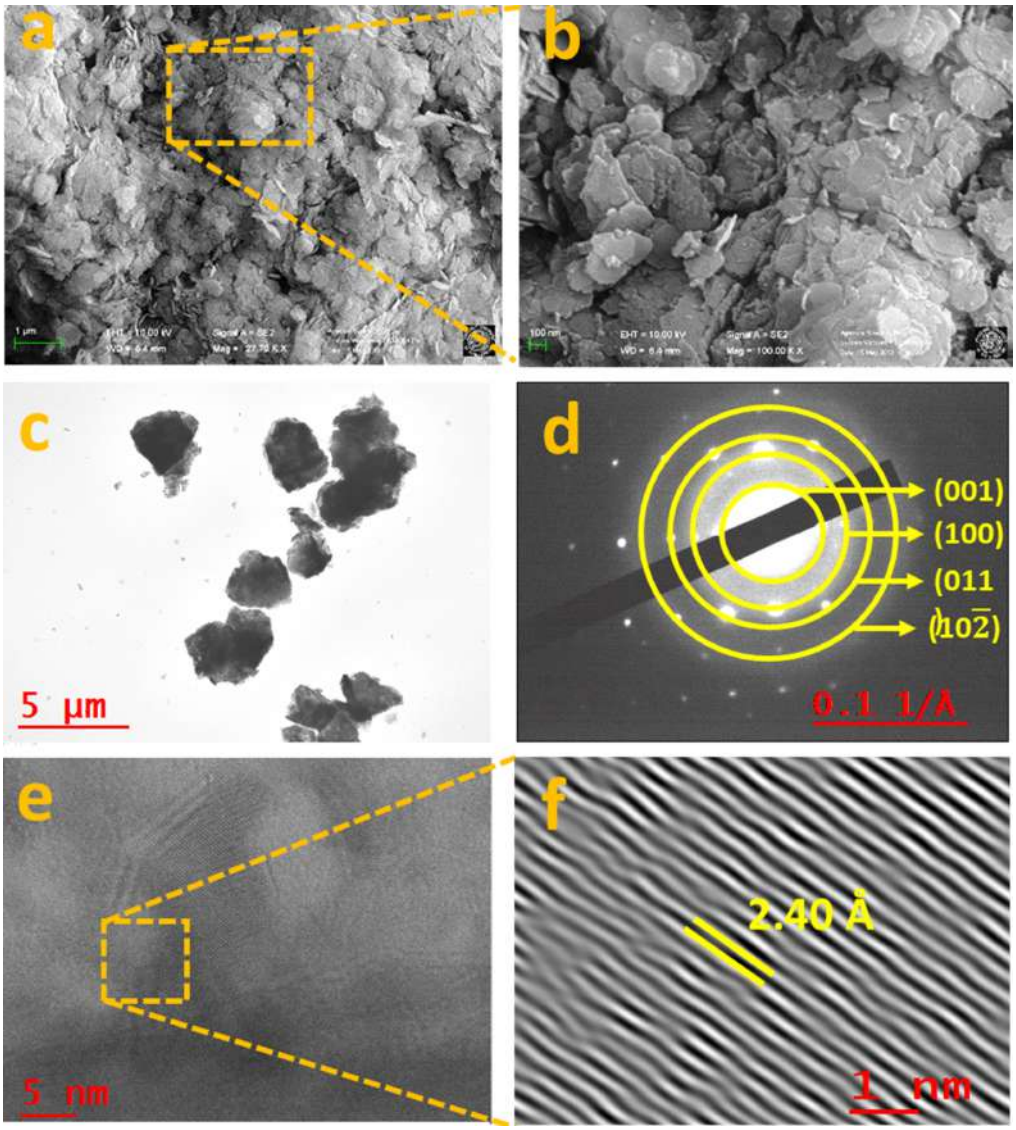

Figure 4.7.1: (a-b) FE-SEM images, © TEM, and **(d)** SAED pattern of the as-synthesized $Co(OH)_2$ NS. **(e)** HR-TEM images and **(f)** magnified calibrated lattice fringes of $Co(OH)_2$ Ns for (001) plane (Copy right Adeel et al.2021).

4.7.2 Structural Analysis

Figure 4.7.2a shows the XRD results of the as-prepared $Co(OH)_2$NS together with the simulated XRD results of $Co(OH)_2$. The simulated pattern was completely matched with the XRD results of $Co(OH)_2$NS without the occurrence of impurity peaks. The intense and sharp XRD peaks represented the high-crystallinity of the $Co(OH)_2$ NS, coherent with the TEM results. The major peaks of $Co(OH)_2$NS at 2θ angle values of ca. 19.30, 32.60, 38.10, 51.35, 57.98, and 61.75° could be assigned to the *hkl* reflections of (001), (100), (011), $(10\overline{2})$, and (110), respectively[8]. FTIR study was acquired to examine the chemical bonding in the $Co(OH)_2$ NS (**Figure 4.7.2b)**, which displayed a strong absorption peak of O-H stretching at ca. 3425 cm^{-1}, appearing from the Co-OH groups and the adsorbed water molecules[9]. The absorption bands that appeared at ca. 1115 cm^{-1} and 1575 cm^{-1} could be attributed to the C-O stretching and C-H bending, respectively. These bands could be appeared from the adsorbed or intercalated CH_3COO^- ions into the $Co(OH)_2$ NS[61]. The less intense FTIR absorption band observed at ca. 640 cm^{-1} could be ascribed to both Co-OH and Co-O bending vibrations, as similarly observed for $Co(OH)_2$, $Ni(OH)_2$, $Ni(OH)_2$-$Co(OH)_2$ layered double hydroxide[9].

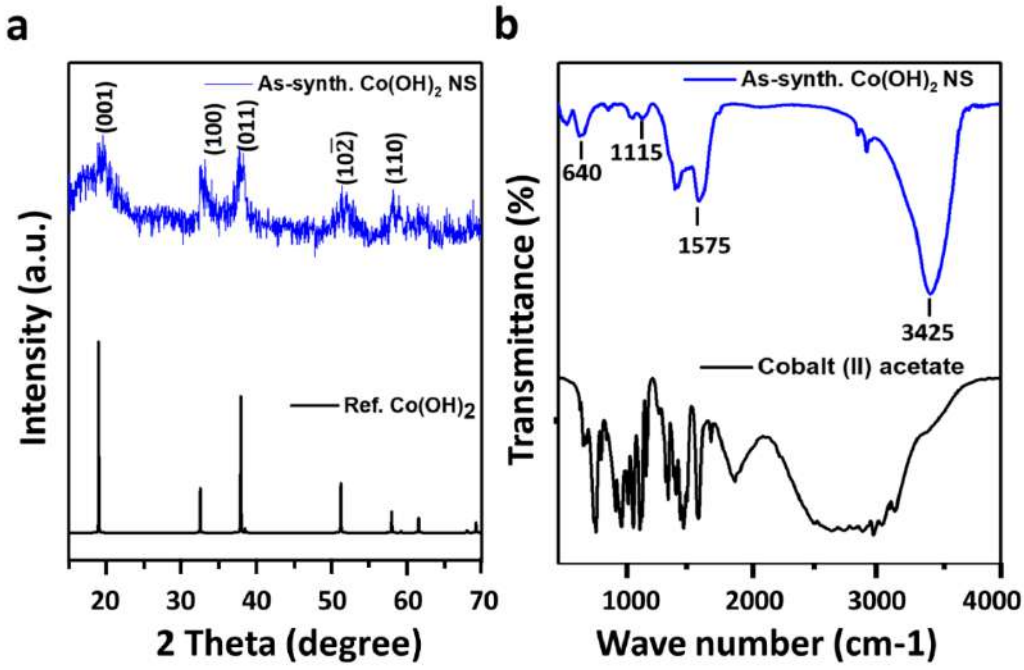

Figure 4.7.2: (a) XRD powder results of the as-prepared $Co(OH)_2$ NS along with the simulated pattern of $Co(OH)_2$. (b) FTIR spectrum of cobalt acetate and as-synthetized $Co(OH)_2$ NS (Copy right Adeel et al.2021).

4.7.3 IC50 Results

Cell viability measurements were performed on several different cell lines (ovarian, colon cancer cell lines and normal cells). The results are presented in **Table 4.7.3**. The cell viability values of $Co(OH)_2$ NS (highlighted) are in the range of 1.6-11.4 µg/mL compared to Cobalt acetate used as precursor, that was 5.5-41.6 µg/ml. These results indicated that inside the cells, $Co(OH)_2$ NS could release Co^{2+} ions and exert its toxic activity[62]. However, comparing with cisplatin, in cancer cells $Co(OH)_2$ NS is less potent in the range of 2-32 fold. Conversely, in MRC-5 normal cells the toxicity of $Co(OH)_2$ NS is 80 fold less, which could be a reasonable value to use it as drug. A calculate ratio of potency/toxicity of $Co(OH)_2$ NS vs cisplatin is 2.5-40 fold increased. The results indicated that $Co(OH)_2$ NS could be a possible future potential candidate as an alternative drug effective for late stage tumors therapy. The versatility of the $Co(OH)_2$ NS as potential therapeutic

compound for other cancers, it was tested on HCT-116 colon cancer cell line and demonstrated promising potency and comparable results with FDA approved drug.

	DRUG	AV	SD	RATIO
A2780	Cisplatin	0.05	0.01	1
	$CO(OH)_2$ NS	1.6	0.2	32
	Cobalt Acetate	5.5	2.6	110
OVCAR3	Cisplatin	0.6	0.1	1
	$CO(OH)_2$ NS	11.4	2.2	19
	Cobalt Acetate	12.1	1.7	20
HCT-116	Cisplatin	3.1	0.3	1
	$CO(OH)_2$ NS	6.7	0.4	2
	Cobalt Acetate	41.6	1.6	13
MRC-5	Cisplatin	0.4	0.1	1
	$CO(OH)_2$ NS	31.9	3.6	80
	Cobalt Acetate	29.8	11.4	75

Table 4.7.3. cell viabilities values of $Co(OH)_2$ NS, cobalt acetate and cisplatin. The values are expressed as µg/mL (Copy right Adeel et al.2021).

4.7.4 Apoptosis Analysis

Apoptosis (annexin V) was measured using flow cytometric analysis with $Co(OH)_2$NS (50µg/mL), cobalt acetate (50µg/mL) and cisplatin (6µg/mL) as reference compound at several different time points. All the results are summarized and presented in **Figure 4.7.4**. No apoptosis has been seen in the untreated experiments while cisplatin, cobalt acetate and $Co(OH)_2$ NS promptly induced apoptosis after 6h. Both early and late apoptosis was investigated starting from 6h and increased with time. The apoptosis is very high in $Co(OH)_2$ NS treated cells as compared to cobalt acetate at every time point. These results proved that $Co(OH)_2$NS could be an alternative therapeutic candidate that could cause earlier apoptosis and cell death in aggressive tumors.

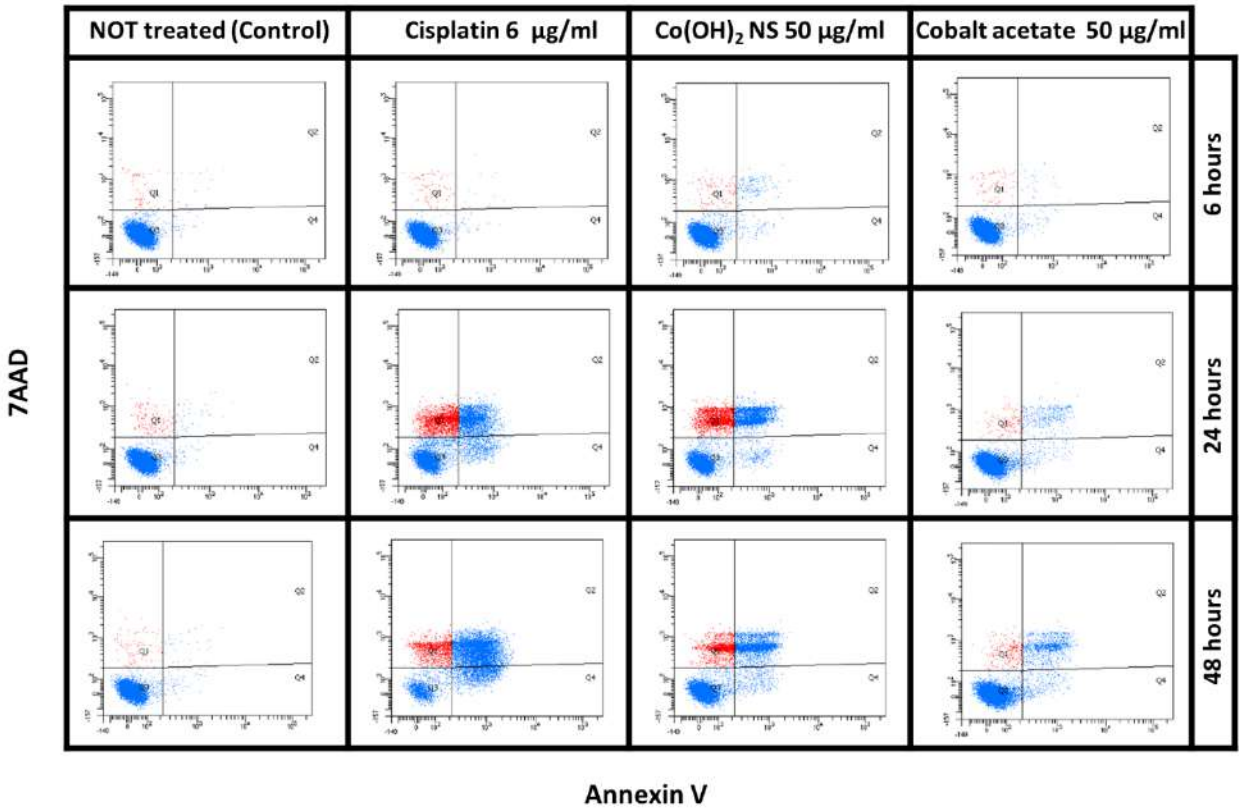

Time (hours)	Sample name	Late Apoptosis % (Q2)		Early Apoptosis % (Q4)	
		Average	SD	Average	SD
6	Not treated	0.05	0.02	0.08	0.04
	Cisplatin	0.05	0.01	0.10	0.02
	Cobalt acetate	0.13	0.02	0.18	0.01
	$Co(OH)_2$ NS	0.46	0.06	0.23	0.02
24	Not treated	0.14	0.04	0.14	0.03
	Cisplatin	8.66	0.05	2.40	0.04
	Cobalt acetate	1.18	0.04	0.58	0.04
	$Co(OH)_2$ NS	8.97	0.33	0.79	0.01
48	Not treated	0.08	0.02	0.17	0.02
	Cisplatin	18.08	1.24	5.29	0.20
	Cobalt acetate	3.36	0.04	0.89	0.04
	$Co(OH)_2$ NS	9.26	1.23	1.13	0.04

Figure 4.7.4. Upper panel: an example of apoptosis analysis of cobalt acetate, $Co(OH)_2$ NS, and cisplatin at different time points. Q1, dead cells; Q2, late apoptosis; Q3, healthy cells; Q4, early apoptosis. Lower panel: values (µg/ml) of early and late apoptosis from three experiments (Copy right Adeel et al.2021).

4.7.5 Lysotracker Observations

Lysosomes have been well recognized to have a key role in the degradation of extracellular materials, included chemotherapeutics agents[63]. The co-localization study were analyzed to compare (evaluate), the amount of $Co(OH)_2$NS trafficking to lysosomes. The experiments were performed in A2780 ovarian cancer cell line (**Figure 4.7.5**). The nucleus of the cell was labeled with Hoechst 33342 (blue), lysosome with Lysotracker™Green DND-26 (green) and $Co(OH)_2$NS was labeled with rhodamine B (red). $Co(OH)_2$NS were analyzed with a fluorescent microscope after different time points (1h, 6h, and 24h). It was noted that $Co(OH)_2$NS were uptaken at each time point. The marked arrows (in yellow) represent the $Co(OH)_2$NS started internalizing even after one hour. The colocalization of $Co(OH)_2$ NS and lysosomes was investigated with Pearson's correlation coefficient (R) after 24h. It was observed an "R" values of 0.43 for $Co(OH)_2$ NS, suggesting that $Co(OH)_2$ NS partially localized to the lysosomes and could relocalize to the cytoplasm avoiding degradation.

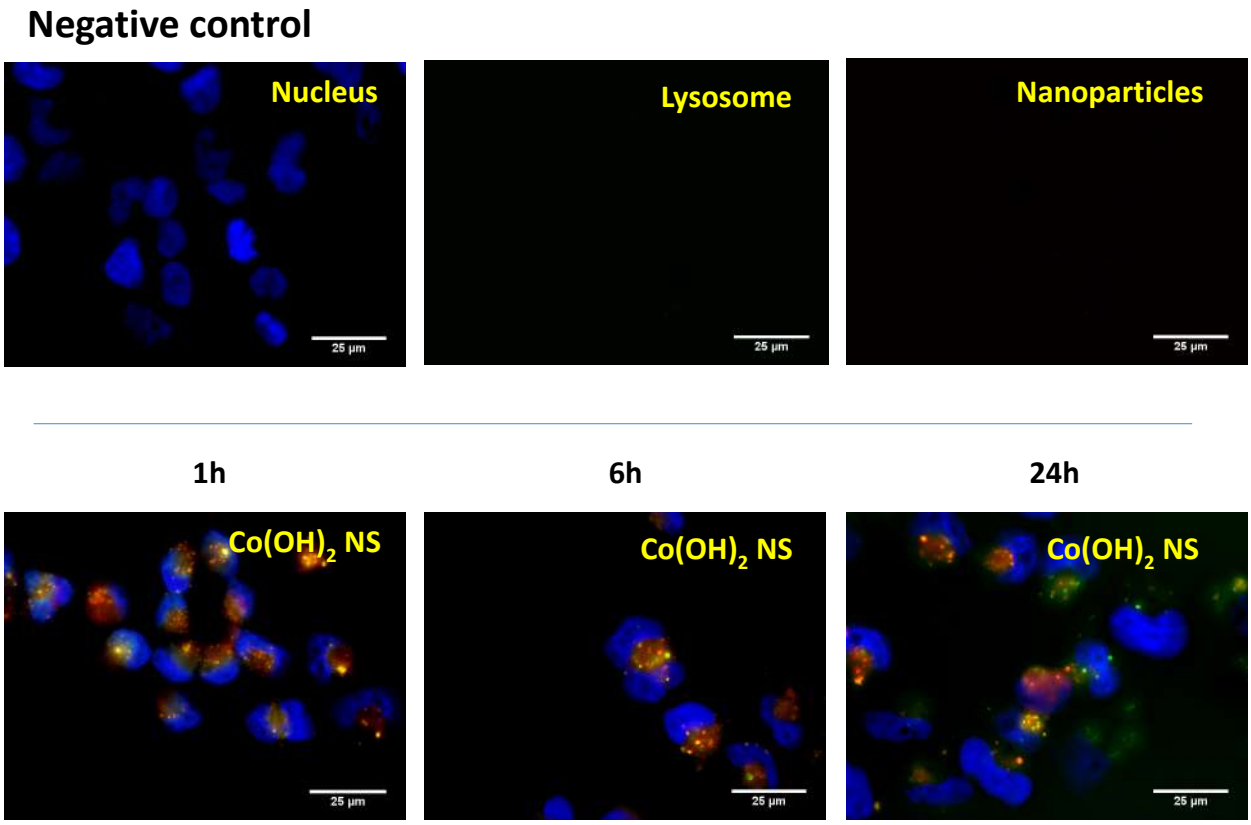

Figure 4.7.5. Lysotracker analysis of $Co(OH)_2$ NS for cell internalization observations. Fluorescence microscopy images of rhodamine-labeled $CO(OH)_2$ NS in A2780 ovarian cancer cells after 1h, 6h and 24h, from the left to the right respectively. Negative control (only nuclei staining, upper part) was used to set-up fluorescence intensity while to avoid background signal. The panel in each row display fluorescence from Hoescht 33342 (nuclei stained blue), LysoTracker green (lysosome stained green), and rhodamine B ($CO(OH)_2$ NS stained red) and merged images. In merged images, the co-localization of rhodamine with LysoTracker green gives yellow areas (Copy right Adeel et al.2021).

4.7.6 Organoids from Cancer Patients Analysis

It is obvious that more than 30% of patients at late stage of ovarian cancer will develop ascites. Ascites are treated indirectly with chemotherapy and paracentesis is used to alleviate the symptoms [64]. Ascites contains free floating cells that are responsible of intraperitoneal metastasis [65].

To test the effectiveness of $Co(OH)_2$ NS, cancer organoids were produced. Cancer organoids are the last frontiers for ex vivo testing of drugs[66–69] that replicate the response of patients in clinic[70]. Two HGSOC derived organoids from ascites (Pat A,B) and one high grade endometroid ovarian cancer from a primary tumor (Pat C) were treated with cobalt acetate and $Co(OH)_2$ NS. $Co(OH)_2$ NS are effective in the range of 7-26 μg/ml (**Table 4.7.6**).

Patients	**Derived from**	**Cobalt acetate**	**$Co(OH)_2$ NS**	**Doxorubicin**
A	**Ascites**	28±4	7±3	1.8±0.4
B	**Ascites**	41±13	26±27	0.09±0.03
C	**Primary tumor**	22±12	16±5	0.9±0.3

Table 4.7.6. IC50 values (μg/ml) of cobalt acetate and $Co(OH)_2$ NS in cancer organoids derived from two HGSOC ascites patients (Pat A,B) and one high grade endometroid tumor patient (Pat C). Data were obtained in triplicates. The numbers represent mean and standard deviation (Copy right Adeel et al.2021).

References

[1] A. X. Zhu, R. B. Lin, X. L. Qi, Y. Liu, Y. Y. Lin, J. P. Zhang, X. M. Chen, *Microporous Mesoporous Mater.* **2012**, *157*, 42.

[2] N. S. Lopa, M. M. Rahman, F. Ahmed, T. Ryu, J. Lei, I. Choi, D. H. Kim, Y. H. Lee, W. Kim, *J. Electroanal. Chem.* **2019**, *840*, 263.

[3] M. Adeel, V. Canzonieri, S. Daniele, A. Vomiero, F. Rizzolio, M. M. Rahman, *Microchim. Acta* **2021**, *188*, 1.

[4] N. S. Lopa, M. M. Rahman, F. Ahmed, S. C. Sutradhar, T. Ryu, W. Kim, *J. Electroanal. Chem.* **2018**, *822*, 43.

[5] M. Nacef, M. L. Chelaghmia, A. M. Affoune, M. Pontié, *Electroanalysis* **2019**, *31*, 113.

[6] C. Y. Ko, J. H. Huang, S. Raina, W. P. Kang, *Analyst* **2013**, *138*, 3201.

[7] D. Su, X. Xie, P. Munroe, S. Dou, G. Wang, *Sci. Rep.* **2014**, *4*, 1.

[8] I. Shackery, U. Patil, A. Pezeshki, N. M. Shinde, S. Kang, S. Im, S. C. Jun, *Electrochim. Acta* **2016**, *191*, 954.

[9] R. Li, Z. Hu, X. Shao, P. Cheng, S. Li, W. Yu, W. Lin, D. Yuan, *Sci. Rep.* **2016**, *6*, 1.

[10] I. Shackery, U. Patil, A. Pezeshki, N. M. Shinde, S. Im, S. C. Jun, *Microchim. Acta* **2016**, *183*, 2473.

[11] S. Ranganatha, N. Munichandraiah, *ACS Omega* **2018**, *3*, 7955.

[12] H. Li, S. Gan, H. Wang, D. Han, L. Niu, *Adv. Mater.* **2015**, *27*, 6906.

[13] M. Baghayeri, A. Sedrpoushan, A. Mohammadi, M. Heidari, *Ionics (Kiel).* **2017**, *23*, 1553.

[14] L. Chen, L. Liu, Q. Guo, Z. Wang, G. Liu, S. Chen, H. Hou, *RSC Adv.* **2017**, *7*, 19345.

[15] M. C. Hsiao, S. H. Liao, M. Y. Yen, P. I. Liu, N. W. Pu, C. A. Wang, C. C. M. Ma, *ACS Appl. Mater. Interfaces* **2010**, *2*, 3092.

[16] J. Pei, T. Zhang, H. Suo, *J. Solid State Electrochem.* **2021**, *25*, 1245.

[17] W. Wan, F. Zhang, S. Yu, R. Zhang, Y. Zhou, *New J. Chem.* **2016**, *40*, 3040.

[18] L. Wang, Y. Park, P. Cui, S. Bak, H. Lee, S. M. Lee, H. Lee, *Chem. Commun.* **2014**, *50*, 1224.

[19] W. Zhang, M. M. Rahman, F. Ahmed, N. S. Lopa, C. Ge, T. Ryu, S. Yoon, L. Jin, H. Jang, W. Kim, *Nanotechnology* **2020**, *31*.

[20] F. Samadaei, M. Salami-Kalajahi, H. Roghani-Mamaqani, M. Banaei, *RSC Adv.* **2015**, *5*, 71835.

[21] W. Li, D. Li, Q. Fu, C. Pan, *RSC Adv.* **2015**, *5*, 80428.

[22] Y. Shao, S. Zhang, C. Wang, Z. Nie, J. Liu, Y. Wang, Y. Lin, *J. Power Sources* **2010**, *195*, 4600.

[23] K. Kordek, L. Jiang, K. Fan, Z. Zhu, L. Xu, M. Al-Mamun, Y. Dou, S. Chen, P. Liu, H. Yin, P. Rutkowski, H. Zhao, *Adv. Energy Mater.* **2019**, *9*.

[24] J. Nimita Jebaranjitham, C. Mageshwari, R. Saravanan, N. Mu, *Compos. Part B Eng.* **2019**, *171*, 302.

[25] Y. Ding, F. Zhang, J. Xu, Y. Miao, Y. Yang, X. Liu, B. Xu, *RSC Adv.* **2017**, *7*, 28754.

[26] S. Ravi, S. Zhang, Y. R. Lee, K. K. Kang, J. M. Kim, J. W. Ahn, W. S. Ahn, *J. Ind. Eng. Chem.* **2018**, *67*, 210.

[27] M. Mahbubur Rahman, J. J. Lee, *Electrochem. commun.* **2021**, *125*.

[28] M. Rohani Moghadam, L. Salehi, S. Jafari, N. Nasirizadeh, J. Ghasemi, *Microchim. Acta* **2019**, *186*.

[29] S. R. Chinnadayyala, S. Cho, *Sensors* **2021**, *21*, 1.

[30] H. R. Barai, N. S. Lopa, F. Ahmed, N. A. Khan, S. A. Ansari, S. W. Joo, M. M. Rahman, *ACS Omega* **2020**, *5*, 22356.

[31] M. Adeel, V. Canzonieri, S. Daniele, A. Vomiero, F. Rizzolio, M. M. Rahman, *Microchim. Acta* **2021**, *188*.

[32] Y. SAITO, *Rev. Polarogr.* **1968**, *15*, 177.

[33] R. C. Engstrom, C. M. Pharr, *Anal. Chem.* **1989**, *61*, 1099 A.

[34] Z. Rahmati, M. Roushani, H. Hosseini, H. Choobin, *Microchim. Acta* **2021**, *188*.

[35] B. Mojsoska, S. Larsen, D. A. Olsen, J. S. Madsen, I. Brandslund, F. A. Alatraktchi, *Sensors* **2021**, *21*, 1.

[36] M. Adeel, F. Duzagac, V. Canzonieri, F. Rizzolio, *ACS Appl. Nano Mater.* **2020**, *3*, 4962.

[37] W. Zhang, M. M. Rahman, F. Ahmed, N. S. Lopa, C. Ge, T. Ryu, S. Yoon, L. Jin, H. Jang, W. Kim, *Nanotechnology* **2020**, *31*.

[38] M. Adeel, M. M. Rahman, J. J. Lee, *Biosens. Bioelectron.* **2019**, *126*, 143.

[39] W. Zhang, M. M. Rahman, F. Ahmed, N. S. Lopa, C. Ge, T. Ryu, S. Yoon, L. Jin, H. Jang, W. Kim, *Nanotechnology* **2020**, *31*, 13.

[40] M. Kaszuba, J. Corbett, F. M. N. Watson, A. Jones, Royal Society, 2010; Vol. 368, pp. 4439–4451.

[41] G. M. Zayed, I. Kamal, W. A. Abdelhafez, F. M. Alsharif, M. A. Amin, M. S. A. Shaykoon, H. A. Sarhan, A. M. Abdelsalam, *Pharm. Res.* **2018**, *35*, 1.

[42] P. Yousefpour, F. Atyabi, E. Vasheghani-Farahani, A. A. M. Movahedi, R. Dinarvand, *Int. J. Nanomedicine* **2011**, *6*, 1977.

[43] M. A. Nejad, P. Umstätter, H. M. Urbassek, *J. Mol. Model.* **2020**, *26*, 1.

[44] M. A. Nejad, P. Umstätter, H. M. Urbassek, *J. Mol. Model.* **2020**, *26*.

[45] D. T. Manallack, R. J. Prankerd, E. Yuriev, T. I. Oprea, D. K. Chalmers, *Chem. Soc. Rev.* **2013**, *42*, 485.

[46] K. Baba, H. E. Pudavar, I. Roy, T. Y. Ohulchanskyy, Y. Chen, R. K. Pandey, P. N. Prasad,

Mol. Pharm. **2007**, *4*, 289.

[47] F. Liu, J. Y. Park, Y. Zhang, C. Conwell, Y. Liu, S. R. Bathula, L. Huang, *J. Pharm. Sci.* **2010**, *99*, 3542.

[48] J. Park, B. Sun, Y. Yeo, *J. Control. Release* **2017**, *263*, 90.

[49] O. R. Rodig, *J. Med. Chem.* **1963**, *6*, 826.

[50] O. R. Rodig, *J. Med. Chem.* **1963**, *6*, 826.

[51] P. M. Costanzo, *Clays Clay Miner.* **2001**, *49*, 372.

[52] S. M. Dizaj, Z. Vazifehasl, S. Salatin, K. Adibkia, Y. Javadzadeh, *Res. Pharm. Sci.* **2015**, *10*, 95.

[53] J. B. Wolinsky, Y. L. Colson, M. W. Grinstaff,. *J. Control. Release* **2012**, *159*, 14–26.

[54] A. Gil-Ordóñez, M. Martín-Fontecha, S. Ortega-Gutiérrez, M. L. López-Rodríguez,. *Biochem. Pharmacol.* **2018**, *157*, 18–32.

[55] M. Elluru, H. Ma, M. Hadjiargyrou, B. S. Hsiao, B. Chu, *Polymer (Guildf).* **2013**, *54*, 2088.

[56] C. Granchi, M. Lapillo, S. Glasmacher, G. Bononi, C. Licari, G. Poli, M. El Boustani, I. Caligiuri, F. Rizzolio, J. Gertsch, M. Macchia, F. Minutolo, T. Tuccinardi, A. Chicca, *J. Med. Chem.* **2019**, *62*, 1932.

[57] Q. Peng, S. Zhang, Q. Yang, T. Zhang, X. Q. Wei, L. Jiang, C. L. Zhang, Q. M. Chen, Z. R. Zhang, Y. F. Lin, *Biomaterials* **2013**, *34*, 8521.

[58] R. D. Minshall, A. B. Malik, *Handb. Exp. Pharmacol.* **2006**, *176*, 107.

[59] M. Lapillo, B. Salis, S. Palazzolo, G. Poli, C. Granchi, F. Minutolo, R. Rotondo, I. Caligiuri, V. Canzonieri, T. Tuccinardi, F. Rizzolio, *ACS Med. Chem. Lett.* **2019**, *10*, 475.

[60] C. Guo, X. Hou, L. Dong, J. Marakovits, S. Greasley, E. Dagostino, R. Ferre, M. Catherine Johnson, P. S. Humphries, H. Li, G. D. Paderes, J. Piraino, E. Kraynov, B. W. Murray, *Bioorganic Med. Chem. Lett.* **2014**, *24*, 4187.

[61] M. Kim, D. H. Nam, H. Y. Park, C. Kwon, K. Eom, S. Yoo, J. Jang, H. J. Kim, E. Cho, H. Kwon, *J. Mater. Chem. A* **2015**, *3*, 14284.

[62] D. J. Paustenbach, B. E. Tvermoes, K. M. Unice, B. L. Finley, B. D. Kerger, A review of the health hazards posed by cobalt. *Crit. Rev. Toxicol.* **2013**, *43*, 316–362.

[63] J. Hraběta, M. Belhajová, H. Šubrtová, M. A. M. Rodrigo, Z. Heger, T. Eckschlager,. *Int. J. Mol. Sci.* **2020**, *21*, 1–18.

[64] E. Kipps, D. S. P. Tan, S. B. Kaye,. *Nat. Rev. Cancer* **2013**, *13*, 273–282.

[65] E. Smolle, V. Taucher, J. Haybaeck,. *Anticancer Res.* **2014**, *34*, 1553–1562.

[66] S. Palazzolo, M. Hadla, C. R. Spena, I. Caligiuri, R. Rotondo, M. Adeel, V. Kumar, G. Corona, V. Canzonieri, G. Toffoli, F. Rizzolio,. *Cancers (Basel).* **2019**, *11*.

[67] C. Granchi, G. Bononi, R. Ferrisi, E. Gori, G. Mantini, S. Glasmacher, G. Poli, S. Palazzolo, I. Caligiuri, F. Rizzolio, V. Canzonieri, T. Perin, J. Gertsch, A. Sodi, E. Giovannetti, M. Macchia, F. Minutolo, T. Tuccinardi, A. Chicca,. *Eur. J. Med. Chem.* **2021**, *209*, 112857.

[68] T. Scattolin, E. Bortolamiol, F. Visentin, S. Palazzolo, I. Caligiuri, T. Perin, V. Canzonieri, N. Demitri, F. Rizzolio, A. Togni, *Chem. - A Eur. J.* **2020**, *26*, 11868–11876.

[69] F. Duzagac, G. Saorin, L. Memeo, V. Canzonieri, F. Rizzolio, Microfluidic organoids-on-a-chip: Quantum leap in cancer research. *Cancers.* **2021**, *13*, 1–35.

[70] S. J. Hill, B. Decker, E. A. Roberts, N. S. Horowitz, M. G. Muto, M. J. Worley, C. M. Feltmate, M. R. Nucci, E. M. Swisher, H. Nguyen, C. Yang, R. Morizane, B. S. Kochupurakkal, K. T. Do, P. A. Konstantinopoulos, J. F. Liu, J. V. Bonventre, U. A. Matulonis, G. I. Shapiro, R. S. Berkowitz, C. P. Crum, A. D. D'Andrea, *Cancer Discov.* **2018**, *8*, 1404–1421.

Chapter 05: Conclusions and Perspectives

The results reported in this thesis have highlighted the usefulness of nanotechnologies and nanomaterials for the development of either sensor systems or new methodologies to treat or cure illnesses. These possibilities have emerged from convergence of the physical sciences, chemistry and biology. The trends which dominate the research in these fields include several aspects and among others include: i) efforts to develop effective point of care tests and implantable/wearable technologies for early diagnosis and continuous monitoring of small molecules or detecting the biomarkers status; ii) the inclusion of active pharmaceutical ingredients in drug delivery systems, which represent a contemporary approach to overcome problems such as poor solubility and stability of the drug in physiological media or their permeation within the cells or to locally treat cancer cells. Based on these considerations, the work done in the three years PhD activity can be divided in two main topics.

The first is concerned with the use of nanomaterials to develop electrochemical-based sensors for monitoring glucose, working, possibly, at physiological conditions, and for early-stage diagnosis of SARS-CoV-2 infection. The second topic is related to the development of nanomaterials as drug carriers or for direct cure of cancer cells.

The main achievements and future perspectives of the work are summarized below for each main topic.

Topic I- Glucose sensors

Two types of glucose sensors have been developed, belonging to the so called fourth-generation glucose sensors. They are essentially enzyme-free sensors and, by the use of nanomaterials, also defined nanozymes. The first sensor is based on a 2D metal azolate framework (i.e., MAF-5) and $Co(OH)_2$ nanosheets (2D MAF-5-CoII NS). It was was synthesized by a simple hydrothermal method and the material displayed high purity and crystallinity, as well as high surface area, as

assessed by surface and spectroscopic techniques. The procedure adopted for the synthesis allowed obtaining a nanostructured material containing a large number of active sites, easily accessible, for the catalytic oxidation of glucose to gluconolactone. The latter reaction occurred through the Co(III/Co(II) redox pair present in the MAF-5 structure, in turn regenerated by applying a constant potential (i.e., + 0.45 V vs. Ag/AgCl reference electrode). The measurements have been performed using a simple and commercially available screen-printed electrode (SPE), housed in a home-made holder, able to process many samples in relatively short times. The detection of glucose has been carried out by amperometry. The 2D MAF-5-CoII NS redox system proved better catalytic activity toward the oxidation of glucose in alkaline medium with respect to a BP buffer. In any case, the developed sensor displayed high electrochemical stability and reproducibility (up to 1 or 100 CV cycles) the with negligible interferences from some common interfering compounds, such as fructose, galactose, and lactose. The sensor was also tested in PBs diluted plasma samples. It must be considered that, although the analytical performance of the MAF-5-CoII NS/SPE sensor in PBS diluted BP solution is lower compared to that in the NaOH diluted BP solution, it is promising for the construction of disposable type sensor for direct measurements in blood. Additionally, MAF-5-CoII NS material has potential as catalytic electrode material to detect other biologically important compounds, due to its good stability in aqueous medium.

Exploiting a simple solution process, mediated by organic bases, $Co(OH)_2$ nanosheets (2D-NS of $Co(OH)_2$), enriched with oxygen vacancies were synthesized and used as nanozyme to promote the direct oxidation of glucose. Also, in this case, the material was characterized by surface and spectroscopic techniques. This compound displayed, as the 2D MAF-5-CoII NS, good catalytic activity towards glucose oxidation, in both NaOH and PBS at physiological pH, in the latter case with higher sensitivity with respect to the alkaline medium. The general better analytical

performance of the $Co(OH)_2$ NS/SPE sensor at physiological pH, could be due to the high surface area and oxygen vacancies, and this makes it very promising for the construction of simple apparatuses for glucose detection directly in human body fluids. The sensor showed good selectivity for glucose with respect to fructose, galactose, and lactose, other than good reproducibility, and long-term stability.

Topic I- Covid-19 sensor

A self-supported EDA functionalized GCF electrode was developed for the label-free detection of SARS-CoV-2 SP. This was constructed by the controlled and partial oxidation and exfoliation of the GCF surface (down to a few layers) with the consequent EDA functionalization. The EDA-GCF electrode served as the anti-SARS-CoV-2 immobilization matrix, which enabled the subsequent SARS-CoV-2 SP binding at the sensor probe, and consequently its quantification. The immunosensor thus prepared could detect SARS-CoV-2 SP in PBS and diluted blood plasma samples over a wide concentration range (0.2–100 ng/mL), with the LOD of 25 and 27 pg/mL, respectively, without any significant interference from other proteins, such as SARS-CoV, BSA, HSA.

The self-supported electrode proposed here could be advantageous for developing sensors with high sensitivity, stability, and low cost since it could minimize the necessity of post-fabrication of electrodes with the pre-developed nanomaterials. Furthermore, because GCF, OGCF, and EDA-GCF are flexible, and therefore easily wearable, are promising for the integration of the corresponding developed sensing devices in face masks, for remote monitoring of SARS-CoV-2 and other biomolecules. This proposed sensor and the study reported could open a new avenue for

developing flexible and self-supported electrodes for various electroanalytical applications using other low-cost carbon-based electrodes (e.g., carbon cloth, carbon fiber sheet, etc.).

Topic II- Drug Delivery Carriers of Doxorubicin for Cancer Therapeutic Applications

In this topic, 2D hydroxylated boron nitride nanosheets has been synthesized by simple hydrothermal method. The as prepared OH-BN was characterized by different spectroscopic techniques to analyze the surface properties and to confirm the structural purity. The biocompatibility of the material (OH-BN) was tested on different normal cell lines. The results have showed the biocompatible nature of the materials and, therefore, their suitability as carriers in therapeutic applications. The hydroxylated 2D boron nitride nanosheets were loaded with doxorubicin providing a rather high loading efficiency (i.e., 82%) and suitable release of the drug at tumoral sites. The stability of the material (OH-BN) was tested for up to 60 days at two different pH (7.4 and 5.5). The results showed excellent stability compared to the bulk BN material. Finally, the OH-BN loaded with doxorubicin was tested on different ovarian cancer cell lines. The results demonstrated excellent therapeutic efficacy, as that observed for the free drug towards different ovarian cancer cell lines.

Topic II- Solubility and Carrier Free Delivery System of Super Hydrophobic Monoacylglycerol Lipase Inhibitor for Cancer Therapy

The first nanoformulation of a potent MAGL inhibitor, MAGL23, which is a promising compound as anticancer agent, was developed. MAGL is an enzyme that is highly expressed in tumors, where it plays a fundamental role in the oncogenic lipid signaling that promotes invasion, migration, survival, and in vivo tumor growth. Many MAGL inhibitors have been reported in the literature

and they showed positive effects when tested in in vivo studies. However, most MAGL inhibitors act by an irreversible mechanism of action, which provokes many negative effects in animal models, thus hampering their further development as drugs. On the other hand, potent MAGL reversible inhibitors are usually characterized by a high lipophilicity. MAGL23 is a recently published reversible MAGL inhibitor, whose development is facilitated by its high selectivity towards other members of the endocannabinoid system as well as by its straightforward synthetic preparation. Unfortunately, not a single delivery system is available (for reversible and irreversible inhibitors). A challenge in drug delivery systems is to have one single system able to protect and transport the drug to the target site without compromising the potency. Most of the systems are not stable in *in vivo,* suffer of a low loading efficiency and require drug pre-solubilization (because of their intrinsically hydrophobic nature). Hence, a nanocrystallization method was employed to decrease the size of the crystals of MAGL23. They were dissolved in an organic solvent together with different surfactants, which helps to decrease the size of nanocrystals and provides their hydrophilicity, in turn increasing the solubility at about 1 mg/ml. Usually, the pharmacokinetics profile of the therapeutic compounds is altered by decreasing the size (while employing different physical or chemical methods to achieve the solubility) in turn influencing the potency of the compound. But in our case, the nanocrystal formation was thoroughly observed by different spectroscopic techniques and results demonstrated that there was no change in the structural properties and the IC_{50} data on cells are also in line with the results obtained with the compound stand-alone. The nanocrystals were formulated with albumin for safe delivery applications. Indeed, albumin can direct the therapeutic compound at tumoral sites via the GP60 receptor and SPARC, and also it stabilizes the nanocrystals avoiding unwanted protein adsorption during circulation in the body. Furthermore, our future research is directed to investigate the *in vivo* properties of the

formulated nanocrystals in animal models. In conclusion, in this article, we developed the first soluble and easily absorbable nanoformulation system for a potent reversible MAGL inhibitor for a future use in clinical applications.

Topic II- Self-Therapeutic Cobalt Hydroxide Nanosheets ($Co(OH)_2$ NS) for Ovarian Cancer Therapy

$Co(OH)_2$ NS synthesized by a simple solution process has been used as a self-therapeutic drug for treating HGSOC. The results revealed that the cytotoxicity of the cobalt acetate (the precursor) and the as-synthesized high purity and crystalline $Co(OH)_2$ NS showed toxic activity in the same range for cancer cells. Compared to cisplatin, $Co(OH)_2$ NS is less toxic with a favorable potency/toxicity ratio. Flow cytometric analysis (Annexin V) showed an increase in cellular apoptosis that was much more evident for $Co(OH)_2$ NS than cobalt acetate. Furthermore, colocalization and cellular internalization experiments of $Co(OH)_2$NS using lysotracker marker indicated an active internalization of $Co(OH)_2$ NS that can escape the lysosomal degradation pathway. Although a high concentration of cobalt is toxic for humans, however, nanoformulations have been demonstrated to be potentially safe at least at the preclinical level. Thus, this study opens up a window to develop cobalt-based nanomaterials as self-therapeutic nanomedicine for cancer therapy.

The future prospective of this thesis includes (part-I) the development of wearable or implantable systems (using microelectrodes) to detect biomolecules of interest from complex biological solutions for continuous real time measurements or in live cells. These microelectrodes could be modified through different nano materials (organic, inorganic and polymers) that have high surface to volume ratio and good electrocatalytic activities, to provide sensitive and selective sensor signal for the biomolecule of interest from overall complex biological fluids. Wearable sensor system

could be promoted by the development of several electrocatalytic 2D materials synthetized through different physical or chemical methods to achieve defects free surface on flexible substrates (carbon cloths, PDMS, PET etc.) for the stable covalent immobilization of bio molecule e.g., antibody, aptamers etc. to detect the biological targets employing with the different parts of the body.

The second part of the thesis (Part-II) could be promoted by using different self-therapeutic nanomaterials like bi-metallic nitroprusside that can have abilities to kill cancer cells through Fenton mediated chemistry, through their different dual self-therapeutic options, like having bi-metallic cations as perfect chemodynamic agent and naturally present NO species to generate ROS specifically on cancer cells.

List of Publications:

1. **M. Adeel,** K. Asif, V. Canzonieri, S. Daniele, M. M. Rahman, F. Rizzolio, Controlled, Partially Exfoliated, Self-Supported Functionalized Flexible Graphitic Carbon Foil for Ultrasensitive Detection of SARS-CoV-2 Spike Protein. (Submitted in Adv.Sci.)
2. **M. Adeel,** G. Saorin, G. Boccalon, A. A. Sfriso, S. Parisi, I. Moro, S. Palazzolo, I. Caligiuri, C. Granchi, V.Canzonieri, T. Tuccinardi, F. Rizzolio. Carrier Free Delivery System of Monoacylglycerol Lipase Hydrophobic Inhibitor for Cancer Therapy. (Submitted in Int J of Pharmaceutics).
3. **M. Adeel,** P. Salvatore, M. Matteo, K. Asif, B. Michele, P. Fabio, C. Isabella, M. M. Rahman, C. Vincenzo, F. Rizzolio. Self-Therapeutic Cobalt Hydroxide Nanosheets (Co(OH)2 NS) for Ovarian Cancer Therapy (Just accepted in ACS Omega).
4. **M. Adeel,** K. Asif, V. Canzonieri, S. Daniele, M. M. Rahman, F. Rizzolio, Glucose Detection Devices and Methods Based on Metal–Organic Frameworks and Related Materials. *Adv. Funct. Mater.* **2021.** https://doi.org/10.1002/adfm.202106023
5. **M. Adeel,** V. Canzonieri, S. Daniele, A. Vomiero, F. Rizzolio, M. M. Rahman. 2D Metal Azolate Framework as a Highly Sensitive Nanozyme for Glucose Detection in Human Blood Plasma at Physiological pH and Alkaline Medium. *Microchim. Acta.* **2021**, *188,* 77 : Doi.org/10.1007/s00604-021-04737-w.
6. **M. Adeel,** V. Canzonieri, S. Daniele, F. Rizzolio, M. M. Rahman. Organobase Assisted Synthesis of Co(OH)2 Nanosheets Enriched with Oxygen Vacancies for Nonenzymatic Glucose Sensing at Physiological pH. J. Ind. Eng. Chem. **2021**, *7*, 30. Doi.org/10.1016/j.jiec.2021.07.030.
7. **M. Adeel,** M. M. Rahman, I. Caligiuri, V. Canzonieri, F. Rizzolio, S. Daniele. Recent advances of electrochemical and optical enzyme-free glucose sensors operating at physiological conditions, **2020**, *165*. 112331. Doi.org/10.1016/j.bios.2020.

8. **M. Adeel,** F. Duzagac, V. Canzonieri, F. Rizzolio. Self-Therapeutic Nanomaterials for Cancer Therapy: A Review. *ACS Appl. Nano Mater.* **2020**, *3,* 4962. Doi.org/10.1021/acsanm.0c00762.

9. S. Bayda, **M. Adeel,** T. Tuccinardi, M. Cordani, F. Rizzolio. The History of Nanoscience and Nanotechnology: From Chemical–Physical Applications to Nanomedicine. **2020**, *25*, 1. Doi:10.3390/molecules25010112.

10. S. Palazzolo, M. Hadla, C. R. Spena, S. Bayda, V. Kumar, F. Lo Re, M. Adeel, I. Caligiuri, F. Romano, G. Corona, V. Canzonieri, G. Toffoli, F. Rizzolio, Proof-of-Concept Multistage Biomimetic Liposomal DNA Origami Nano system for the Remote Loading of Doxorubicin. ACS Med. Chem. Lett. 2019, *10*, 517. Doi: 10.1021/acsmedchemlett.8b00557.

11. S. Palazzolo, M. Hadla, C. R. Spena, I. Caligiuri, R. Rotondo, **M. Adeel,** V. Kumar, G. Corona, V. Canzonieri, G. Toffoli, F. Rizzolio. An effective multi-stage liposomal DNA origami nano system for in vivo cancer therapy. Cancer. **2019**, *11*,12. Doi:10.3390/cancers11121997.